Creation and Study of Matter in Extreme Conditions by High-intensity Free-electron Laser Radiation

Sam M. Vinko

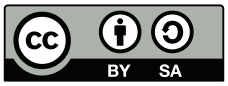
BY SA

to my grandmother, mother, sister, Ivo and Jože

Creation and Study of Matter in Extreme Conditions by High-intensity Free-electron Laser Radiation

Sam M. Vinko
Wolfson College, University of Oxford

Thesis submitted for the degree of Doctor of Philosophy
Michaelmas term, 2010

Abstract

The recent development of free-electron lasers operating at XUV and X-ray wavelengths are proving vital for the exploration of matter in extreme conditions. The ultra-short pulse length and high peak brightness these light sources provide, combined with a tunable X-ray wavelength range, makes them ideally suited both for creating high energy density samples and for their subsequent study. In this thesis I describe the work done on the XUV free-electron laser FLASH in Hamburg, aimed at creating homogeneous samples of warm dense matter through the process of volumetric XUV photo-absorption, and the theoretical work undertaken to understand the process of high-intensity laser-matter interactions. As a first step, we have successfully demonstrated intensities above 10^{17} Wcm^{-2} at a wavelength of 13.5 nm, by focusing the FEL beam to micron and sub-micron spot sizes by means of a multilayer-coated off-axis parabolic mirror. Using these record high intensities, we have demonstrated for the first time saturable absorption in the XUV. The effect was observed in aluminium and magnesium samples and is due to the bleaching of a core-state absorption channel by the intense radiation field. This result has major implications for the creation of homogeneous high energy density systems, as a saturable absorption channel allows for a more homogeneous heating mechanism than previously thought possible. Further, we have conducted soft X-ray emission spectroscopy measurements which have delivered a wealth of information on the highly photo-excited system under irradiation, immediately after the excitation pulse, yet before the system evolves into the warm dense matter state. Such strongly photo-excited samples have also been studied theoretically, by means of density functional theory coupled to molecular dynamics calculations, yielding detailed electronic structure information. The use of the emission spectroscopy as a probe for solid-density and finite-temperature systems is discussed in light of these results. Theoretical efforts have further been made in the study of the free-free absorption of aluminium as the system evolves from the solid state to warm dense matter. We predict an absorption peak in temperature as the system heats and forms a dense plasma. The physical significance of this effect is discussed in terms of intense light-matter interactions on both femtosecond and picosecond time-scales.

Contents

Acronyms

CPU	Central Processing Unit
DFT	Density Functional Theory
DOS	Density Of States
pDOS, LDOS	projected, Local Density Of States
EOS	Equation Of State
FCC	Face Centred Cubic
FEL	Free-Electron Laser
FWHM	Full Width at Half Maximum
GGA	Generalized Gradient Approximation
GMD	Gas Monitor Detector
HHG	High Harmonic Generation
HNC	Hyper-Netted Chain Equations
KG	Kubo-Greenwood equation
LDA	Local Density Approximation
LFC	Local Field Correction
MEC	Matter in Extreme Conditions
MD	classical Molecular Dynamics
NFE	Near-Free Electron approximation
OAP	Off-Axis Parabola
OCP	One-Component Plasma
PAW	Projector Augmented Wave
PMMA	Poly(Methyl MethAcrylate)
RMS	Root Mean Square
RPA	Random Phase Approximation
SASE	Self-Amplified Spontaneous Emission
UV, VUV, XUV	UltraViolet, Vacuum UV, x-ray UV
VASP	Vienna Ab-initio Simulation Package
WDM	Warm Dense Matter
XES	X-ray Emission Spectroscopy

Facilities, Institutions

CEA	Commissariat à l'Énergie Atomique
DESY	Deutsches Elektronen-Synchrotron
ESRF	European Synchrotron Radiation Facility
FAIR	Facility for Antiproton and Ion Research
FLASH	Free-electron LASer in Hamburg
GSI	Gesellschaft für SchwerIonenforschung
LCLS	Linac Coherent Light Source
PBC	Peak Brightness Collaboration
SCSS	SPring-8 Compact SASE Source
SLAC	Stanford Linear Accelerator Center
XFEL	European X-ray Free-electron Laser

Notation

quantity	symbol(s)	value / preferred units
absorption	A	-
absorption coefficient	$\kappa(\omega)$	m^{-1}
Boltzmann's constant	k_B	1.381×10^{-23} m^2 kg s^{-2} K^{-1}
charge number	Z	-
chemical potential	μ	eV
collision frequency	ν	s^{-1}
conductivity	$\sigma(k,\omega)$	$\mathrm{m}^{-1}\ \Omega^{-1}$
coordinate	r, x, y, z	m
Coulomb logarithm	$\ln\Lambda = \ln(\lambda_\mathrm{D}/r_0)$	-
Coulomb potential	$\nu(q)$	eV
cross section	σ	1 b (10^{-28} m^2)
current density	j	A m^{-2}
Debye length	$\lambda_\mathrm{D} = \omega_p\sqrt{k_\mathrm{B}T/m_e}$	m
Debye wavevector	$K_\mathrm{D} = \sqrt{Zn_e e^2/(\epsilon_0 k_\mathrm{B}T)}$	m^{-1}
density	n	m^{-3}
density of states	$\rho(E)$	states/(eV atom)
dielectric function	$\epsilon(k,\omega), \varepsilon(k,\omega)$	-
electron charge	e	1.602×10^{-19} C
electron mass	m_e	9.109×10^{-31} kg
electron stopping power	$S(E) = dE/dx$	J m^{-1}
energy	E	eV or J
Fermi-Dirac distribution	$f_\mathrm{FD}, f(k)$	-
Fermi energy	E_F	eV
Fermi temperature	$k_\mathrm{B}T_\mathrm{F}$	eV
fluence	F	Jcm^{-2}
gamma function	$\Gamma(z) = \int_0^\infty t^{z-1}\mathrm{e}^{-\mathrm{t}}\mathrm{dt}$	-
Hamiltonian	$\mathcal{H}$	-
imaginary unit	i	-
indices	k, l, m, n	-
inverse thermal energy	$\beta = (k_\mathrm{B}T)^{-1}$	eV^{-1}
ion-ion structure factor	$S(q)$	-

Notation

quantity	symbol(s)	value / preferred units
kinetic energy	T	eV or J
Landau length	$r_0 = Ze^2/k_\mathrm{B}T$	m
Maxwell-Boltzmann distr.	f_MB	-
momentum	p	m kg s^{-1}
number	N	-
photon angular velocity	ω	rad s^{-1}
Planck's constant	$h(\hbar = h/2\pi)$	6.626×10^{-34} m^2 kg s^{-1}
plasma frequency (energy)	$\hbar\omega_p$	eV
plasma parameter	Γ	V/T
potential energy	V, U	eV or J
radiation intensity	I	W cm^{-2}
rate	R	s^{-1}
reciprocal lattice vector	$\mathbf{G}, G = \lvert\mathbf{G}\rvert$	m^{-1}
reciprocal space coordinate	k, q	m^{-1}
speed of light	c	2.9979×10^8 m s^{-1}
temperature	T	K
thermal energy	$k_\mathrm{B}T$	eV
time	t, τ	s
transmission	T	-
vacuum permittivity	ϵ_0	8.854×10^{-12} F m^{-1}
volume	V	m^3
wavefunction	Ψ, ψ, ϕ	$\mathrm{m}^{-3/2}$

CHAPTER 1

Introduction

The study of high energy density matter is an expanding area of intense current research and is of great importance for both fundamental and applied physics. A high energy density system is defined roughly as having an energy density above 10^{11} Jm^{-3}. Such matter is widespread in the universe in a variety of forms, ranging from the interiors of giant planets such as Saturn and Jupiter, to the constituent matter of all the different types of stars. Importantly, the coupling of such matter with electromagnetic radiation is the basic interaction that underlines astrophysical observations, and is the prime source of information available to us about our surrounding physical universe. Our understanding of these systems in extreme conditions and their radiative and transport properties is in this sense one of the backbones of modern science.

Systems containing high energy densities are extremely short-lived if unconfined. In the realm of astrophysics, such confinement is provided by the gravitational force, as these systems are often large and massive. The possibility to generate analogous samples in the controlled environment of a laboratory, where it could then be tampered with, tailored and probed, is an extremely attractive one, with research to this end constituting the exciting field of laboratory astrophysics. As use of gravitational confinement in a laboratory setting is not viable, these systems can be confined in two ways: either by an external magnetic field, or through the inertia of the constituent particles of the system. The latter has become of particular interest recently as it allows for much denser systems to be created and is the scheme of choice for laser-driven inertially confined nuclear fusion

experiments [1, 2].

This thesis is focused on a particular kind of high energy density system, with densities characteristic to ground-state metallic samples and temperatures between 1 and 10 eV: Warm Dense Matter (WDM). This state has a very transient nature and significant effort has been invested in learning how to create representative samples at homogeneous conditions in a controlled manner using the mechanism of volumetric photoabsorption. Although this mechanism is by no means unique, I aim to demonstrate that it is indeed very efficient at sub-picosecond homogeneous heating. The work comprising this thesis is therefore interested in the many facets pertaining to high-intensity light-matter interactions. Investigations have been carried out on this topic both from the theoretical and computational point of view, but also experimentally, which has been made possible only very recently by the advent of the latest 4^{th} generation free-electron laser (FEL) light sources.

It is in this context that the absorption mechanism is of vital importance to understand the process of creation of high energy density matter. For example, the absorption coefficient defines the total amount of energy that can be deposited in a given sample, as well as the penetration depth, important for homogeneous energy deposition. Furthermore, the cross sections of different absorption channels define the dominant microscopic mechanism in a particular wavelength regime. These mechanisms can be very different and have a strong impact on the interaction process. Importantly, all these aspects are tied together to yield the main experimental observables of interest: the highest final temperature achieved and the temperature and density profile within the sample. These are some of the main points that this thesis hopes to tackle in addressing the efficient creation of WDM and it follows that a significant portion will be dedicated to studying the detailed absorption process, in particular involving metallic aluminium. Aluminium was chosen because it is a prototypical metallic system, which has been extensively investigated both theoretically and experimentally, and most of its properties are known. Furthermore, it is widely available, inexpensive, and simple to handle.

The interaction of light with a material is governed by its electronic structure. In an isolated atom the electronic states are discrete and the dominant parameters to describe this interaction are the occupancy of the levels and their energy compared with the continuum. All the states are bound and are, at least in this regard, very similar. In a solid the situation changes: the electrons in the highest lying levels are delocalized and an energy band forms. As it originates from the bonding valence electrons, it is called the *valence band*[1]. Aluminium has the very useful property of having a valence

[1]The term *conduction band* is also often used as this band is responsible for the conduction properties

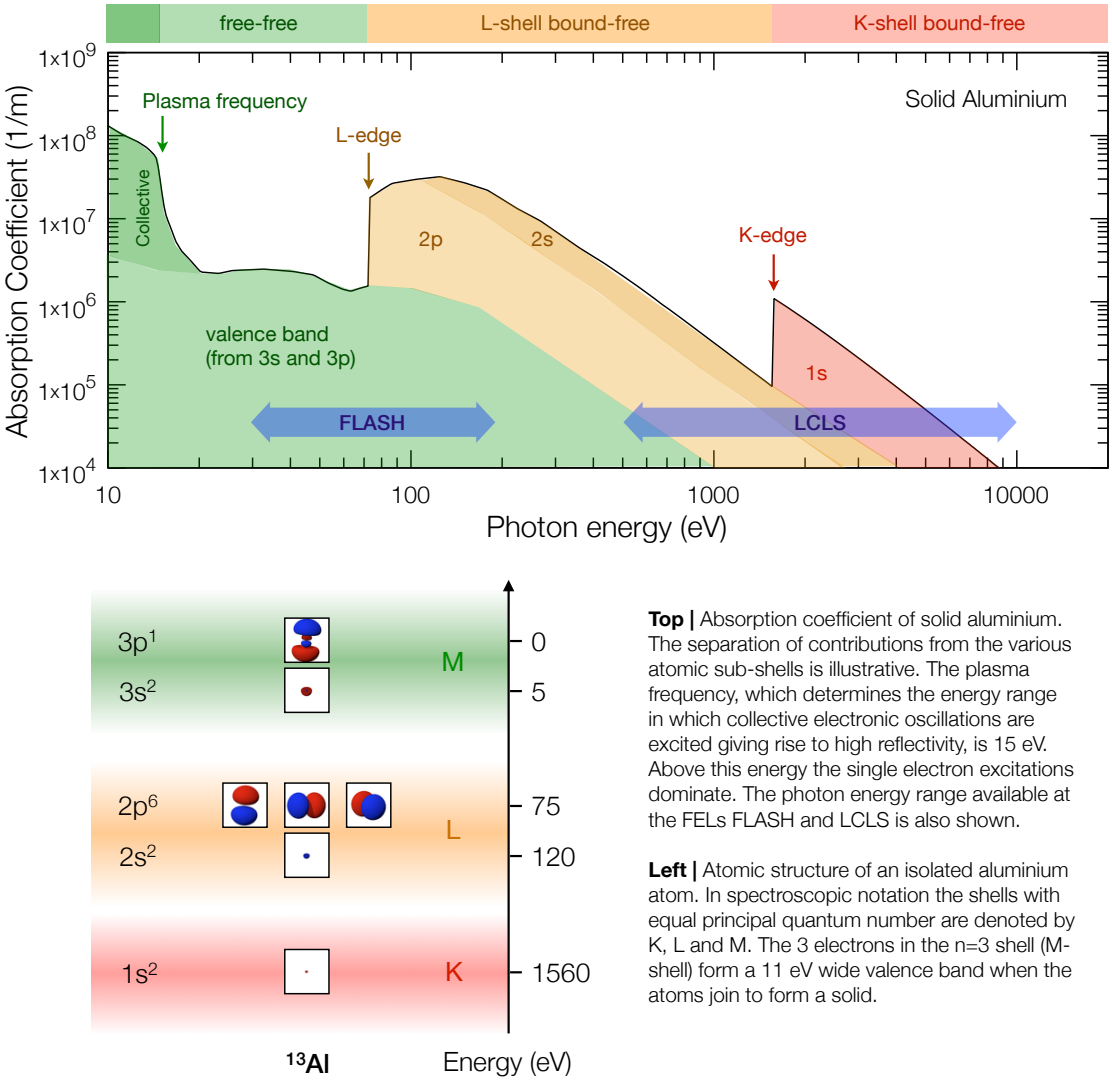

Top | Absorption coefficient of solid aluminium. The separation of contributions from the various atomic sub-shells is illustrative. The plasma frequency, which determines the energy range in which collective electronic oscillations are excited giving rise to high reflectivity, is 15 eV. Above this energy the single electron excitations dominate. The photon energy range available at the FELs FLASH and LCLS is also shown.

Left | Atomic structure of an isolated aluminium atom. In spectroscopic notation the shells with equal principal quantum number are denoted by K, L and M. The 3 electrons in the n=3 shell (M-shell) form a 11 eV wide valence band when the atoms join to form a solid.

Figure 1.1: Atomic structure and absorption coefficient of aluminium. The photon energy range is subdivided into three main regions depending on the type of absorption mechanism. The energies that can be reached with the FEL facilities FLASH and LCLS are shown by the blue arrows and are discussed in more detail in the text.

band density of states that is very similar to a free-electron gas, i.e., it increases roughly with the square root of the energy. This means that simple models assuming only a charge-neutral homogeneous electron gas, such as the jellium model, afford the possibility to describe the main physical properties of light interacting with these weakly-bound electrons. An illustrative depiction of the electronic states of Al is given in Fig. 1.1. The atomic structure translates into the main absorption features of the metal in a rather straightforward manner, as can be seen by the absorption edge features, related to the energies of atomic shells with decreasing principal quantum numbers.

Based on the nature of the participating electrons, the absorption energy spectrum can be separated into regions that exhibit physically distinct behaviour. In Al, the L-edge at around 73 eV defines the border region between the so-called *free-free* absorption at lower and the *bound-free* absorption at higher photon energies. Below this edge the photons do not have sufficient energy to excite a core state and only valence electrons participate in the absorption. The term free-free relates to the nearly free-electron nature of the delocalized valence electrons in both the initial and final states of a single photon absorption process. Core level electrons are on the other hand specific to a localized atomic bound state and the excitation process is hence dubbed bound-free[2]. For aluminium, the absorption spectrum can be subdivided into four bands shown colour-coded in Fig. 1.1: the sub-plasmon region, the region between the plasma frequency and the L-edge, the region between the L-edge and the K-edge, and the region with photon energy above the K-edge. Exciting a sample at energies below the plasma frequency is not particularly interesting as a method for volumetric high energy deposition due to the very large reflectivity that valence electrons in metallic samples exhibit in this regime. Higher photon energies are however very promising, and in this thesis I will address both free-free absorption, present below the L-edge, and bound-free absorption, which dominates above. In particular, it is important to notice that the FLASH FEL operates in an energy range which is well-suited for this kind of investigations. Furthermore, the Linac Coherent Light Source (LCLS) is an FEL which came into operation only recently and enables reaching much higher energies, extending beyond the Al K-edge.

of metals. Distinguishing valence and conduction bands however only makes sense in semiconductors, where a band gap is formed within the band created by the valence electrons. Thanks to our good fortune, this thesis is semiconductor-free and the conduction band nomenclature will not be needed.

[2]Note that the second *free* in this terminology originates from the atomic excitation in plasma physics where the electron is kicked out of the atom into the continuum. In a bulk solid this is generally not the case since, except from a very thin layer at the surface, the electrons are confined to the system due to rapid scattering with other electrons in the valence band.

1.1 Important concepts

Understanding the mechanisms of high intensity light-matter interaction and its implications related to the field of high energy density physics is the underlining theme of this thesis and the objective behind all the investigations that will be discussed. As mentioned, the primary focus will be on WDM. Part of the importance of the WDM regime lies in its strategic position in density-temperature phase space, which cannot be avoided if dense systems are to be heated to high temperatures. The experimental investigation of WDM, although challenging, is essential to this research and recently developed free-electron laser systems, as will be discussed in the following chapters, have proven invaluable in this regard. The difficulties encountered in obtaining reliable experimental data in the WDM regime are matched, if not surpassed, by those found in theoretical modelling. The theoretical approach that we have taken in the work here presented is mainly that of building on a reliable, fully quantum-mechanical model that describes successfully the physics of a solid state metal, and studying how high in temperature it can be pushed before its limits are reached. In this regard, the most promising results are given by finite-temperature density functional theory (FT-DFT). A brief introduction to WDM, FELs, and DFT is given below, as these will be widely referred to throughout this manuscript.

1.1.1 Warm dense matter

Warm dense matter is a state characterized by solid or near-solid densities and temperatures in the eV range, which places it between the condensed matter state (solid densities and low temperatures) and the classical plasma state (high temperatures and low densities). Two temperature-density diagrams, for hydrogen and aluminium, are shown in Fig. 1.2, showing the region of phase space occupied by warm dense matter.

A typical example of the occurrence of WDM in nature is in the interior of the giant planets and in brown dwarfs, which makes the understanding of this regime, and in particular of its equation of state (EOS), of significant interest to planetary astrophysics. For example, a prominent case where an accurate EOS of H and He in warm dense conditions is needed, together with the phase diagram of H/He mixtures, is that concerning the internal structure of Saturn and Jupiter. Several characteristic quantities of these planets can be measured, such as their luminosity, total mass, equatorial radius, temperature, angular velocity, gravitational moments and atmospheric He mass fraction, placing significant constrains on planetary models. Nonetheless, a homogeneous evolution model considering a radiating and internally isentropic planet, which accounts

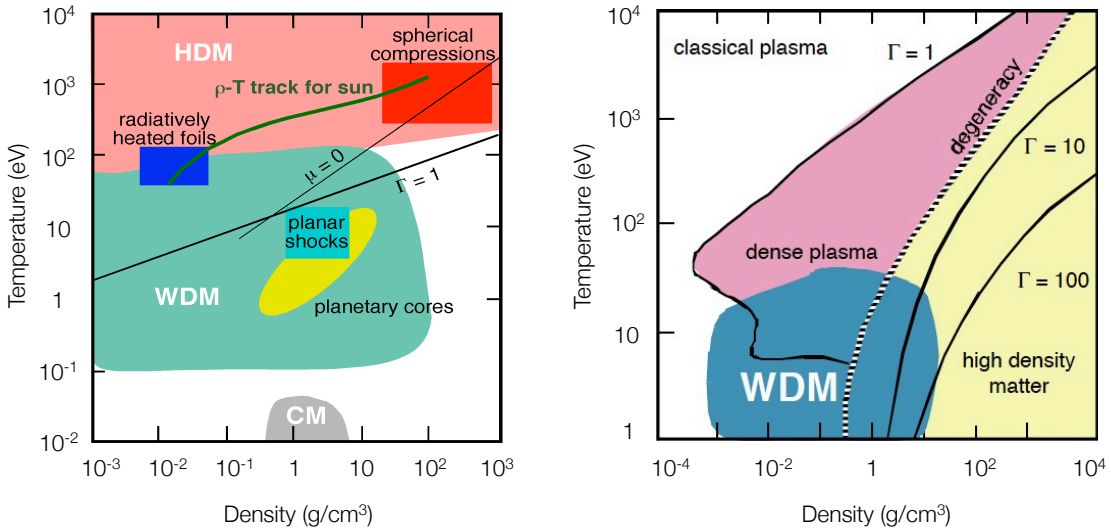

Figure 1.2: Temperature-density diagrams of hydrogen (left) and aluminium (right) illustrating the region of phases space occupied by the warm dense matter regime. On the plots μ indicates the chemical potential and Γ the plasma coupling parameter: the ratio of the Coulomb and kinetic energies. Images taken from [6].

for these observational constraints, predicts that Saturn is either roughly half the age of Jupiter, or alternatively, is far more luminous than would be expected. This is an important indication of a rich and complex internal structure, perhaps partially due to a phase separation of He from liquid metallic H within the planet [3, 4]. Clearly however, any quantitative modelling of this structure depends strongly on the phase diagram of H and He, and on their EOS in the WDM conditions of the planetary interior. These issues are not limited to Jovian giants but also apply to terrestrial planets, with a higher content of heaver elements, the EOS of which are also very poorly known at the relevant conditions, i.e. at pressures significantly above 200 GPa and temperatures of order 1 eV [5].

From the more immediate point of view of possible applications it is worth mentioning that any laboratory-created plasma obtained by the heating of a condensed matter sample, solid, gas or liquid, will have eventually transversed the WDM region of phase space. Such experimental investigations are becoming increasingly common with the development of high-intensity short-pulse laser systems, but are also of relevance for ion-beam driven plasmas, exploding wires and pinch devices. Perhaps the most important facet of this observation is that related to laser-driven inertial confinement fusion,

where the initially cold deuterium-tritium pellet must be heated and compressed to fusion conditions. The details on the interaction process between the fusion pellet and the radiation field – be it optical for direct-drive or x-ray for indirect-drive – are needed over a large range of densities, temperatures and pressures so as to enable the most efficient field-matter coupling possible. Again, the EOS, the radiative and the transport properties in the WDM state are essential pieces of information.

Naturally, to solve most of these issues a consistent EOS and radiative model is needed for all temperatures and densities, not only for the WDM state, so it might seem slightly peculiar at first to want to isolate this specific region of phase-space. There are two underlying motivations for this separation. The first is the intrinsically transient nature of the WDM regime, which is not only very short-lived, but also exhibits large temperature and density gradients even in minute samples, making the experimental investigation extremely challenging. The second motivation is theoretical and follows from the plasma parameter Γ, defined as the ratio between the potential energy, due to Coulomb inter-particle interactions, and the kinetic energy of the system. WDM is the region around the $\Gamma \approx 1$ line, where the two energies are comparable in size, as can be seen in Fig. 1.2. This situation raises formidable theoretical difficulties as standard perturbative expansions cannot be applied. So while various theoretical models having predictive capabilities in either the condensed matter or the hot plasma state can be constructed, the WDM region remains problematic. These difficulties further emphasise the need for accurate experimental investigations of the properties of WDM.

1.1.2 Free-electron lasers

Since their invention half a century ago, lasers have been radically transforming the way we do physics and have proven an invaluable tool to probe and study the world around us. The interaction between light and matter is probed using a combination of scattering and spectroscopic techniques, for instance absorption or emission spectroscopy, Thomson scattering, Raman scattering and x-ray diffraction. Conventional laser systems today can deliver exceptional performance in the key parameters for light-matter interaction studies: full pulse coherence, transform-limited femtosecond pulses and bandwidths, very high average and peak brilliances, etc. The wavelength of the radiation is perhaps the only foible, as for conventional lasers it is limited to the near-IR and visible region of the spectrum due to atomic structure constraint. This limits the spatial resolutions that can be obtained experimentally with such devices, and more pertinently to this thesis, the plasma densities that can be penetrated and probed.

These are important limitations which can only be addressed with higher energy radiation, such as XUV or x-rays. However, the generation of light at these wavelengths provides some significant challenges. Until recently, synchrotrons were the world's flag ship facility for x-ray production. These are cyclic accelerator-based devices, where electrons[3] are accelerated and curved by synchronized electric and magnetic fields. Typical operational energies are in the several GeV range. Light is generated from the electron beam by passing it through an undulator – a periodic structure of dipole magnets – which accelerates the relativistic electrons transversely to their path, causing them to radiate. The emitted radiation wavelength depends on the characteristics of the magnetic field in the undulator and on the electron beam energy, and can be tuned, ranging from the soft x-ray regime to hard x-rays above 60 keV (see, for example, the specifications of the ESRF synchrotron [7]). Synchrotrons are able to provide high quality, stable, bright and high-flux x-ray beams, however their beam coherence is limited, as the electrons emitting radiation are independent, and the pulse lengths are restricted by the electron bunches, and are generally not shorter than 30 ps. Beam slicing techniques can be employed to cut this number down to several hundred femtoseconds, but this is accomplished with a severe reduction in photon flux, making it unfeasible for many experimental purposes involving high energy density physics.

The absence of a brilliant, short pulse x-ray source led to the development of the x-ray laser in the 1980s and 1990s [8]. Here, the goal is to generate a population inversion in a hot plasma that is created by focusing a conventional laser on to a suitable target. Although not very efficient, the spectral brightness that can be achieved in the XUV with this method is significantly higher than that available at synchrotrons (see Fig. 1.3). This technique is still of interest as an intense laboratory x-ray source, however, the recent development of high brightness FELs in this regime, as will be discussed shortly, has rendered x-ray lasers to some degree obsolete. Furthermore, current research into high harmonic generation and into FELs based on laser wakefield acceleration are becoming increasingly promising as techniques to deliver small-scale, high brightness XUV and x-ray radiation sources.

A solution to several of the limitations that synchrotrons exhibit as light sources for ultra-fast science was to be the development of free-electron lasers. This name was coined by Madey in 1971 [10], however the first discussion of the underlining physical process was already published by Motz two decades earlier [11]. The basic concept of the process is fairly simple: an oscillating electron bunch is coupled to electromagnetic

[3]Naturally, other charged particles can also be used. Hadrons are used, for example, in the LHC at CERN.

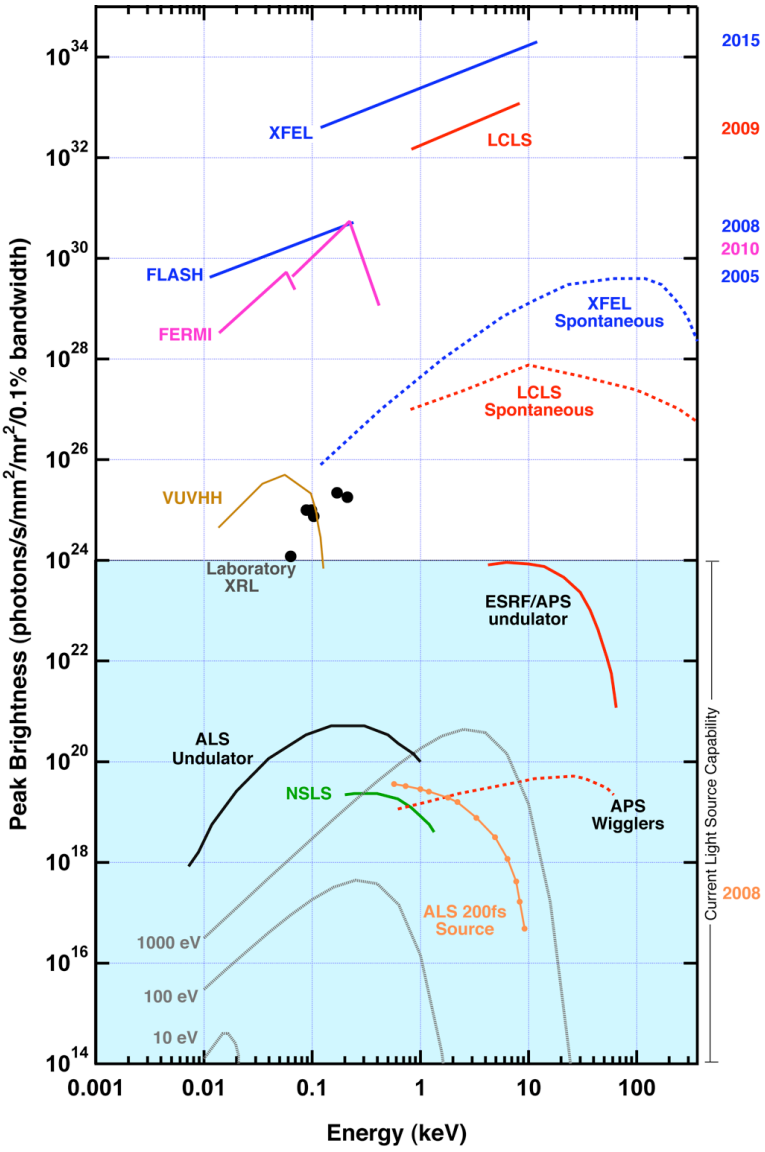

Figure 1.3: Peak brilliance of 3rd generation synchrotrons, x-ray lasers, VUV high harmonic generation sources and FELs.

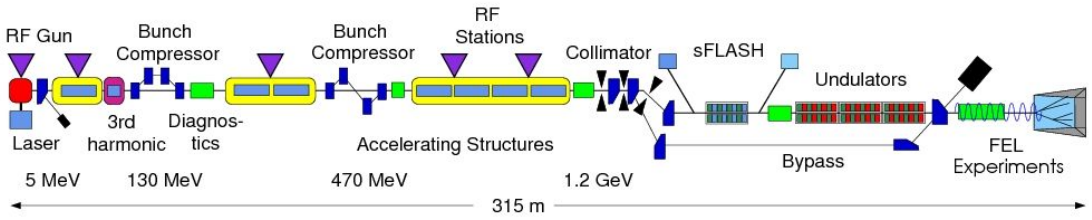

Figure 1.4: Schematic view of the FLASH free-electron laser at DESY. Image courtesy of DESY website [9].

radiation and is used as a gain medium, in a setup that schematically resembles that of conventional lasers. The radiation field causes stimulated emission to take place from the electrons, provided certain constrains are met, and is amplified [12]. The gain obtained in this manner can increase the radiative power of the photon field drastically, up to a threshold value. The first FEL operating above threshold was reported in 1977 [13] at a wavelength of 3.4 μm.

Initially, FELs were based on oscillators with cavities and mirrors surrounding the undulators to couple the photon field to the electrons. While this is viable for long wavelength radiation, the lack of efficient reflective optics at below-optical wavelengths provided a push for a new operating scheme. The design that was developed is the single-pass, self-amplification of spontaneous emission (SASE) FEL that is the base of today's 4^{th} generation light sources. Here the radiation field builds up from noise in the undulator and is coupled to the electron bunch, leading to a density modulation, or micro-bunching, which enhances the power and coherence of the radiation during a single pass through the undulator system. Reaching the amplification threshold within a reasonable undulator length however means that the quality prerequisites on the electron beam are extremely stringent and can generally only be obtained with a linear accelerator.

The first demonstration of SASE FEL operation took place in 1997 [14], at a wavelength of 12 μm. Three years later, SASE FEL saturation was demonstrated at the visible wavelength of 390 nm [15]. Since then, several improvements have been achieved and the radiation wavelength has been slowly pushed down to encompass the water window (23–44 Å) [16, 17, 18, 19]. An important landmark was the beginning of operation as a user facility of FLASH (Free-electron LASer in Hamburg) in 2005 [20], which remains at the time of writing the only XUV FEL available for user operation worldwide. A schematic layout of FLASH is shown in Fig. 1.4. A major advance in the field was achieved in 2009 with the observation of saturation at the wavelength of 1 Å at the Linac

Coherent Light Source (LCLS) FEL at SLAC [21]. This is the worlds first, and currently only, x-ray FEL and represents the first true 4^{th} generation light source. In the next few years, several new FELs will start operation: Fermi@elettra in Italy in the XUV, and the SPring-8 Compact SASE Source in Japan (SCSS) and the European XFEL in Germany in the x-ray region.

Compared with synchrotron light sources, SASE FELs can deliver up to 10 orders of magnitude higher peak brilliances, as is illustrated in Fig. 1.3. Due to the micro-bunching of the electron beam and the SASE operation the pulse lengths are also extremely short, from 100 fs down to below 10 fs in the low bunch-charge mode. The FEL pulse also exhibits almost full transverse coherence. Importantly, the wavelength can be tuned over an extended range.

1.1.3 Density functional theory

Whilst the use of FEL radiation represents the main basis of the experimental work presented in this thesis, most of the theoretical calculations are based on density functional theory. It will be useful to introduce some basic concepts that will be referred to in the following chapters.

Density functional theory was introduced in a seminal paper by Hohenberg and Kohn in 1964, and has since become the most widely used concept in electronic structure calculations. It won Kohn the Nobel prize in Chemistry in 1998. The basics of DFT are covered in almost all books on solid state physics and will be introduced here only briefly as certain concepts will be used later in the thesis. For the following I will follow closely the discussion given in [22, 23] and the reader may want to consult these references for further details.

The standard many body system composed of N-electrons in a periodic potential is described by the following Hamiltonian:

$$\mathcal{H} = \sum_{l=1}^{N} \left(\frac{p_l^2}{2m_e} + V(\mathbf{r}_l) \right) + \frac{1}{2} \sum_{k,l=1;k\neq l}^{N} v(\mathbf{r}_l - \mathbf{r}_k), \tag{1.1}$$

with the Coulomb potential given by

$$v(\mathbf{r}_l - \mathbf{r}_k) = \frac{e^2}{4\pi\epsilon_0 |\mathbf{r}_l - \mathbf{r}_k|}, \tag{1.2}$$

and the term $V(\mathbf{r}_l)$ containing the ion-ion and electron-ion interactions, with $\mathbf{R}_i$ indi-

cating the equilibrium position of the i-th ion:

$$\sum_l V(\mathbf{r}_l) = \sum_{n,l} v(\mathbf{r}_l - \mathbf{R}_n) + \frac{1}{2}\sum_{n,m} V(\mathbf{R}_n - \mathbf{R}_m). \tag{1.3}$$

The problem consists in solving the eigenvalue equation

$$\mathcal{H}\Psi_N = E_N\Psi_N, \tag{1.4}$$

where Ψ_N is the many body wavefunction. This is a formidable challenge. The question is then whether Eq. (1.4) can be in some way decoupled into a set of solvable single-particle Schrödinger equations, valid for all the electrons, of the form

$$\left(-\frac{\hbar^2}{2m_e}\nabla^2 + V_{\text{eff}}(\mathbf{r})\right)\psi_\alpha(\mathbf{r}) = E_\alpha\psi_\alpha(\mathbf{r}), \tag{1.5}$$

with α indicating a complete set of quantum numbers and V_{eff} some effective transformation potential that needs to be found. The first successful attempt at this, historically, was the Hartree approximation, where Ψ_N is considered to be composed of a direct product of single-particle wave functions ψ_α, and the Hartree-Fock approximations where a Slater determinant is used to explicitly consider the contribution of Coulomb exchange. Density functional theory can be considered an extension of these methods as it further includes the contributions due to electron correlations in the effective potential.

The first important step towards the DFT description of a many body system is the Hohenberg-Kohn theorem [24], which gives the theory its name, and states that the ground state energy, E_0, of a N-electron system, for a given external potential V, is a unique functional of the single-particle density $n(\mathbf{r})$:

$$E_0 = \langle\Psi_0|T + V + U|\Psi_0\rangle = E_V[n(\mathbf{r})], \tag{1.6}$$

with T indicating the kinetic energy and U the energy due to electron-electron interactions. Importantly, this theorem says that only the 3-dimensional electron density is needed to obtain the ground state energy, or indeed the expectation value of any observable in the ground state, rather than the full $3N$-dimensional Ψ_N. The theorem also states that the ground state minimizes the energy functional:

$$E_V[n(\mathbf{r})] = T_s[n(\mathbf{r})] + \int V(\mathbf{r})n(\mathbf{r})\mathrm{d}^3\mathbf{r} + \frac{e^2}{2}\iint \frac{n(\mathbf{r})n(\mathbf{r}')}{4\pi\epsilon_0|\mathbf{r}-\mathbf{r}'|}\mathrm{d}^3\mathbf{r}\mathrm{d}^3\mathbf{r}' + E_{\text{xc}}[n(\mathbf{r})], \tag{1.7}$$

which contains the kinetic functional of the non-interacting electron system T_s, the energy of the electron density in the external field, the Hartree direct term and the exchange-correlation energy functional. This minimum can be obtained by a variational approach, representing the density by a complete set of single particle wave functions $\psi_\alpha(\mathbf{r})$

$$n(\mathbf{r}) = \sum_{\alpha=1}^{N} |\psi_\alpha(\mathbf{r})|^2, \qquad N = \int n(\mathbf{r}) \mathrm{d}^3\mathbf{r}, \tag{1.8}$$

and taking the functional derivatives with respect to $\psi^*_\alpha(\mathbf{r})$. This leads to the Kohn-Sham equations – a set of Schrödinger-like equations for the single particle functions $\psi_\alpha(\mathbf{r})$:

$$\left(-\frac{\hbar^2}{2m_e}\Delta + V(\mathbf{r}) + e^2 \int \frac{n(\mathbf{r}')}{4\pi\epsilon_0 |\mathbf{r} - \mathbf{r}'|} \mathrm{d}^3\mathbf{r}' + V_{\mathrm{xc}}(\mathbf{r}) \right) \psi_\alpha(\mathbf{r}) = E_\alpha \psi_\alpha(\mathbf{r}). \tag{1.9}$$

The exchange-correlation potential is given in terms of the exchange-correlation energy as

$$V_{\mathrm{xc}}(\mathbf{r}) = \frac{\delta E_{\mathrm{xc}}[n]}{\delta n(\mathbf{r})}, \tag{1.10}$$

which can be computed assuming an appropriately simplified form for the exchange-correlation energy, such as, for instance, the local density approximation (LDA). Here the exchange-correlation energy per electron is taken to be that of the uniform electron gas, or jellium, ϵ_{xc}, with density n:

$$E_{\mathrm{xc}}[n(\mathbf{r})] \Rightarrow E_{\mathrm{xc}}^{\mathrm{LDA}}[n(\mathbf{r})] = \int n(\mathbf{r}) \epsilon_{\mathrm{xc}}(n(\mathbf{r})) \mathrm{d}^3\mathbf{r}. \tag{1.11}$$

The LDA has been seen to be a moderate-accuracy approximation that captures the general trends, is well behaved and reliable. More accurate results can be obtained by considering the exchange-correlation functional to depend on, in addition to the electron density as given in Eq. (1.11), also its first derivative

$$\epsilon_{\mathrm{xc}}^{\mathrm{LDA}}[n(\mathbf{r})] \Longleftrightarrow \epsilon_{\mathrm{xc}}^{\mathrm{GGA}}[n(\mathbf{r}), \nabla n(\mathbf{r})] \tag{1.12}$$

Several such functionals are currently available and they go under the name of the generalized gradient approximation (GGA). The particular parametrisation which was used in all the DFT results presented in this thesis is due to Perdew, Burke and Ernzerhof (PBE-GGA) [25]. We further note that the spin contribution can also be accounted for, if needed.

The standard DFT calculation of the electronic structure is conducted in an iterative way. First the external potential V is given in terms of the ions and their positions in the calculation cell. A single particle test-density is then chosen, the direct and exchange-correlation terms calculated, and the Schrödinger equation in Eq. (1.9) solved, yielding the occupied electron states. With these, a new electron density is calculated and the loop is repeated. This takes place until the densities or the energy eigenvalues converge to the desired accuracy, providing a self-consistent solution for the electron energies and wave functions.

Shortly after its introduction, Mermin demonstrated that the Hohenberg-Kohn theorem was extendable to an inhomogeneous electron gas at finite temperatures [26]. This important finding is the basis of finite-temperature DFT (FT-DFT), essential for modelling systems at temperatures which are not significantly lower than their Fermi energies. Warm dense matter is an excellent example of such a system, with temperatures in the 1-10 eV range. As mentioned previously, analytical evaluations of structural properties of WDM is a challenging task; it is being tackled from two main directions. One is a top-down approach, which consists in trying to find ways to modify existing classical plasma models[4] to incorporate the degeneracy and quantum correlations that are of importance at lower temperatures and higher densities. The other is a bottom-up approach, where established condensed matter theories are pushed to their temperature and pressure limits. In this context, the terms *up* and *down* refer to the extension of a model according to the phase space illustrated in Fig. 1.2. Finite-temperature DFT, often coupled through the Born–Oppenheimer approximation to classical molecular dynamics (MD), is an example of this bottom-up approach, and is proving very useful for systems in a variety of conditions ranging from high-pressure phase transition studies to laser-generated solid density plasmas.

Despite showing great promise, calculations are hindered by the often prohibitive computational constraints, which limits work to large computers and relatively small and simple physical systems. As such, a common use of FT-DFT-MD calculations is to benchmark plasma codes in a limited range of very specific physical conditions. It is these top-down codes that are then used in data analysis and experiment planning, as they are much faster and more efficient. Another problem that DFT calculations face is the accuracy of pseudopotentials – the performance-enhancing effective potentials used to substitute the Coulomb ion potential – used in the calculations. This issue is strongly pertinent to the DFT-based calculations that will be discussed in this thesis and will be

[4]The term classical is used loosely in this context, to indicate a model that is not fully quantum-mechanical.

addressed in the following chapters.

1.2 Thesis structure

The content of this thesis is divided into six chapters. The first chapter is introductory in nature and aims at providing a basic description of the main topics discussed in the thesis. In particular, a brief description is given of WDM, FEL operation and facilities worldwide and of DFT, which has been used extensively to perform electronic structure calculations from first principles. The author's contributions to the results presented are also outlined.

The following four chapters represent the core of this work and are focused around the different regions illustrated in Fig. 1.1. They follow closely the line of experimental and theoretical investigations the author was involved in during the past three years. As the scope of this discussion is to elucidate the new results obtained, no particular care has been taken to separate the experimental and theoretical research, which are rather presented conjointly. It is hoped that this will prove beneficial to the reader.

Chapter 2 is theoretical in nature and is aimed at discussing the physical process of free-free absorption in the XUV region of the electromagnetic spectrum. Free-free absorption is a plasma physics term indicating the interaction of light with free electrons, as opposed to bound-free absorption, in which the interaction concerns electrons that are initially located in a bound atomic state. The underlying mechanism of free-free absorption in plasma physics is inverse bremsstrahlung. This model, which is successfully used to describe low-density and high-temperature systems, is introduced and discussed briefly. The extrapolation of standard inverse bremsstrahlung methods to systems approaching solid densities and temperatures of order 1 to 10 eV has, however, proven rather challenging, as can be seen by the severe degradation in predictive capabilities of plasma opacity codes in these conditions. This chapter is dedicated to the investigation of some of these issues in the particular case of aluminium, by means of both a semi-analytical model and finite-temperature density functional theory calculations. A natural link exists between the calculations and recent XUV FELs such as FLASH in that these facilities offer, for the first time, the opportunity to efficiently create and probe the free-free opacity in warm dense systems and hence to benchmark the theory in this notoriously elusive regime, of great significance to a variety of fields ranging from astrophysics to laser-driven inertial confinement fusion research. The results presented in this chapter were published in High Energy Density Physics in 2009 [27].

Chapter 3 introduces the idea of radiative heating of thin foils as a viable technique

for homogeneous WDM generation. In this context we have used the FLASH XUV FEL facility in Hamburg, which has proven to be exceptionally well suited for this kind of research. The facility is introduced, together with its basic operating parameters. The first step in this research was the construction of an experimental setup on FLASH, enabling the delivery of high intensity XUV radiation – the microfocusing setup on beam line BL3. This setup is described, together with the efforts made to measure and characterize the beam profile and the radiation intensity. Of significance is the achievement of focal spot sizes below 1 μm FWHM, corresponding to record-high intensities of 10^{17} Wcm^{-2} at an XUV photon energy of 92 eV. The results of this work were published in Optics Express in 2009 [28].

Chapter 4 discusses the first experimental results obtained using the microfocusing setup, described in Chapter 3. These investigations led to the first observation of saturable absorption at above-optical wavelengths in solid density samples. Tuning the FEL wavelength to a core electron excitation channel in aluminium, it was possible to saturate the absorption transition and render a thin foil transparent to the pulse on femtosecond timescales. These findings were published in Nature Physics in 2009 [29].

Chapter 5 describes the results obtained from XUV spectroscopy at FLASH. These investigations were done in part concomitantly with the absorption measurements, albeit on thicker aluminium samples, and in part during the following beam time on FLASH. The emission I will focus on is the fluorescence obtained by the radiative recombination of a valence electron filling a $2p$ core state hole, in solid density aluminium. We have noticed that this spectrum yields important information on the electron valence band density and temperature on femtosecond time scales and can be useful to characterize the sample properties after energy deposition, but prior to the evolution to the warm dense state. Theoretical investigations using FT-DFT have been undertaken to understand the electronic structure in Al and how it changes under these highly excited conditions, in addition to investigating the degree of sensitivity that soft x-ray emission spectroscopy has to any such changes. These results were published in Physical Review Letters in 2010 [30].

The final, sixth, chapter is a summary of the work done and the results obtained. It also briefly introduces some new ideas and outlines future work.

1.3 Author contributions

Much of the work presented in this thesis is part of a collaborative research effort. This is true in particular for the experimental work undertaken on the FLASH facility.

Beam time allocation on this remarkable FEL is extremely competitive and the time given per single experiment is limited. This is mainly due to it being a unique place to conduct high-intensity XUV experimental work. As such, a large collaboration was established – dubbed the Peak Brightness Collaboration (PBC) [31] – uniting researchers from numerous institutes worldwide with a variety of different research interests but motivated by the same desire to use this novel source of XUV light for exciting new science. The author, who has been an active member of this collaboration for the past three years, would like to acknowledge its many members and their contributions to that portion of successful experiments that are presented in this thesis. This thesis has nevertheless been structured in such a way as to emphasise the topics where the author's contributions have been essential. Where others have contributed significantly to the results presented, this will be clearly indicated in the text. As such, this thesis is not meant to be a compilation of all the work undertaken by the author nor by the PBC in the discussed fields. It is anticipated that the curious reader will find further information in this regard by consulting the extensive list of references given at the end of the manuscript. Naturally, my supervisor, Professor Justin S. Wark, has had a vital role in all aspects of the work presented herein.

The thesis is divided in six chapters, with the four middle chapters containing the research carried out. The first chapter is introductory and the last contains conclusions and future plans.

Chapter 2 is the work of the author with the exception of the FT-DFT calculations, which were conducted by Dr. Michael P. Desjarlais from Sandia National Laboratories, Albuquerque, USA, who is also acknowledged for providing his most recent DFT-MD results for the cold Al system before official publication. Vital discussions with Dr. Gianluca Gregori from the University of Oxford, concerning all aspects of this investigation, are further acknowledged.

The author contributed to the microfocusing experimental campaign that is discussed in Chapter 3 and in particular, worked on the experimental setup, the alignment of the optical system, monitoring FEL operation and data acquisition. The experimental beam time was led by Dr. Arthur J. Nelson from Lawrence Livermore National Laboratory, USA. Theoretical work on the beam characterization and spot size measurements were conducted through a joint effort by the group of Professor Libor Juha from the Czech Institute of Physics in Prague, in particular by Jaromir Chalupsky, and Dr. Jacek Krzywinski from the SLAC National Accelerator Laboratory, USA.

Chapters 4 and 5 discuss experimental work on FLASH which was undertaken by the author, together with many members of the PBC. For a full list of people involved the

reader may consult the extensive author lists in the two main publications [29, 30]. The theoretical investigations and data analysis presented in these chapters have been done by the author[5]. Relevant contributions to the work presented and acknowledgments of useful discussions are however in particular due to a number of people: Dr. Bob Nagler, a former postdoc in our group in Oxford, for a list of things too long to quote, Dr. Ryszard Sobierajski from the Polish Academy of Sciences in Warsaw, for valuable discussions regarding the transmission data analysis, Ulf Zastrau from the University of Jena, Germany, for the soft x-ray emission spectra extraction and discussions, and Dr. Stephane Mazevet from CEA, DAM, DIF, France, for his contributions to the core-hole pseudopotential approach to modelling photo-excited matter.

[5]The saturable absorption model presented in [29] is due to Dr. Bob Nagler and differs to the simple model presented in this thesis.

CHAPTER 2

Free-free Absorption in Warm Dense Aluminium

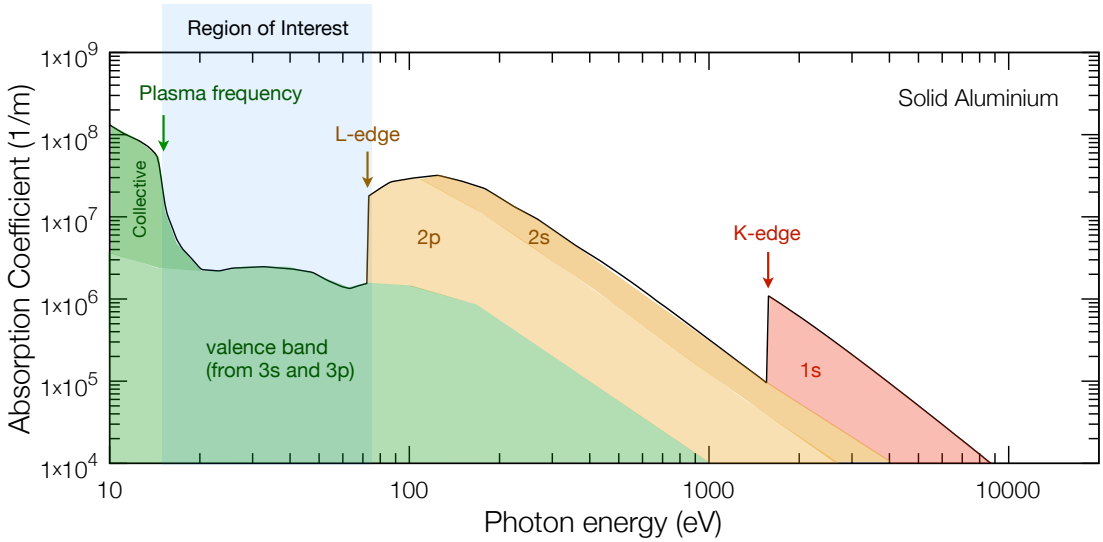

2.1 Introduction

Determining the opacity of a material in the XUV region of the spectrum as it makes the transition from a cold solid to a hot plasma is a problem that both tests our fundamental understanding of how light interacts with matter, and is of increasing experimental interest due to the development of intense XUV free-electron lasers. From the applied physics point of view, free-free absorption in dense samples is of great interest because it is an important energy absorbing mechanism of a deuterium-tritium plasma in an inertially confined laser-driven fusion process [32].

The FLASH XUV-FEL has been introduced in the previous chapter, where it was shown that its extremely high peak brilliance allows for record high intensities in the XUV region of the spectrum. A thin foil placed in the focus of such a beam can be rapidly heated to several tens of eV, and during this absorption process we expect significant changes in the opacity. To understand the microscopic details of the rapid heating and provide a predictive capability for experimental design, a consistent absorption model is required. A complete model, which covers a wide range of densities, temperatures, and incident photon energies would need to include sophisticated atomic physics that accounts for both bound-free and free-free absorption, and includes the dependence on charge state upon heating, density and ionization. The ability to separate the contributions of these different mechanisms is of great importance because it provides the opportunity to model the role that each has to play in the opacity of dense plasmas.

In this context, the opacity of warm dense Al in the XUV regime is of particular interest. The valence band of Al is nearly-free-electron-like and there is a considerable expanse of energy space where nearly free-electron theory might be applicable, i.e., between the plasmon frequency at 15 eV and the L-edge at 73 eV. For photon energies above the L-edge, both valence band (free-free) and core-electron absorption (bound-free) take place, however at lower energies, no bound states can be excited and Al becomes a prototypical free-electron system. Nonlinear effects such as multi-photon absorption could void this statement at increasingly high intensities, however, as these effects are also proportional to the square of the wavelength, they are negligible in the XUV region even well beyond the currently attainable 10^{17} Wcm^{-2} intensity regime[1]. Importantly, calculations of the equation of state of Al indicate that at solid density and in thermal equilibrium, ionization of the L-shell does not occur for electron temperatures below the Fermi temperature (11 eV) [33]. Thus, with a known free-electron density and ionic state over a wide temperature range, Al is an ideal material to test our understanding

[1]The experimental achievement of such high intensities is the topic of the next chapter.

of free-free absorption in warm dense matter. Despite all this, significant difficulties have arisen both experimentally and theoretically in the investigation of the free-free absorption, even in the simplest experimental conditions, such as the solid state at room temperature. Although the solid state absorption might not seem directly relevant to the title of this chapter, it is important to note that until we are able to describe the basic absorption mechanisms at every-day conditions, little insight can be truly gained in the more complex study of the change in opacity of a sample heated from the solid state to the warm dense matter regime. I will give a brief description of some of the issues encountered, which will be described in more detail throughout the chapter.

The accurate determination of the opacity of solid state, crystalline Al in the XUV, while seemingly a rather simple problem, was historically hindered by the lack in availability of an intense and continuously variable XUV light source. The recent development of both XUV FELs and, perhaps more importantly in this context, high harmonic generation (HHG) laser light sources, has responded to this problem and made this wavelength range easily accessible [2]. In these setups, as well as in plasma x-ray laser experiments, Al is a commonly used filter material, which has exposed a rather interesting problem: the two most often used tabulated opacities in the XUV, which were experimentally measured first by Henke and collaborators [34] and shortly after by Gullikson and collaborators [35], when compared, differ significantly. For photon energies above the L-edge, the same measurements are in much better agreement. Part of the problem lies is the difficulty of treating the contribution to the opacity of the oxide layer, which is always present on an Al foil. We note that the Gullikson paper claims to have measured the oxide thickness (4 nm on each side of the foil) and accounted for it. However, a more ingenious way of considering and excluding the contribution of the oxide layer was used in the x-ray laser measurements by Keenan and co-workers [36], by using a step target. Their results are reported to be in good agreement with those of Henke and in conflict with those of Gullikson. Accurate experimental results for dense plasmas are unfortunately currently unavailable.

Theoretically, the problem of the opacity of solid state Al in the XUV has been addressed by Sturm and co-workers within the random-phase approximation (RPA), who found the discrepancy between the measured and calculated results to be significant [37].

In order to theoretically study the opacity of a warm dense system, two possible routes may be taken. A solid state approach would involve finding a consistent extension of the theory to account for finite temperatures. The plasma approach on the other hand

[2] Although XUV FELs are rare, large and expensive facilities, HHG setups are becoming increasingly standard in University-scale laser laboratories.

is inverse: plasma models work very well for dilute and hot systems and the challenge is to extrapolate the predictions to cooler and denser systems. Several plasma opacity codes based on inverse bremsstrahlung are available, such as for example the Cassandra code [38], which can calculate the opacity of Al plasmas for a range of temperatures, densities and ionization states. Unfortunately, such codes are generally quite poor in reproducing solid state results where degeneracy and quantum correlations start playing important roles. In particular, for photon energies just above the plasmon frequency in Al, this code overestimates the absorption coefficient by about an order of magnitude. On the other hand, Iglesias has shown in a recent publication that a plasma opacity model based on inverse bremsstrahlung can yield good results in the XUV also for solid-state systems, provided the scattering is considered to all orders in the potential [39].

Finding a reliable opacity model for warm and dense systems, be it analytical or computational, is a current field of active research. In the following I will discuss the work done on this topic which conceptually follows the idea of heating-up a solid state system. This approach was chosen since it closely resembles the actual experimental process of creating high energy-density matter from solid targets with intense radiation. Moreover, it is in line with the first principle approach of finite-temperature density functional theory, which is proving to constitute one of the most powerful tools available today for studying strongly coupled systems.

2.2 Absorption coefficient and the dielectric function

In electromagnetism, the dielectric function is defined as the quantity which connects the displacement field, $\mathbf{D}$, with the electric field, $\mathbf{E}$, according to

$$\mathbf{D}(\mathbf{k},\omega) = \epsilon_0\,\epsilon(\mathbf{k},\omega)\mathbf{E}(\mathbf{k},\omega). \tag{2.1}$$

The real part of $\epsilon(\mathbf{k},\omega)$ relates the amplitudes of the external and induced fields and therefore gives the screening, while the imaginary part describes the energy dissipation. The dielectric function describing the interaction of matter with electromagnetic radiation of frequency ω is given by taking the limit where the scattering vector $\mathbf{k}$ goes to zero:

$$\epsilon(\omega) = \lim_{\mathbf{k}\to\mathbf{0}} \epsilon(\mathbf{k},\omega), \tag{2.2}$$

In turn, intuitively, the absorption of light is defined through the absorption coefficient $\kappa(\omega)$ as the rate at which the initial intensity of the field I_0 decreases with penetration

into the material along a given direction x:

$$I(x) = I_0\, e^{-\kappa(\omega)x}. \tag{2.3}$$

Since the radiation intensity is proportional to the square of the electric field, it is easy to see that the absorption coefficient and the macroscopic dielectric function are related through the simple equation:

$$\kappa(\omega) = \frac{2\omega}{c}\mathrm{Im}\sqrt{\epsilon(\omega)}, \tag{2.4}$$

where c is the speed of light. All the information on the absorption is contained in $\epsilon(\omega)$, which can be calculated in different approximations based on the system under consideration and the region of parameter space of interest.

The elementary process of light absorption is due to the interaction of photons and electrons. In an atom there are typically two 'types' of electrons, based on the binding energy with the ionic core: the tightly bound, inner electrons and the nearly-free outer electrons. Assuming the final electron state to be free-electron like, we can separate the contributions to the absorption at a certain photon energy in bound-free or free-free processes, based on the initial state of the electron.

The simplest form of $\epsilon(\omega)$ is that initially proposed by Drude over a century ago:

$$\epsilon(\omega) = 1 - \frac{\omega_p^2}{\omega^2[1 + i\nu/\omega]}. \tag{2.5}$$

It includes a collision frequency parameter ν and hence describes the dielectric processes as due to collisional scattering within the material. Having been proposed before the advent of quantum mechanics, this form is classical. Here $\omega_p^2 = e^2 n/(\varepsilon_0\, m_e)$ denotes the square of the plasma frequency, with n and m_e the electron density and mass.

Interestingly enough, given the correct collision frequency, the low-frequency optical properties of a variety of systems are well described in terms of a Drude function. Absorption in a classical plasma, or the DC conductivity in simple metals, are both examples of such systems. This model is rather basic and most of the interesting physics is hidden in the collision frequency term. Unfortunately, a calculation from first principles of the collision frequency (or its inverse, the relaxation time τ) is hindered by the fact that it cannot be rigorously defined in terms of a correlation function in the theory of

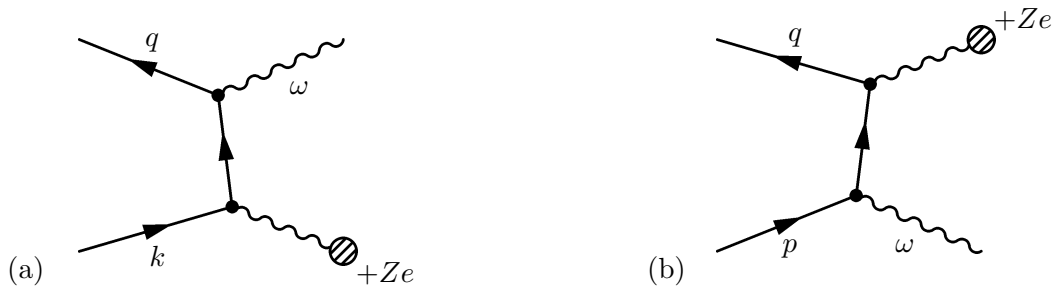

Figure 2.1: Feynman diagram for bremsstrahlung (a) and inverse bremsstrahlung (b).

linear response, i.e. written as a generalised Kubo formula:

$$\chi_{\mathrm{AB}}(\omega) = \frac{i}{h}\int_{-\infty}^{+\infty} d\tau \mathrm{e}^{i\omega\tau}\theta(\tau)\langle[\hat{A}(\tau), \hat{B}(0)]\rangle. \tag{2.6}$$

Here $\hat{A}$ is the measured observable, $\hat{B}$ the observable appearing in the perturbation (Hermitian adjoint of $\hat{A}$) and χ is the response function. $\theta(\tau)$ is the step function in 0. Of particular interest for discussing the process of absorption (and emission) are the electrical conductivity $\sigma(\omega)$ and the dielectric function $\varepsilon(\mathbf{q}, \omega)$:

$$\frac{1}{\varepsilon(\mathbf{q},\omega)} = 1 + v_{\mathbf{q}}\frac{i}{h}\int_{-\infty}^{+\infty} d\tau \mathrm{e}^{i\omega\tau}\theta(\tau)\langle[N_{\mathbf{q}}(\tau), N_{-\mathbf{q}}(0)]\rangle, \tag{2.7}$$

$$\sigma(\omega) = \frac{i}{\hbar\omega}\int_{-\infty}^{+\infty} d\tau \mathrm{e}^{i\omega\tau}\theta(\tau)\langle[j(\tau), j(0)]\rangle, \tag{2.8}$$

which can be written as Kubo formulas and are given as correlation functions of the number (or density) fluctuations $N_{\mathbf{q}}$ and of the current density j, respectively. It is in this sense that the assumption of validity of the Drude expression for the dielectric function given in Eq. (2.5) is needed to define the absorption collision frequency.

2.3 Inverse bremsstrahlung

Bremsstrahlung is the process of emission of radiation due to the deceleration of electrons in a material. One of the two Feynman diagrams of such a process, where upon scattering on an ion, the electron with momentum k emits a photon and scatters into an electron with momentum q, is given in Fig. 2.1, diagram (a). The process of inverse bremsstrahlung (IB) is shown in (b), where a photon is absorbed by an electron, which due to the interaction with an ion experiences a change in its momentum from p to

q. This is the lowest order diagram of single photon absorption and the relative cross sections are known results from quantum electrodynamics.

The total rate of absorption, R, is calculated in the following manner[3]: consider shining photons with frequency ω through an absorber and measuring the amount of photons in transmission. The probability of the photons being absorbed is given by the IB graph in Fig. 2.1 (b). On the other hand it could occur – with probability given by Fig. 2.1 (a) – that a photon with frequency ω is emitted from the absorber. Since this photon would be undistinguishable from the others it needs to be considered. Such emission enhances the transmission, i.e., reduces the absorption, by the probability (a). We therefore have

$$R(p,\omega\to q)=\frac{\pi c^3E_0^2n_i}{8\hbar\omega^3m_e}\left[k\frac{\mathrm{d}\sigma(k\to q,\omega)}{\mathrm{d}\omega}-q\frac{\mathrm{d}\sigma(q\to p,\omega)}{\mathrm{d}\omega}\right]. \tag{2.9}$$

Here we have tacitly used the fact that (a) and (b) are actually the same physical process and have the same bremsstrahlung cross section. Angle and polarization averaged, it is given by [40]:

$$\frac{\mathrm{d}\sigma(k\to q,\omega)}{\mathrm{d}\omega}=\frac{8\pi^3Z^2n_i^2E_0^2qk}{3\hbar(k-q)^2\omega^4}\frac{-\mathrm{d}|F(\xi)|^2/\mathrm{d}\xi}{[1-\exp(-2\pi\eta_k)][\exp(2\pi\eta_q)-1]}. \tag{2.10}$$

Here $F(\xi)=F(i\eta_k,-i\eta_q,1;\xi)$ is the hypergeometric function and

$$\begin{aligned}\xi&=-4kq/(k-q)^2,\\ \eta_q&=Ze^2m_e/\hbar q.\end{aligned} \tag{2.11}$$

The ratio η is known as the Coulomb parameter and depends on the momentum ratio between bound and free electrons. Free electrons with momentum p larger than the bound electron momentum are said to be fast ($\eta_p<1$) and if the opposite is true they are said to be slow ($\eta_p\geq 1$).

In the present picture, the electron involved in the absorption or emission is non-interacting with any other electrons in the system, i.e., there are no electron correlations involved. The simple extrapolation of this microscopic picture to a macroscopic system is therefore limited to systems where electron degeneracy has little to no effect, such as very dilute systems, systems at high temperature, or an appropriate combination of the two. A hot, low density plasma is a good example of such a case. This is the reason why IB is often called a classical theory - because the passage to a macroscopic absorption

[3]For the German reader, this process is described fully in the PhD thesis of A. Tronnier [42].

theory assumes a macroscopically classical system. The microscopic theory is however based on relativistic quantum mechanics.

2.3.1 Hot plasma regime

Consider a hot plasma where the electrons are fast ($\eta < 1$) and have a kinetic energy that is much greater than the photon energy:

$$\hbar\omega \ll m_e v^2. \tag{2.12}$$

Then an asymptotic form of the hypergeometric function may be used to simplify Eq. (2.10):

$$F(i\eta_k, -i\eta_q, 1; \xi) \sim \frac{i}{\pi}\xi^{i(\eta_k+\eta_q)/2} e^{\pi(\eta_k+\eta_q)} \ln\left(\frac{2\sqrt{\eta}}{\eta_k+\eta_q}\right), \tag{2.13}$$

and Eq. (2.9) is simplified to

$$R(p, \omega \to q) \equiv R^{\mathrm{IB}} = \frac{2\pi e^6 E_0^2 Z^2 n_i}{\hbar\omega^3}\frac{1}{p^3}. \tag{2.14}$$

The electrons are of course not monochromatic but have a certain momentum spectrum. In the hot plasma case this will be described by a thermal Maxwell-Boltzmann distribution and the actual absorption rate that we are interested in is the distribution average of Eq. (2.14):

$$\begin{aligned}\langle R^{\mathrm{IB}}\rangle_{\mathrm{MB}} &= \frac{2\pi e^6 E_0^2 Z^2 n_i}{\hbar\omega^3}\frac{1}{(2\pi m_e k_B T)^{3/2}}\int \mathrm{d}^3 p \frac{1}{p^3} e^{-\frac{p^2}{2m_e k_B T}} \\ &= \frac{2\sqrt{2\pi}}{3}\frac{e^6 E_0^2 Z^2 n_i}{\hbar\omega^3 (m_e k_B T)^{3/2}} \ln\left(\frac{p_{\max}}{p_{\min}}\right) \\ &= \frac{2\sqrt{2\pi}}{3}\frac{e^6 E_0^2 Z^2 n_i}{\hbar\omega^3 (m_e k_B T)^{3/2}} \ln\Lambda.\end{aligned} \tag{2.15}$$

The ratio between the maximum and minimum momentum equals the ratio of largest and smallest impact parameters, which we take to be the Debye length $\lambda_D = \omega_p\sqrt{k_B T/m_e}$ and the Landau length $r_0 = Ze^2/k_B T$. We then find

$$\Lambda = \frac{(m_e k_B T)^{3/2}}{Ze^2 m_e^2 \omega_p}. \tag{2.16}$$

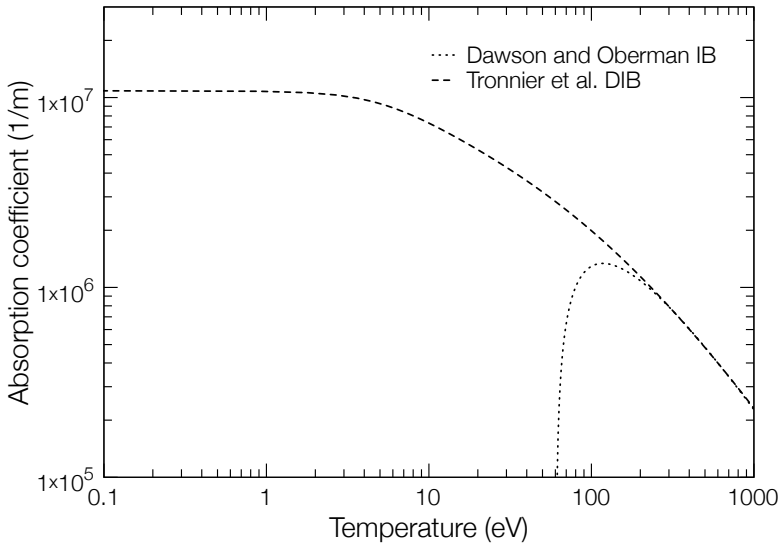

Figure 2.2: The absorption coefficient for the free-free opacity of Al according to the inverse bremsstrahlung theory of Dawson and Oberman [41], as given by Eq. (2.18). Due to the Coulomb logarithm, for temperatures below ∼70 eV the absorption becomes negative and this model is therefore not applicable to the degenerate regime. Also shown is the degenerate inverse Bremsstrahlung model proposed by Tronnier [42], which is briefly described in Section 2.3.2.

The collision frequency is related to the averaged absorption rate of inverse bremsstrahlung by the expression:

$$\nu^{\mathrm{IB}} = \frac{2m_e\hbar\omega^3}{e^2E_0^2}\langle R^{\mathrm{IB}}\rangle_{\mathrm{MB}}, \tag{2.17}$$

obtained assuming the validity of the Drude dielectric function given in Eq. (2.5). Taking the $\nu \ll \omega$ limit and considering Eq. (2.4), we obtain the IB absorption coefficient

$$\kappa = \frac{64\pi^3 Z n_e^2 e^6 \ln\Lambda}{3c\omega^2(2\pi m_e k_B T)^{3/2}}\left(1-\frac{\omega_p^2}{\omega^2}\right)^{-1/2}. \tag{2.18}$$

The temperature dependence of this model is important: note that the opacity decreases with increasing temperature as $T^{-3/2}$.

2.3.2 Extension to degenerate regimes

The approximations made to obtain the standard inverse bremsstrahlung absorption coefficient of Eq. (2.18) are clearly unsuitable at temperatures where the electron degeneracy starts to play a role:

$$\eta \leq 1, \qquad \hbar\omega \geq m_e v^2 \tag{2.19}$$

In particular, the expansion given in Eq. (2.13) is no longer valid and a different asymptotic form must be used. We use the expansion proposed by Krainov [43] to calculate the absorption rate in these conditions:

$$R^{\mathrm{DIB}} = \frac{2\pi^2}{15 \cdot 3^{5/6}} \frac{e^4 E_0^2 Z^2 n_i}{m_e^2 \hbar \omega^3} \left(\frac{2m_e e}{Z\omega}\right)^{2/3} \frac{1}{p} \frac{\Gamma(\frac{1}{3})}{\Gamma(\frac{2}{3})}. \tag{2.20}$$

The Maxwell-Boltzmann averaging is no longer applicable, being valid only for classical systems, and the averaging over initial electron momenta must be conducted with Fermi-Dirac statistics. Furthermore we must ensure that the final electron state is not occupied, for such transition would clearly be prohibited. The averaged rate is then given by:

$$\begin{aligned} \langle R^{\mathrm{DIB}} \rangle_{\mathrm{FD}} &= \frac{1}{30\pi \cdot 3^{5/6}} \frac{e^4 E_0^2 Z}{m_e^2 \hbar^4 \omega^3} \left(\frac{2m_e e}{Z\omega}\right)^{2/3} \frac{\Gamma(\frac{1}{3})}{\Gamma(\frac{2}{3})} \int \mathrm{d}^3 p \frac{1}{p} f_{\mathrm{FD}}(p)[1 - f_{\mathrm{FD}}(p+\omega)] \quad (2.21) \\ &= \frac{\pi^2}{5 \cdot 3^{5/6}} \frac{e^4 E_0^2 Z^2 n_i}{m_e^2 \hbar \omega^3} \left(\frac{2m_e e}{Z\omega}\right)^{2/3} \frac{\Gamma(\frac{1}{3})}{\Gamma(\frac{2}{3})} \frac{T}{p_F T_F (1 - e^{-\hbar\omega/k_B T})} \ln\left(\frac{1 + e^{\mu/k_B T}}{1 + e^{(\mu - \hbar\omega)/k_B T}}\right). \end{aligned}$$

Warm dense matter is a state between the two limits described here of fast and slow electrons. To model the absorption, a global model that handles intermediate temperature regimes is needed. An attempt to tackle this issue was made by Tronnier and collaborators [42], who calculated the momentum-averaged global absorption rate by interpolating between Eq. (2.15) and Eq. (2.21). They find

$$\begin{aligned} \langle R^{\mathrm{DIB}} \rangle_{\mathrm{FD}} =& \frac{3\sqrt{2}\pi}{4} \frac{e^6 E_0^2 Z n_e}{\hbar \omega^3 (m_e k_B T)^{3/2}} \left(\frac{T}{T_F}\right)^{3/2} \ln\left(1 + \frac{1.32}{\sqrt{2\pi}} \left[\frac{m_e k_B T}{(Z e^2 m_e^2 \omega)^{2/3}}\right]\right) \times \quad (2.22) \\ & (1 - e^{-\hbar\omega/k_B T})^{-1} \ln\left(\frac{1 + e^{\mu/k_B T}}{1 + e^{(\mu - \hbar\omega)/k_B T}}\right). \end{aligned}$$

which through the Drude model and Eq. (2.17) can be used to calculate the absorption coefficient, the form of which is however not particularly illuminating and can be found in the reference. The only reliable experimental data to test the models in the degenerate

electron regime is the absorption for room temperature, crystalline aluminium. In this comparison it will be seen that this result is reasonable and will be used for comparison with our results from the following section.

2.4 Absorption in quantum plasmas

In a seminal paper, Ron and Tzoar calculated in a systematic manner, using perturbation theory, the complex, frequency dependent conductivity for classical and quantum plasmas [44], using temperature-dependent Green's function theory and Kubo's formula for the conductivity (see Eq. (2.8)). Using a diagrammatical approach, Hopfield showed their result to be exact up to second order in the electron-ion interaction potential [45]. The macroscopic dielectric function is related to the complex conductivity $\sigma(\omega)$ by

$$\epsilon_M(\omega) = 1 + i\frac{\sigma(\omega)}{\omega}, \tag{2.23}$$

and the absorption coefficient can be found making use of Eq. (2.4).

The same functional form for the macroscopic dielectric function was also obtained by Sturm [46], albeit using a different approach, namely the density-density response function theory within the random phase approximation (RPA)(see Eq. (2.7)). Sturm considers the near-free electron (NFE) approximation, within which the interaction potential between electrons and ions is treated as a small perturbation to the homogeneous electron liquid. This corresponds to writing the dielectric function as a perturbation expansion, up to second order:

$$\begin{aligned}\epsilon_M(\omega) &= 1 + \varepsilon^{(1)}(\omega) + \varepsilon^{(2)}(\omega) \\ &= 1 - \frac{\omega_p^2}{\omega^2} + \varepsilon^{(2)}(\omega).\end{aligned} \tag{2.24}$$

The first two terms of Eq. (2.24) correspond to the free-electron liquid and the second order correction accounts for the electron-ion interaction according to the NFE approximation. It can be written in the form [45]:

$$\epsilon^{(2)}(\omega) = \frac{1}{6\pi^2}\frac{n_i}{m_e^2\omega^4}\int dq\; q^6 \frac{V_q^2}{|\varepsilon(q,\omega)|^2} S(q)\left[\varepsilon(q,\omega) - \varepsilon(q,0)\right]. \tag{2.25}$$

Here n_i is the ion density, V_q is the bare interaction potential, $\varepsilon(q,\omega)$ is the microscopic dielectric function of the homogeneous electron and $S(q)$ is the static ion-ion structure factor accounting for ion-ion correlations. While a fully quantum-mechanical and dy-

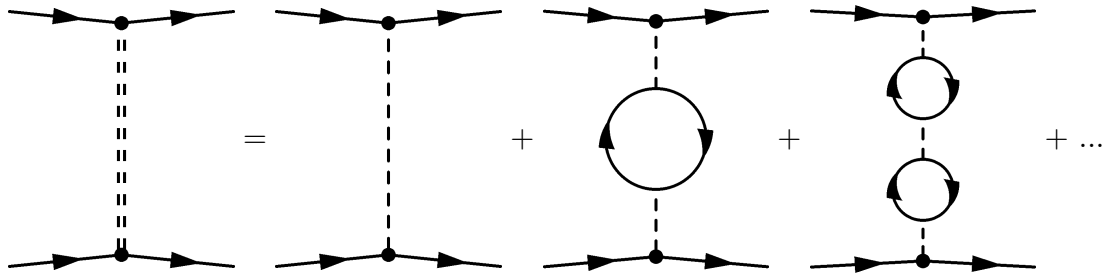

Figure 2.3: Screening in the random phase approximation: the screened interaction between two electrons in the homogeneous liquid is obtained by summing over the infinite series of bubble diagram interactions.

namical description is needed for the electrons, the ions may be treated statically, as they are much heavier and may be considered frozen-out during the relevant interaction time.

2.4.1 Electron dielectric function

Due to the large mass difference, the electrons are much more mobile than the ions and can be assumed to form a uniform neutralising background of negative charges (see for example [47]). This corresponds to saying that the valence electron wave-functions spatially overlap over several ionic sites. In this case, the electron subsystem may be treated as a homogeneous liquid with no reference to the discrete nature of the actual physical system. In the case of weekly interacting particles, the random-phase approximation (RPA) holds [48] and the dielectric function is given by:

$$\varepsilon_{\mathrm{RPA}}(q,\omega) = 1 + \nu(q)\Pi_{\mathrm{RPA}}(q,\omega), \tag{2.26}$$

where $\nu(q)$ is the Fourier transform of the Coulomb potential and $\Pi_{\mathrm{RPA}}(q,\omega)$ is the polarisation in the RPA:

$$\Pi_{\mathrm{RPA}}(q,\omega) = \pi^{+}(q,\omega) + \pi^{-}(q,\omega); \tag{2.27}$$

$$\pi^{+}(q,\omega) = -2\int \frac{d\mathbf{k}}{(2\pi)^3}\left[\frac{f(\mathbf{k})\{1-f(\mathbf{k}+\mathbf{q})\}}{\hbar\omega + i\delta + E(\mathbf{k}) - E(\mathbf{k}+\mathbf{q})}\right] \tag{2.28}$$

$$\pi^{-}(q,\omega) = -2\int \frac{d\mathbf{k}}{(2\pi)^3}\left[\frac{f(\mathbf{k})\{1-f(\mathbf{k}+\mathbf{q})\}}{-\hbar\omega - i\delta + E(\mathbf{k}) - E(\mathbf{k}+\mathbf{q})}\right], \tag{2.29}$$

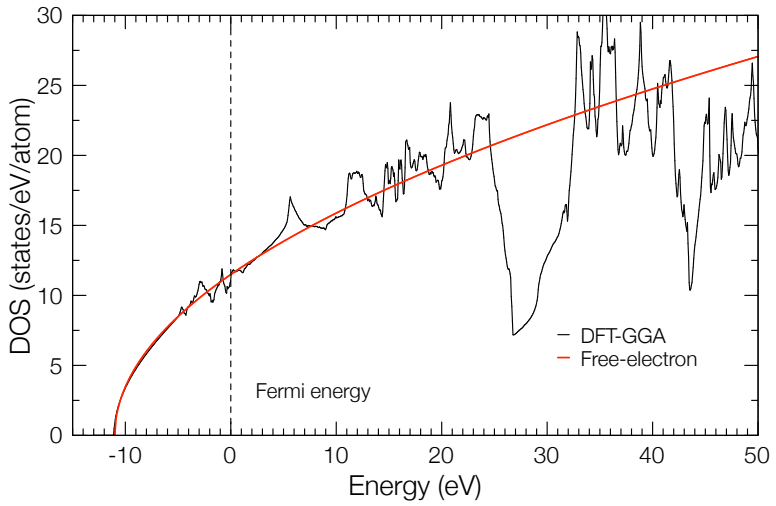

Figure 2.4: Density of valence states in Al.

with $f(\mathbf{q})$ denoting the Fermi-Dirac distribution of the electrons with wavevector q and kinetic energy $E_{\mathbf{q}} = \hbar^2 q^2/(2m_e)$. Causality is preserved by adding to the denominator the infinitesimal constant $\delta > 0$. From the diagrammatical point of view, the RPA corresponds to the infinite sum over all bubble diagram interactions, as shown in Fig. 2.3. Within this approximation, the electron dielectric function can be evaluated for all temperatures, densities and photon energies. The single dashed line in Fig. 2.3 represents the bare Coulomb interaction and the double dashed line the interaction screened by the dielectric function. The bubble diagram *per se* is the lowest order polarization process, involving the excitation and de-excitation of an electron-hole pair. The RPA is exact in the high density limit where long-range correlations dominate. At lower densities however, such as those in real metals, intermediate and short range correlations become increasingly important. Such correlations, described by vertex and self-energy corrections, need be considered if the problem is to be fully addressed.

The dielectric description of the valence band is a good approximation if it exhibits a behaviour similar to that of a homogeneous electron gas. We have calculated the density of states for Al using DFT and this result is illustrated in Fig. 2.4. We note that the free-electron assumption holds up to around 25 eV above the Fermi energy.

In considering semiconductors, Mahan pointed out that the optical absorption transition from the valence band to the conduction band leads to the creation of bound electron-hole states or excitons, which alter the absorption strength [49]. Further investigations have shown that such exciton states are also present in metals, and that

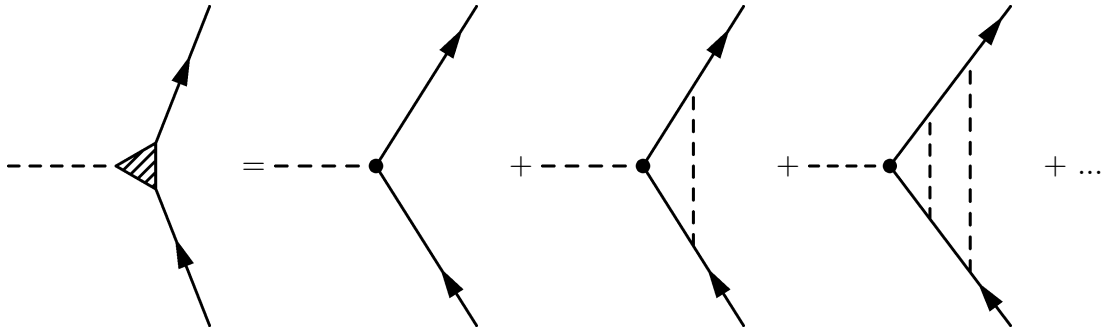

Figure 2.5: The vertex correction obtained by dressing the bare vertex with the infinite series of ladder diagrams.

they are at least in part responsible for the large discrepancies observed when comparing calculations to experimental absorption data [50]. Indeed, although band-structure calculations successfully predict energy thresholds in solids, the absorption strengths mismatch experimental data by as much as a factor two (a detailed review on the absorption in simple metals can be found in [37]). This leads us to believe that such effects could prove to be important also in WDM, which is similar to condensed matter in terms of inter-particle correlations.

Electron-hole interactions are not present in the RPA but can be added as a vertex correction in terms of the ladder diagrams shown in Fig. 2.5. This is the dominant contribution in describing excitons. In general, the RPA polarisation containing a dressed vertex can be written in the as:

$$\Pi_\Lambda(q,\omega) = -2\int \frac{d\mathbf{k}}{(2\pi)^3}\left[\frac{f(\mathbf{k})\{1-f(\mathbf{k}+\mathbf{q})\}-f(\mathbf{k}+\mathbf{q})\{1-f(\mathbf{k})\}}{\hbar\omega+i\delta+\tilde{E}(\mathbf{k})-\tilde{E}(\mathbf{k}+\mathbf{q})}\right]\Lambda(\mathbf{k};\mathbf{q},\omega). \quad (2.30)$$

The energy $\tilde{E}(\mathbf{k})$ contains the exchange self-energy correction:

$$\tilde{E}(\mathbf{k}) = E(\mathbf{k}) + \Sigma(\mathbf{k}), \quad (2.31)$$

$$\Sigma(\mathbf{k}) = -\int \frac{d\mathbf{k}'}{(2\pi)^3}\nu(\mathbf{k}-\mathbf{k}')f(\mathbf{k}'). \quad (2.32)$$

The term $\Lambda(\mathbf{k};\mathbf{q},\omega)$ is the vertex correction and is given by the integral equation:

$$\Lambda(\mathbf{k};\mathbf{q},\omega) = 1 + \int \frac{d\mathbf{k_1}}{(2\pi)^3}\nu(\mathbf{k}-\mathbf{k_1}) \times \left[\frac{f(\mathbf{k_1})\{1-f(\mathbf{k_1}+\mathbf{q})\}}{\hbar\omega + i\delta + \tilde{E}(\mathbf{k_1}) - \tilde{E}(\mathbf{k_1}+\mathbf{q})} - \frac{f(\mathbf{k_1}+\mathbf{q})\{1-f(\mathbf{k_1})\}}{\hbar\omega - i\delta + \tilde{E}(\mathbf{k_1}) - \tilde{E}(\mathbf{k_1}+\mathbf{q})}\right]\Lambda(\mathbf{k_1};\mathbf{q},\omega). \tag{2.33}$$

An approximate solution to Eqs. (2.30) and (2.33) was initially derived by Kleinman [51]. To lowest order in the vertex correction, the RPA result is recovered from Eq. (2.30). Considering the Coulomb interaction $\nu(\mathbf{k})$ as an average over momenta within the Fermi sphere, it is possible to decouple higher order terms and find a closed solution for Eq. (2.30) in terms of the RPA polarisations of Eqs. (2.28) and (2.29), as shown by Higuchi and Yasuhara [52]:

$$\Pi_\Lambda(q,\omega) = \frac{[\pi^+(q,\omega)+\pi^-(q,\omega)] - (\nu_1-\nu_2)\pi^+(q,\omega)\pi^-(q,\omega)}{1-\frac{\nu_1}{2}[\pi^+(q,\omega)+\pi^-(q,\omega)] + \frac{1}{4}(\nu_1+\nu_2)(\nu_1-\nu_2)\pi^+(q,\omega)\pi^-(q,\omega)}, \tag{2.34}$$

with

$$\nu_1 = \langle\nu(\mathbf{k_1}-\mathbf{k_2})\rangle \quad \text{and} \quad \nu_2 = \langle\nu(\mathbf{k_1}+\mathbf{q}-\mathbf{k_2})\rangle. \tag{2.35}$$

The average in Eq. (2.35) is that over the Fermi sphere and is given by the integral:

$$\langle q^\alpha\rangle = \int_0^\infty \frac{q^\alpha\rho(E)dE}{1+e^{\beta E-\eta}}. \tag{2.36}$$

with $\rho(E)$ the density of states (DOS), $\alpha = -2$ for the Coulomb potential and $\eta = \mu/(k_BT)$ the term containing the chemical potential μ. The new, local field corrected dielectric function is then given by

$$\varepsilon_{\mathrm{LFC}}(q,\omega) = 1 + \nu(q)\Pi_\Lambda(q,\omega). \tag{2.37}$$

An extension to finite temperatures of this result is fairly straightforward since only RPA polarizations and Coulomb averages appear in Eq. (2.34), which can be easily evaluated for the entire temperature range of interest. A comparison between the RPA and the LFC dielectric function is shown in Fig. 2.6 and the representative diagrams are illustrated in Fig. 2.7.

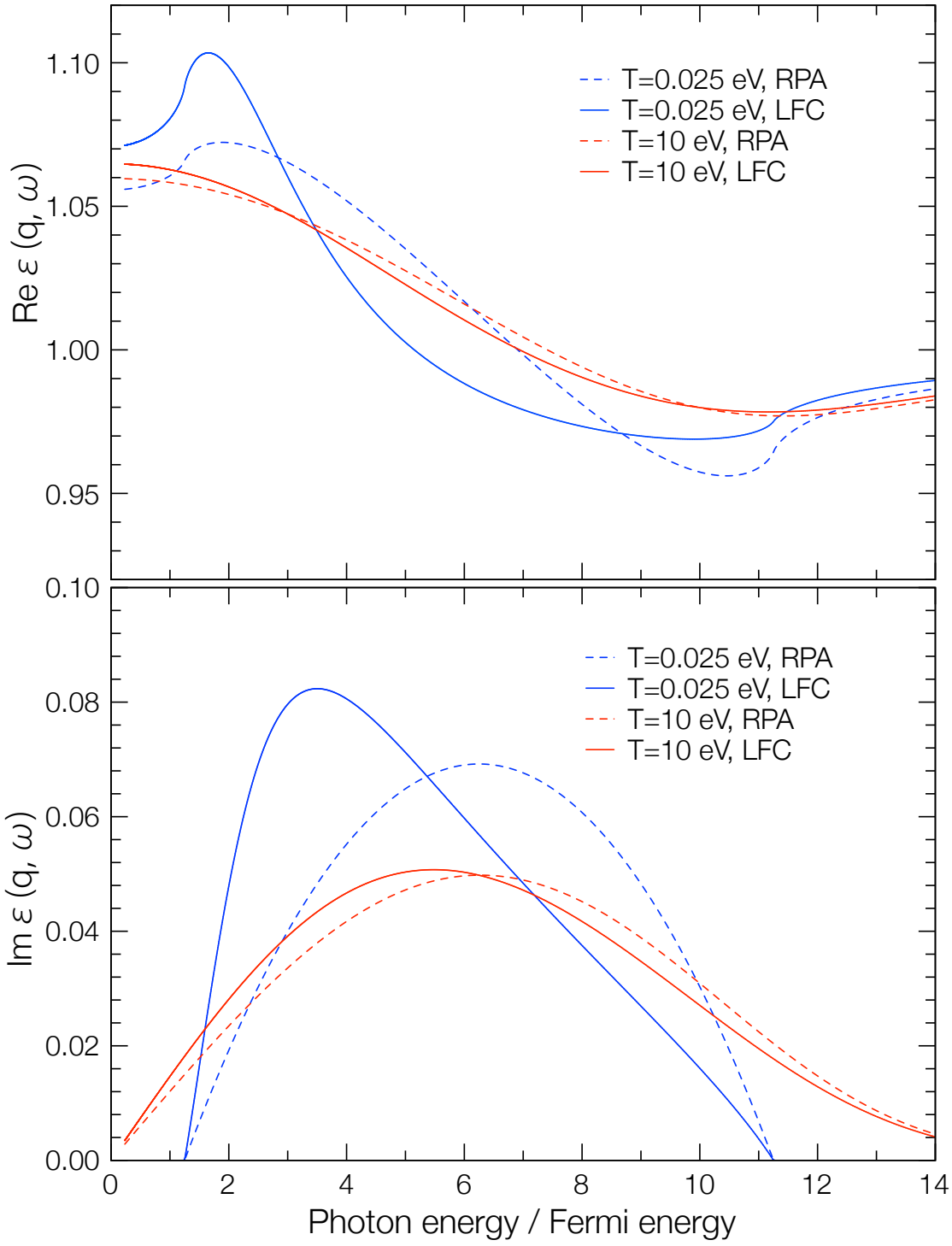

Figure 2.6: Comparison between the real and imaginary parts of the RPA dielectric function with and without electron-hole coupling (LFC). The largest difference between the two can be seen for large q-vectors, here shown at $q = 2q_F$. As the temperature increases, the LFC becomes less pronounced becoming negligible for temperatures above the Fermi temperature ($\sim$11 eV).

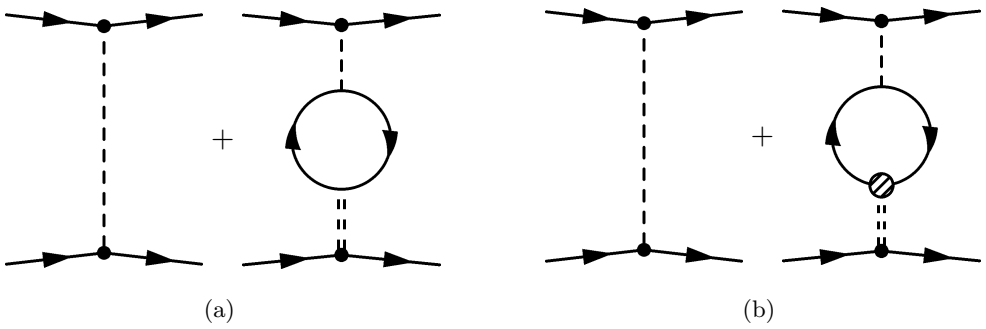

Figure 2.7: Diagrammatical representation of the screening in the RPA (a) and with the LFC (b).

2.4.2 Ion-ion structure factor

There are different approaches that we can use to calculate the ion-ion structure factor in WDM. Numerically, molecular dynamics (MD) [53] techniques as well as direct solution of the hyper-netted chain (HNC) equations [54, 53] can be implemented for finite-temperature dense plasmas. While accurate for ideal classical plasmas, both MD and HNC become computationally very expensive if the full dynamic response of the quantum electron background has to be accounted for. In order to simplify the analysis, we use the approach initially suggested by Singh and Holz [55] for a liquid metal and applied to the ion-ion structure factor of WDM by Gregori *et al.* [56]. In this simplified approach, the bare ionic response is constructed from the analytical solution of the mean spherical equations for a system of charged hard spheres embedded in a neutralising background [57]. Such an approximation is the equivalent of the Percus-Yevick solution for a neutral gas of hard spheres [58, 53], and it has been shown to correctly reproduce MD and HNC results at various degrees of inter-ion coupling [53]. The idealised one-component plasma (OCP) structure factor $S_{\rm OCP}(q)$ is thus obtained. The dynamical screening of the electron background on the ions is then calculated within the linear response framework [59, 56],

$$S(q) = S_{\rm WDM}(q) = \frac{S_{\rm OCP}(q)}{1 + f_v(q) S_{\rm OCP}(q)}, \tag{2.38}$$

where $f_v(q)$ is the attractive screening correction to the bare ion-ion interaction [55, 56]:

$$f_v(q) = \frac{Z K_D^2}{q^2} \cos^2[q r_{hc}(T)] \left(\frac{1}{\varepsilon(q)} - 1 \right), \tag{2.39}$$

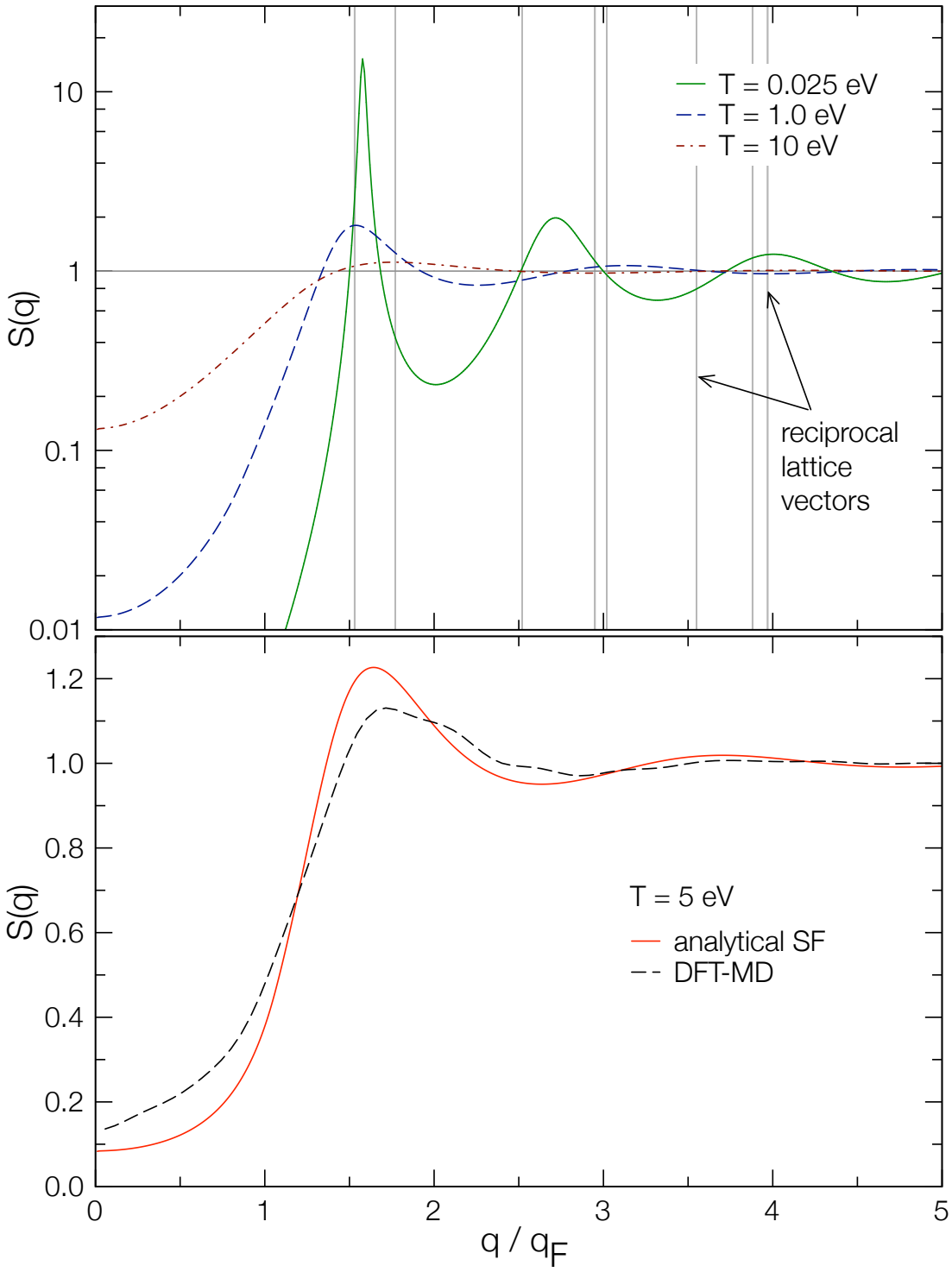

Figure 2.8: Ion-ion structure factor given by Eq. (2.38) for warm dense Al. Above, the analytical calculation is shown for three different temperatures and compared with the two limiting results: a hot, dilute plasma where $S(q) \to 1$, and cold, crystalline Al where only reciprocal lattice vectors contribute according to Eq. (2.46). Below we compare the analytical $S(q)$ to that obtained through our DFT-MD calculations for a system in thermal equilibrium at 5 eV.

with $\varepsilon(q)$ the frequency integrated electron dielectric function, $K_D^2 = Zn_e e^2/(\epsilon_0 k_B T)$ is the square Debye wavevector and $r_{hc}(T)$ the temperature dependent effective hard-sphere radius, determined by imposing that the ion pair correlation function must be continuous at the hard sphere boundary [56]. A final point to consider is that in our analysis the dense plasma is in thermodynamic equilibrium at the same temperature for both electron and ion subsystems. Such an assumption cannot always be made. For example, right after heating with a femtosecond FEL pulse, only the electrons will be heated and it will take several picoseconds for the electron-phonon coupling to equilibrate the electrons with the lattice. Therefore, if the opacity is required on timescales shorter than that of electron-phonon coupling, the theory discussed here must be extended to a two-temperature plasma, as shown in Ref. [56].

2.4.3 Electron-ion interaction potential

The equation for the absorption coefficient given in Eq. (2.25) requires a term to account for the electron-ion interaction. This term is in principle very challenging to estimate as it not only accounts for the interaction of an electron with the nucleus but also with all other electrons in the core states. These do not contribute to the absorption in terms of direct excitation, being too tightly bound, however, they dynamically screen the core, altering significantly the potential seen by the valence electrons.

There are several practical, albeit approximate, ways to calculate this potential to very high accuracy. A particular one, the projector augmented wave method, will be discussed later on in Chapter 5. For the discussion here a simple analytical model will suffice, which although crude, exhibits the basic features necessary to account for the underlining physics. In particular, for an atom with Z valence electrons, at long distances the valence electrons should see the Coulomb potential of a pseudo-ion of charge Ze and the pseudopotential in this limit should therefore have the asymptotic form $\propto -Ze^2/r$. At short distances, the presence of core electrons creates a repulsive potential around the ion and the pseudopotential should approach some constant.

Several different potentials for the valence electrons in Al, statically screened by the RPA dielectric function $\varepsilon(\omega = 0, k)$, are shown in reciprocal space in Fig. 2.9. As can be seen from this figure, we can divide the potentials in two fundamental groups: potentials to represent the Coulomb attraction for isolated atoms and those for solids. The exact solution for an isolated atom with one electron is of course simply the Coulomb potential. The RWI potentials [60] are analytical, effective potentials for atomic Al and are very similar to the full Coulomb potential at all but shortest wavelengths. In a solid, the

crystalline potential that the electron feels is much weaker than the strong potential of an isolated atom and a simple model applicable to this case is the empty-core potential of Horsfield and Ashcroft [61], defined as:

$$V(r) = \begin{cases} 0 & \text{for} \quad r < r_c \\ -Ze^2/(4\pi\varepsilon_0 r) & \text{for} \quad r > r_c \end{cases} \tag{2.40}$$

The Fourier transform of $V(r)$ is given by

$$V_q = -\frac{Ze^2}{\varepsilon_0 q^2}\cos(qr_c). \tag{2.41}$$

The distance at which this core electron screening becomes important is denoted here as the core radius r_c which is generally a free parameter to be determined by the fit to available experimental data. We take $r_c = 0.608$ Å, a value which minimizes the difference between the pseudopotential values and experimental data obtained through de Haas–van Alphen measurements of the Fermi surface, at the reciprocal lattice points (111) and (200) [61]. As r_c represents the core electron contribution it is not effected by dense plasma effects and can be considered constant in the temperature range of interest [62]. The temperature dependence of the pseudopotential is therefore given only by the valence electrons through the dielectric screening.

The cosine function in the Fourier transform of the empty-core potential is not a physical feature but rather an artefact due to the discontinuity of the potential in real space for $r = r_c$. A model similar to it, but imposing the more physical condition of real-space continuity was introduced by Krasko and Gurskii [63]:

$$V_{\mathrm{KG}}(r) = Z\left(\frac{\mathrm{e}^{-r/r_c} - 1}{r} + \frac{a}{r_c}\mathrm{e}^{-r/r_c}\right), \tag{2.42}$$

with $a = 2.67$ and $r_c = 0.36$ two fitting parameters to the (111) and (200) reciprocal lattice vectors. The Fourier transform is shown in Fig. 2.9, compared to the empty core model.

2.4.4 Classical and quantum limits

We have given a description of the electron and ion structure factors and of the interaction potential that are to be considered for WDM. The model is, however, also consistent with known results from the two limiting cases: a hot, classical plasma and a cold, crystalline solid, provided appropriate considerations are made.

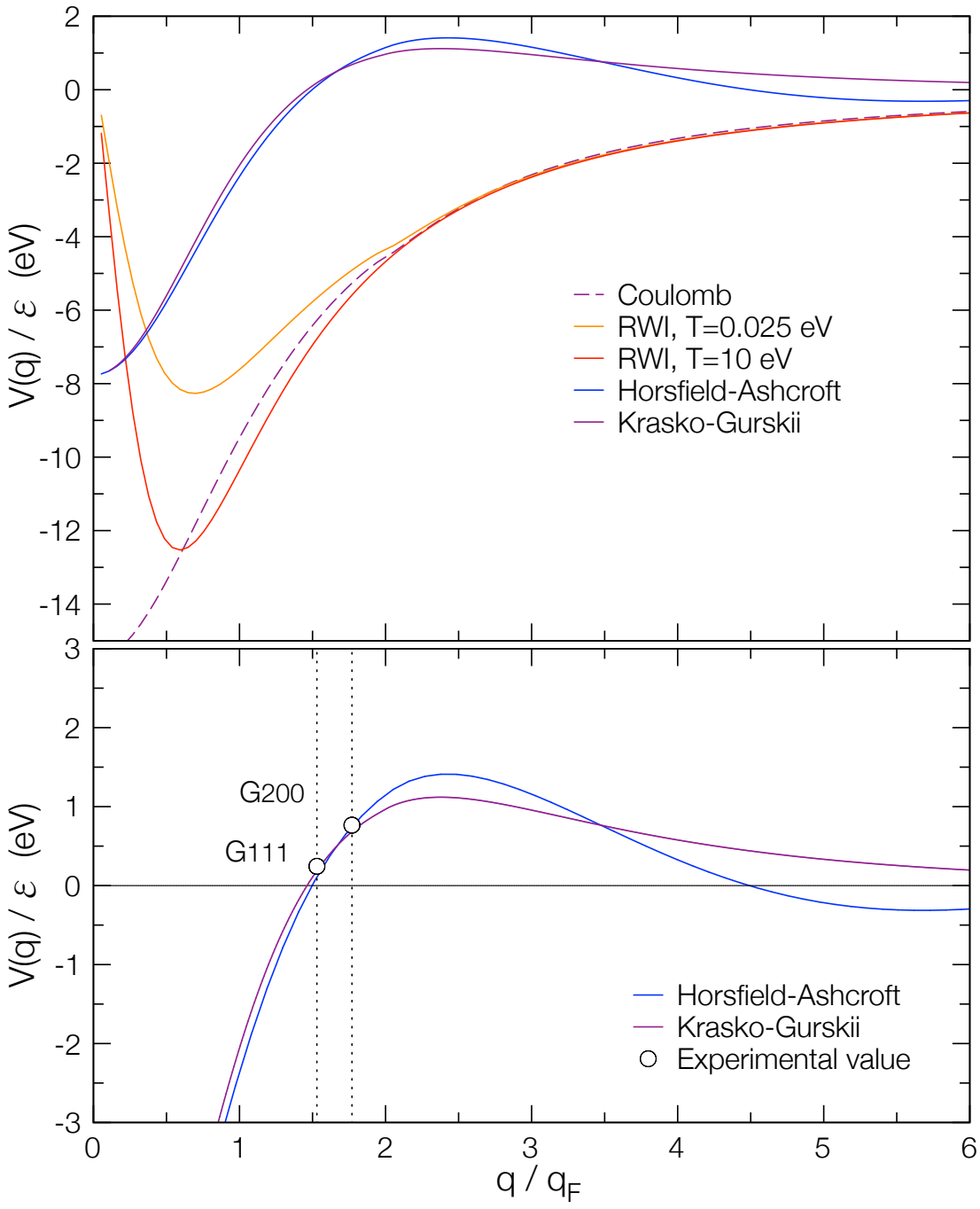

Figure 2.9: Screened pseudopotentials in reciprocal space for the 3 valence electrons in Al, compared with the Coulomb potential. RWI potential is for atomic Al, while the H-A and K-G models represent the effective potential in solid, crystalline Al. The potential at the first two reciprocal vectors, G_{111} and G_{200}, can be extracted from de Haas–van Alphen measurements of the Fermi surface and are used as a fitting parameter (see text).

Hot plasma

In this limit, we may take the classical dielectric function for the electron subsystem

$$\varepsilon_{\text{class}}(q,\omega) = 1 + \frac{e^2}{\varepsilon_0 q^2}\int d\mathbf{v}\frac{\mathbf{q}\cdot\mathbf{v}}{\omega - \mathbf{q}\cdot\mathbf{v} + i\delta}\frac{\partial f_{\text{MB}}(\mathbf{v})}{\partial E}, \tag{2.43}$$

with $f_{\text{MB}}(\mathbf{v})$ the Maxwell-Boltzmann velocity distribution and $E = m_e v^2/2$ the kinetic energy. The ionic and electronic structure factors will be then given by the Debye-Hückel theory and Eq. (2.25) assumes the form

$$\epsilon^{(2)}(\omega) = \frac{1}{6\pi^2}\frac{n_i}{m_e^2\omega^4}\int dq q^2 V_q^2 \frac{q^2 + K_D^2}{q^2 + (1+Z)K_D^2}\left(\frac{q^2}{q^2+K_D^2} - \frac{1}{\varepsilon_{\text{class}}(q,\omega)}\right). \tag{2.44}$$

In a dilute, hot system, the potential V_q is well described by the Coulomb potential. Inserting this in the equation above allows us to recover (after some tedious manipulation) the result for classical plasmas of Eq. (2.18) [44]:

$$\kappa = \frac{64\pi^3 Z n_e^2 e^6 \ln\Lambda}{3c\omega^2(2\pi m_e k_B T)^{3/2}}\left(1 - \frac{\omega_p^2}{\omega^2}\right)^{-1/2}. \tag{2.45}$$

Crystalline solid

The ion-ion structure factor for a crystalline solid is obtained by considering that in this case, the ions form a lattice in both real and reciprocal space. For simplicity we will assume a perfect lattice and will not consider the ionic thermal spectrum. This assumption does not alter noticeably the final results since the change in the structure factor due to the Debye-Waller factor at 300 K is negligible for the final absorption. The ion-ion structure factor for this idealized lattice is then given by

$$S_{\text{solid}}(q) = 2\pi^2 n_i \sum_{\mathbf{G}} \delta(\mathbf{q} - \mathbf{G}) = 2\pi^2 n_i \sum_G g_G \delta(q - G), \tag{2.46}$$

where $\mathbf{G}$ indicates the reciprocal lattice vectors, $G = |\mathbf{G}|$ and g_G counts the number of reciprocal lattice vectors of length G (star of G). With this structure factor, the second order contribution to the macroscopic dielectric function given by Eq. (2.25) becomes

$$\epsilon^{(2)}(\omega) = \frac{n_i^2}{3\omega^4 m_e^2}\sum_G g_G G^4 V_G^2\left(\frac{1}{\varepsilon(G,0)} - \frac{1}{\varepsilon(G,\omega)}\right). \tag{2.47}$$

Sturm and collaborators showed that Eq. (2.47) corresponds to the inter-band optical absorption in a solid [46]. Their results are then seen to agree with the plasma calculations of Ron and Tzoar [44], apart from a small modification accounting for the inter-band oscillator strength enhancement (in the case of crystalline aluminium an increase of 16% [37]). At frequencies between the plasma frequency and the L-shell threshold, this is the only significant term contributing to the total absorption since the Drude-like intra-band term, which dominates at low frequencies, is negligible.

The potential at the lowest reciprocal sites can be obtained from measurements of the Fermi surface, and we can use these results directly for V_G in Eq. (2.47). For aluminium we have $U_{111} = 0.244$ eV and $U_{200} = 0.765$ eV [61], where U_G is the normalised, screened empty-core potential given by

$$U_G = n_i \frac{V_G}{\varepsilon(G, \omega)}. \tag{2.48}$$

In order to obtain the potential at higher G values, we use the empty-core pseudopotential discussed in Section 2.4.3.

2.5 Absorption coefficient from first principles

In addition to modelling the absorption as described above, first principle calculations of the absorption in the crystalline and warm-dense state of Al were conducted using finite-temperature density functional theory (FT-DFT) [64] combined with snapshots of equilibrated molecular dynamics simulations (MD). These calculations were obtained using the VASP DFT code for the electronic structure, along with a Kubo-Greenwood (KG) calculation of the optical properties, and were conducted by Dr. Michael P. Desjarlais from the Sandia laboratories, USA. As such, the DFT techniques for the absorption calculation will not be discussed in great detail. Nevertheless, the results are very important as a benchmark for other calculations so the basic parameters used to obtain them are provided as a reference.

The absorption may be calculated from first principles making use of the Kubo-Greenwood formalism for the conductivity, as illustrated in Eq. (2.8). To this end, the electron wave functions and eigenvalues are needed, and these are obtained self-consistently at a given electron temperature and a set of ionic positions by means of a FT-DFT calculation. The temperature and trajectory of the ions are calculated by performing classical molecular dynamics calculations, evolving the inter-ionic forces while calculating the full DFT ground state charge density at each step. This kind of calculation is clearly of particular importance for absorption in equilibrated WDM and will

be referred to as DFT-MD. Although each Al atom contains 13 electrons, not all are in principle important for the opacity in the XUV. In the simplest approximation, only the 3 outer electrons need be considered for the free-free opacity, while the remaining 10 can be assumed to only contribute to screening the ionic core. In the DFT calculation this separation is implemented using pseudopotentials[4] for the ions, with the first 10 electrons frozen in the core, creating a pseudo-ion of charge +3. The remaining 3 electrons are fully considered and provide the structure of the Al valence band. It was later observed that a more accurate representation of the system necessitates the inclusion of additional electrons to the valence band so that the DFT calculations may account for core-electron polarization effects. For this reason, as well as also to estimate the quality of the potentials in use, two sets of calculations have been performed using either 3 or 11 valence electrons for each Al atom. The results using these two potentials will be referred to as *VASP Desjarlais* 1 or 2, respectively, in the figures.

The electronic structure calculation with the potential containing only 3 valence electrons is conducted using 32 Al atoms placed inside a triply periodic cubic box corresponding to a density of 2.7 gcm^{-3} (corresponding to solid, room temperature Al). The DFT-MD absorption calculations have been done up to a photon energy of 45 eV. The absorption at higher energies are not included due to an increase in spurious features connected to the influence of the pseudopotential on the DOS as the L-edge is approached.

For the calculations with 11 electrons per atom, and for cold metallic Al, an 8 atom cubic box was used, and in addition to the standard DFT calculation several corrections are taken into account such as core electron polarization, local field corrections[5] and screening in the GW approximation. The need for such a complete treatment arose from the observation that standard DFT-MD accounts poorly for the experimentally measured absorption in metallic Al, as is clearly visible in Fig. 2.11. Such a calculation has not been done yet for the WDM case due to the excessive computational cost, however, a non-GW calculation using the same 11-electron improved pseudopotential has been done and shows a marked improvement over previous calculations. These WDM results, as a function of temperature, are displayed in Fig. 2.12.

From the MD results we can extract the ion-ion structure factor and compare it to the analytical expression given in Eq. (2.38). This comparison is shown in Fig. 2.8, where a good agreement between the two can be seen.

[4]Projector Augmented Wave (PAW) potentials are used, which will be covered in detail in Section 5.4.
[5]Note that this LFC is somewhat different to that used for the analytical model.

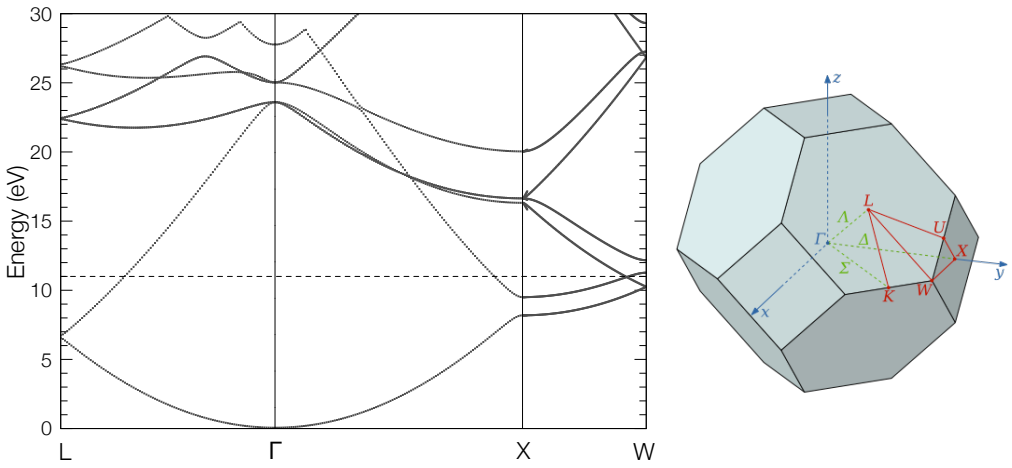

Figure 2.10: Band structure for room temperature, crystalline Al, computed for 8 bands and 200 k-points.The region of interest for the evaluation of the potential is around the W point, which corresponds to the corner of the first Brillouin zone. The bottom of the band is set to 0 and the dashed line indicates the Fermi energy at 11 eV. Points of high symmetry used in the band structure calculation are also shown on the Brillouin zone. Brillouin zone image taken from Wikipedia.

2.5.1 Electron-ion potential in DFT

As discussed in section 2.4.3, the effective electron-ion interaction potential is the most difficult ingredient to model in the calculation of the absorption. It is therefore of considerable interest to compare the potential used in the analytical model of section 2.4 to that used in DFT-MD. The DFT calculation uses atomic, PAW pseudopotentials with frozen core orbitals. As such, these potentials can be very accurate in describing the physical picture and at the same time also computationally efficient. These atomic potentials are used to construct the crystal potential that is then used in the self-consistent DFT ground-state calculation. The analytical model on the other hand uses a much simpler, one-dimensional empirical empty-core pseudopotential to represent the effective crystalline potential of the real problem. In the cold-solid it is needed, in principle, for all reciprocal lattice vectors while for the WDM regime it is needed for all k space (the one-dimensionality comes from the assumption of spherical symmetry, which is a reasonable approximation for cubic systems). Given the non-local nature of the crystalline potential used in the DFT computation, a direct comparison with the more manageable empty-core is not possible. Nevertheless, local information on the crystalline potential can be retrieved by calculating the band structure at specific points of high symmetry.

As illustrated in [61], the first four energy bands at the W-point are related to the

V_{111} and V_{200} Fourier components of the effective electron-ion potential by the relations:

$$\begin{aligned} E(W,1) &= E(W,2) = \epsilon_W - V_{200} \\ E(W,3) &= \epsilon_W + V_{200} - 2V_{111} \\ E(W,4) &= \epsilon_W + V_{200} + 2V_{111}, \end{aligned} \tag{2.49}$$

where $\epsilon_W = \hbar^2 k_W^2/2m$ is the free-electron energy at the W-point. Here we have set $V_{000} = 0$, which corresponds to setting the bottom of the valence band to 0, as was done to create Fig. 2.10. Inverting Eqs. (2.49) we find

$$\begin{aligned} V_{111} &= \frac{1}{4}\{E(W,4) - E(W,3)\} \\ V_{200} &= \frac{1}{2}\{E(W,3) - E(W,1)\} + V_{111}. \end{aligned} \tag{2.50}$$

The first four energies in $k = W$ are calculated to be 10.15 eV (doubly degenerate), 11.17 eV and 12.07 eV, yielding the following values for the potentials:

$$\begin{aligned} V_{111}^{\mathrm{DFT}} &= (0.23 \pm 0.01)\,\mathrm{eV} \\ V_{200}^{\mathrm{DFT}} &= (0.74 \pm 0.01)\,\mathrm{eV}. \end{aligned} \tag{2.51}$$

The Fermi surface can be measured experimentally through the de Haas-van Alphen effect and the potentials can be found using an approach similar to the above, yielding [65]:

$$\begin{aligned} V_{111}^{\mathrm{exp}} &= (0.243 \pm 0.001)\,\mathrm{eV} \\ V_{200}^{\mathrm{exp}} &= (0.764 \pm 0.001)\,\mathrm{eV}. \end{aligned} \tag{2.52}$$

2.6 Results and discussion

The absorption coefficient for warm dense aluminium, calculated using Eqs. (2.25) and (2.38), and with the inclusion of particle-hole interactions according to Eq. (2.37), is plotted as a function of temperature in Fig. 2.12. The results are compared with those in the RPA, i.e. without LFC, and to the DFT-MD calculations. A good agreement is found in the region of validity of the NFE approximation in Al, i.e for photon energies up to the pseudo band-gap between $3d$ and $4f$ bands, around 35 eV above the bottom of the valence band (see Fig. 2.4). This is a known feature in the DOS of Al as shown in Fig. 2.4, which is well approximated by the free-electron DOS only at lower

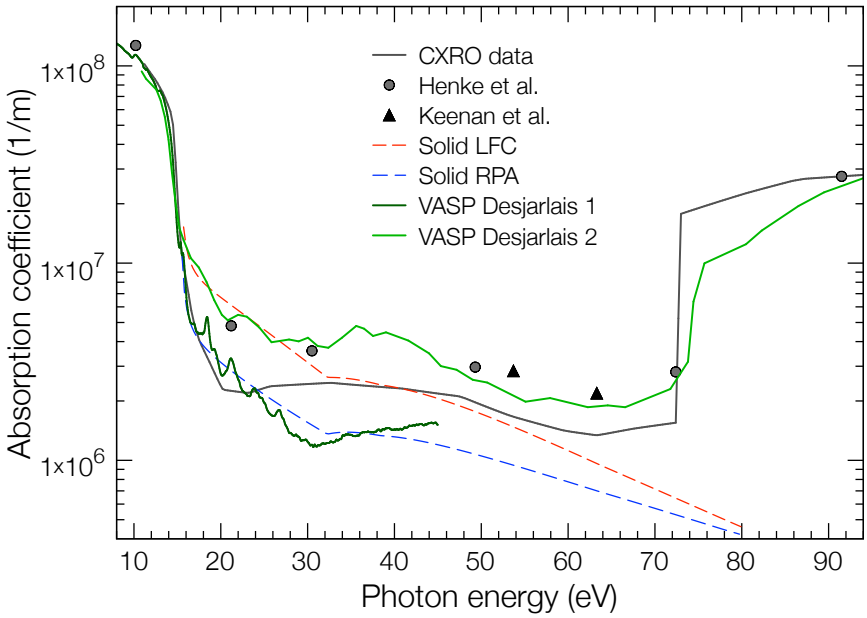

Figure 2.11: Absorption coefficient for crystalline Al at room temperature. The analytical and DFT-MD calculations are compared with experimental data [67, 34, 36].

energies (also see for example, Ref. [66]). We note that in the region of validity of the NFE approximation, the absorption coefficient exhibits a peak in the absorption at a temperature of around 10 eV. This is seen both in the RPA and LFC calculations and in the DFT-MD.

Experimental data for warm dense Al is scarce, with the existing results presenting too large experimental errors to enable a comparison with the calculations presented here [68]. The most reliable experimental results to date are those for room temperature, crystalline Al, which although different to WDM, exhibit similar strong correlation effects and are as such a good test for our calculations. The accurate values of the XUV absorption in cold Al are also of great practical interest due to the widespread use of Al as a filter in XUV laser and high harmonic generation experiments. It is therefore surprising that two different tabulated datasets are currently used in this regime: those of Henke *et al.* [34] and of Gullikson *et al.* [35], which are used for the CXRO database in this regime [67]. These results differ by up to a factor two in the region of interest, as can be seen in Fig. 2.11. We note that more recent measurements using XUV lasers conducted at photon energies of 53.7 eV and 63.3 eV [36] seem to show better agreement with the Henke data. As in the WDM case, in the solid case the DFT-MD results

(VASP Desjarlais 1) agree reasonably well with the analytical calculation in the RPA. The addition of the LFC shows an enhancement to the absorption of about a factor two, placing this calculation in rough agreement with the experimental data. It is interesting to note that considering the agreement between the analytic RPA and DFT-MD calculations, such a large change in the opacity due to exciton contributions may provide some indication of the limitations of using basic DFT-MD in free-free opacity calculations in this regime. It is nevertheless important to note that the DFT-MD results seem to underestimate the free-free absorption systematically throughout most of the range for which calculations are available. Very recent DFT-MD calculations including core-electron polarization, GW screening and local field corrections (VASP Desjarlais 2) show a marked improvement in the calculated absorption coefficient compared with the experimental values of Henke et al. This provides the first accurate ab initio absorption calculation in this regime and the techniques used and implications to WDM opacities will be discussed in a future publication.

A very important prediction of the study presented here is the observation of a peak in the absorption as a function of temperature, predominant at lower frequencies. To understand the physical significance of this peak we refer to Fig. 2.13, where we plot the temperature dependence of the absorption coefficient for three different types of physical systems: a solid and WDM, heated on a femtosecond time scale so that the electrons are hot but the ions are still cold, and WDM in thermal equilibrium. As the peak is due to the overlapping contributions of the electron and ion system, it is strongest in the thermalised WDM case. The ion contribution is due to the thermal broadening of the peaks in the ion-ion structure factor (see Fig. 2.8), which enables a larger range of k-vectors to satisfy the dispersion relation and contribute to the absorption. Experimentally this corresponds to performing an absorption measurement on picosecond time-scales after the initial heating, so as to allow for electron-ion thermalisation. On the other hand, when solid Al is rapidly heated (e.g. by a short FEL pulse) the energy is initially only transferred to the electrons while the ions remain cold. Therefore, during the first $\sim$100 fs after the short heating pulse, the opacity is described by the curve in Fig. 2.13 describing the solid with ions at room temperature. In the same figure we also present the WDM absorption in the cold-ion limiting case which shows good agreement with that of a crystal, within 10%. We note that also on such short time-scales a peak in the absorption is expected due solely to the electron system. This is caused by the plasmon thermal broadening and reduced electron screening at higher temperatures. It is worth noting that although the work here presented is for Al, similar results are expected for other simple metals with near free electrons. Note that the standard temperature dependence of the absorption

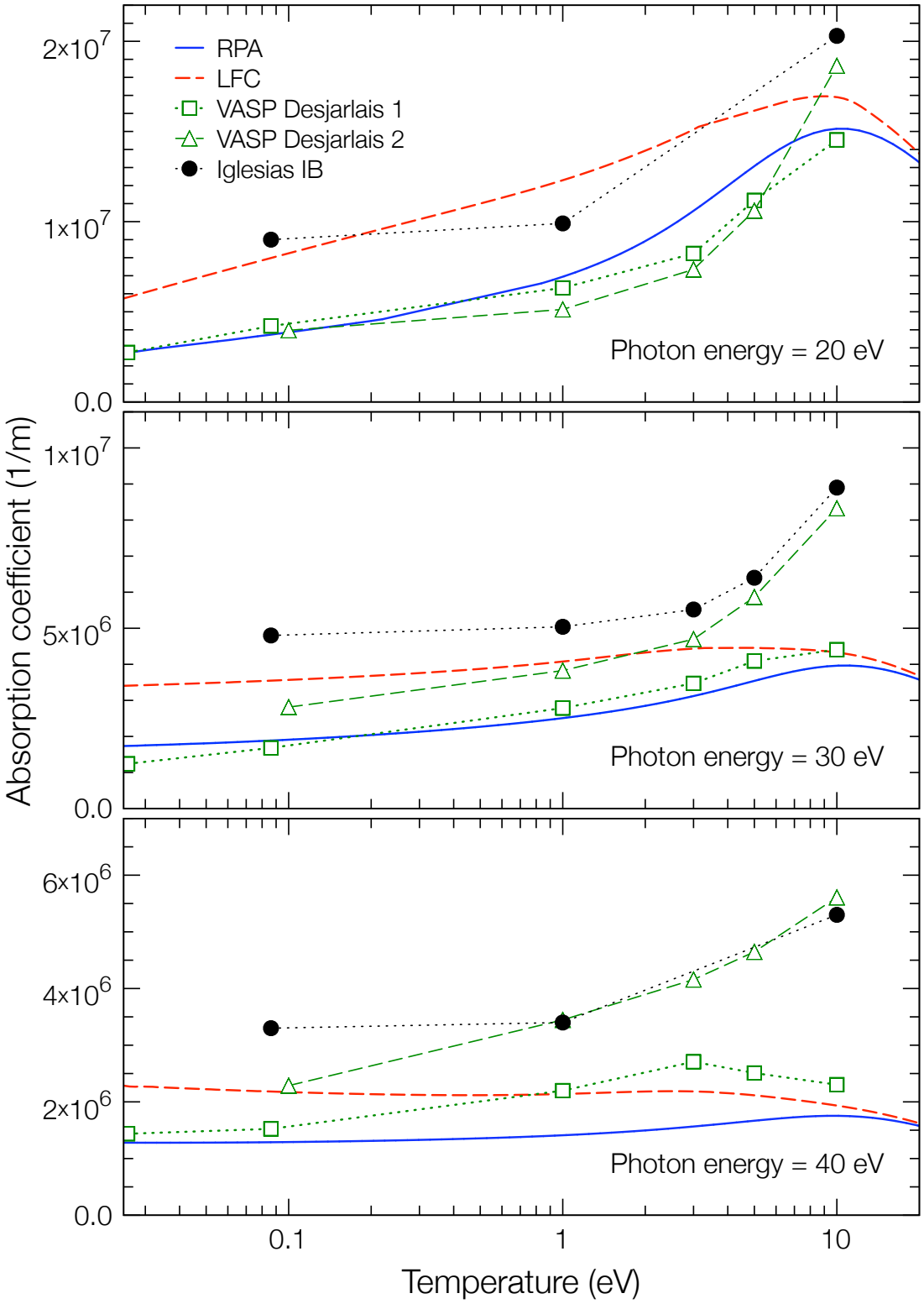

Figure 2.12: Absorption coefficient of warm dense Al at solid density and constant ionization $Z = 3$. The comparison is made between DFT-MD calculations and analytical results using S_{WDM} in the RPA and with LFC, and the recent plasma calculations of Iglesias [39]. Electron-ion thermal equilibrium is assumed throughout.

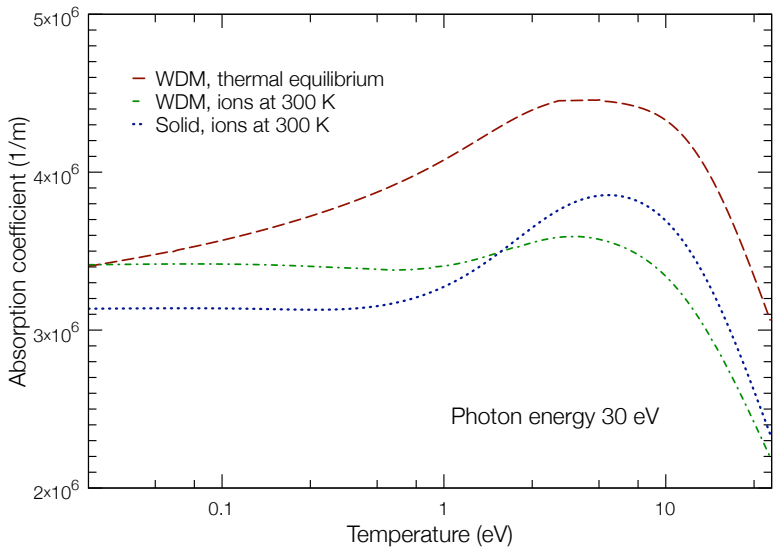

Figure 2.13: Absorption coefficient versus temperature for warm dense Al in thermal equilibrium (red), warm dense Al with ions at room temperature (green) and solid Al with ions at room temperature (blue). Solid density and constant ionization $Z = 3$.

in plasma physics, as given by Eq. (2.18), is a decreasing $\propto T^{-3/2}$. This result is in stark contrast to our results up to a temperature of 10 – 20 eV. At higher temperatures however the standard result is recovered, bringing the two in agreement.

This radically different trend of the absorption coefficient at intermediate and low temperatures was the main drive behind the publication of the results presented in this chapter (see reference [27]), as it is in contrast to several other prevailing predictions, namely the slow-electron extension of IB to the degenerate regime [43, 42], and plasma opacity codes [38]. However, it is important to point out that the standard IB absorption coefficient [69] is not directly applicable to this temperature region due to well-known issues of the Coulomb logarithm becoming negative (see Eq. (2.18) and Fig. 2.2). Several tentative attempts have been made to solve this issue in the warm dense regime, for example by adding 1 to the argument of the Coulomb logarithm, which prevents it from going negative [70]. We note that although *ad hoc*, this solution does roughly provide a similar trend in the absorption as we observe. Interestingly, recently published computational results based on inverse bremsstrahlung also support a peaked temperature dependence of the absorption coefficient [39]. However, experimental evidence for this behaviour has yet to emerge.

Although the trend of the absorption coefficient in our calculations resembles that experimentally measured, the absolute values that we calculate seem to underestimate systematically the experimental results in the cold, solid system. We have shown that this discrepancy can be in part explained by considering additional local field contributions to the absorption beyond the RPA formalism, which are seen to be of particular importance in the cold system. A more detailed evaluation of the experiment–theory comparison is unfortunately hindered by the significant uncertainty in the experimental values for the absorption coefficient in this regime. All caveats taken in consideration, what does emerge from the research presented is that accounting for local fields is an essential step in accurately modelling the free-free absorption process. The first successful step in this direction are the most recent DFT-MD calculations by Desjarlais shown for a cold Al sample in Fig. 2.11, which illustrate an excellent agreement with cold solid measurements and pave the way for accurate evaluations of the free-free opacity in warm dense matter.

CHAPTER 3

Free-electron Lasers and the Generation of High-intensity XUV Radiation

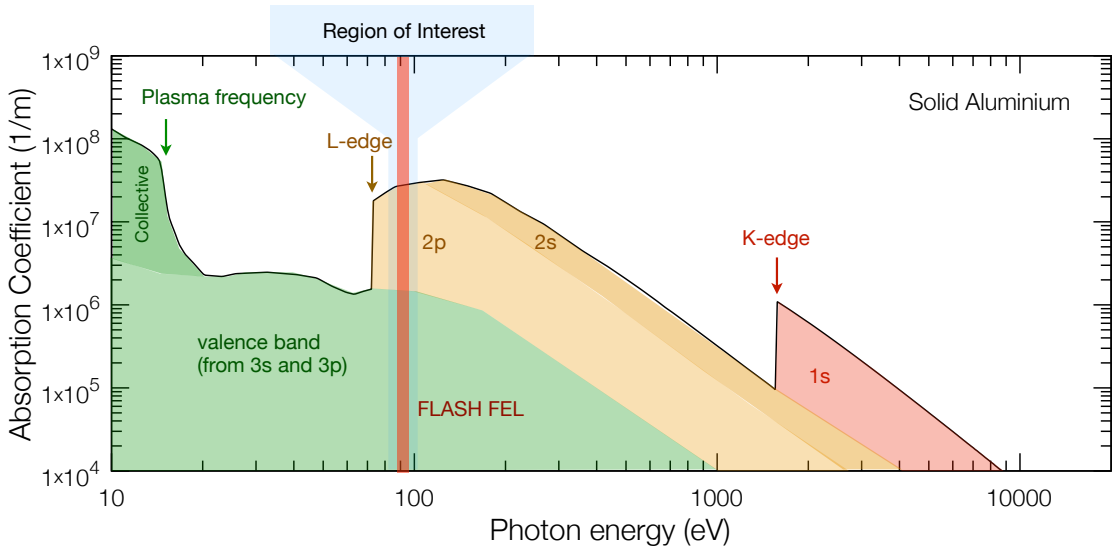

3.1 Introduction

The detailed experimental study of warm dense matter, although of strong interest to both fundamental and applied physics, is a field that has long remained elusive. The reason for this lies in the intrinsic difficulty of creating such a state of matter free of temperature and density gradients, that is to say in a well defined (p, V, T) state. To create WDM, a sufficient amount of energy must be deposited in the sample to raise the temperature to several eV. At these temperatures, the internal pressure becomes very high and the sample tends to dissociate quickly. While dissociation depends on the sample size, for metals such as Al the time scale on which loss of crystalline structure starts to occur is generally on the order of picoseconds. It is therefore of paramount importance for WDM studies that the sample can be created and probed on shorter timescales.

Until recently, two main directions have been taken to create WDM in a controlled fashion: using either optical lasers or proton beams. A third possibility only presented itself recently with the beginning of user operation of FLASH and LCLS, which is to use an XUV or x-ray free-electron laser. This source is beginning to show great potential in the field of high energy-density and WDM research, mainly due to its intrinsically short-pulse duration and exceptionally high peak brilliance. A brief description of the main advantages and disadvantages of the various sources follows.

Conventional optical lasers

The main advantage of conventional optical laser systems is their wide-spread availability, practicality of use, reasonable construction and maintenance costs and overall flexibility in the choice of operating parameters. Moreover, a large variety of optical elements are available and advanced experimental setups can be designed and tailored to the particular experimental requirements. Of particular relevance to high energy-density science are for example accurate time delayed pump-probe schemes and the availability of a variety of focussing options both in reflective and transmissive geometry. Importantly, beam diagnostics and controls are well developed.

The main drawback of these systems is the radiation wavelength. As is well known, metals are not transparent to optical light, since their plasma frequency lies in the UV region of the spectrum. Light below this frequency will primarily interact will collective electron excitations and as a result the field will be screened very efficiently. The penetration depth of optical radiation, and with it the potential for volumetric energy deposition in the sample, is therefore very small. Since these depths are on the

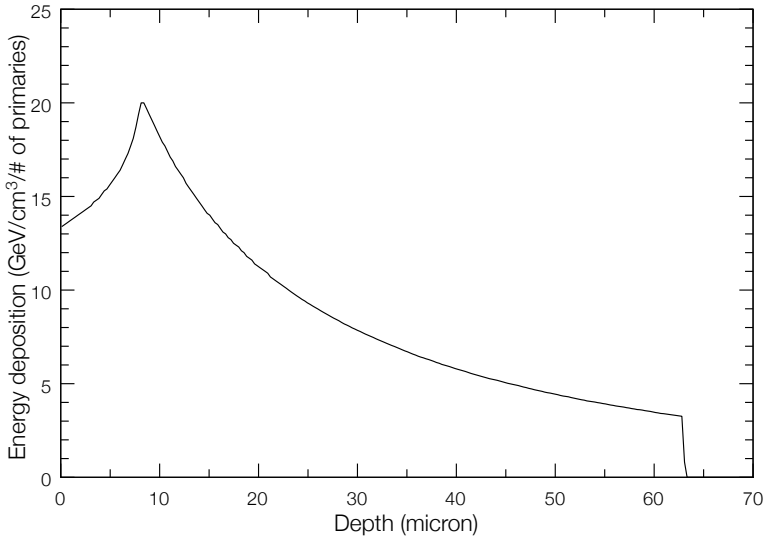

Figure 3.1: Energy deposition of a typical laser-generated proton beam (exponential energy distribution, $k_{\mathrm{B}}T = 4.6$ MeV) in a 62 μm thick Al sample. Thickness chosen somewhat arbitrarily to correspond to the Bragg peak depth of a 10 MeV proton. Calculation courtesy of F. Fiorini using the FLUKA Monte Carlo code [73].

order of only a few nanometers, the gradients in temperature and density due solely to photo-absorption for bulk samples will be generally large. This restricts the samples that can be used to materials that can be made very thin and additionally have large conductivities[1] [71]. The main volumetric heating process in such experiments is only indirectly due to the photons: it arises from the energy loss of the hot electrons created in the thin surface layer where the intense laser light interacts with the sample [72]. This produces a further complication in describing the process of target heating and plasma dynamics, and is an active topic of current research.

Proton beams

Proton beams, like hadrons in general, interact differently with matter compared with light. The energy deposition is not highest at the surface but at a given depth in the sample, depending on the initial energy of the particle. This peak is know as a Bragg peak and the proton loses energy within the distance from the surface to the peak, after which the energy deposition cuts-off rapidly.

The standard source of protons is an accelerator, most commonly a cyclotron or a

[1] For example, gold.

synchrotron, and the beam properties are generally stable and very well defined. Unfortunately such facilities tend to be limited to relatively long pulse durations so that heating matter on solid density timescales is not viable. Nevertheless, hadron beams remain a very tempting method to create high energy-density matter due to the very efficient heating mechanism they provide. This is confirmed by the construction of the FAIR facility at GSI, in Germany, aimed at producing energetic anti-proton and ion beams [74, 75].

More recently, proton beams have been generated using high-power optical lasers. The proton beam is created either by direct radiation pressure acceleration, or alternatively through a process known as target normal sheath acceleration, where the laser creates hot electrons which are expelled from the target and the protons on the surface are consequentially accelerated due to the strong electric field. Using these techniques, the proton pulse length can be significantly reduced compared to that generated by a traditional accelerator, while maintaining high particle numbers, and enabling the production of heated samples at higher densities. Much effort is being invested in addressing the main challenges of this method of generating proton beams, such as the control of the proton pulse profile and the generation of higher peak energies.

A proton beam created by a focused optical laser is not mono-energetic but has an exponential energy distribution. Assuming this beam is collimated and sent on to an Al target, it can be used as an efficient heater, since a large amount of energy can be deposited volumetrically. A simulated energy deposition as a function of sample depth is shown in Fig. 3.1, corresponding to an exponential, thermal proton energy distribution with $k_{\mathrm{B}}T = 4.6$ MeV, which is in the realm of current experimental capabilities. As can be seen, thick samples can be heated in a reasonably homogeneous fashion.

XUV and x-ray FELs

Above-optical radiation FELs provide efficient volumetric heating through the process of photo-absorption since the attenuation length is relatively long for these wavelengths (about 300 μm for 1 Å radiation in Al) and in thin targets linear absorption regimes can be achieved. Indeed, as I will show later on, under the right conditions we can do even better. Complementary to this is also the extremely short pulse duration of FELs, of duration between 10-100 fs or less, based on the operation mode, which enables the heating of samples where the density is fully inertially confined. The main difficulties with this source lie in making efficient and good quality optics at XUV to x-ray wavelengths, the intrinsic FEL beam jitter and in the accurate characterization of the energy and

temporal profile of the pulse on a shot-to-shot basis, due to the SASE FEL amplification scheme. These problems are mainly technological rather than intrinsically physical and some are already starting to be tackled, for example by FEL seeding schemes. In addition to this, we have also successfully addressed several issues during our experiments at FLASH.

3.2 Free-electron LASer in Hamburg - FLASH

The Free-electron LASer in Hamburg - FLASH, was the world's first FEL operating in the XUV region of the electromagnetic spectrum, having seen first light at 32 nm in the autumn of 2004. FLASH is a single-pass, self-amplified spontaneous emission machine, i.e., it achieves laser amplification and saturation within a single pass of the electron bunch through the 30 m long undulator section, where the lasing process is initiated by spontaneous undulator radiation. The electron bunch is created by a RF-gun based photoinjector and accelerated by a superconducting linear accelerator which enables high repetition rate operation. As the undulators are fixed gap (12 mm, producing a peak magnetic field of 0.47 T), the FEL radiation wavelength can only be selected by tuning the final energy of the electron bunch. Initially, operation was constrained to a minimum wavelength of 32 nm, but upgrades to the accelerator in 2006 and 2007 enabled reaching electron beam energies around 1 GeV, which in turn enabled lasing at a wavelength down to 6.5 nm. This result was a record at the time and was held by FLASH until first lasing was observed at the hard x-ray FEL-based Linac Coherent Light Source (LCLS) at SLAC in April 2009 at a wavelength of 1.5 Å. Some characteristic capabilities of FLASH are summarized in Table 3.1. Note that at the time of writing, FLASH is undergoing a further upgrade which, along with several other improvements and changes to the figures in Table 3.1, plans to push the wavelength further down, with the hope of reaching the *water window* between 2.3 and 4.4 nm.

We have conducted experiments on FLASH in 2008 and 2009. A schematic view of the experimental hall showing the 5 beam lines is given in Fig. 3.2. Experiments took place on two beam lines, BL2 and BL3, the former being provisioned with a focussing ellipsoidal mirror that provides a focal spot of 20×30 μm^2 and the latter providing no focussing optic. In this regard BL3 was particularly well-suited for the microfocusing experimental campaign that I will discuss in the following section, as it allowed us to install and use our own focussing optic. All shots were taken at a wavelength of 13.5 nm (92 eV), determined by the optimal reflectivity of the optic. The pulse repetition rate of FLASH is 5 Hz and the number of bunches within each pulse can be selected and tailored

Table 3.1: Nominal FLASH parameters

Parameter	value	units
Wavelength range (fundamental)	6.8–47	nm
Average single pulse energy	10–100	μJ
Pulse duration (FWHM)	10–70	fs
Peak power	1–5	GW
Average power	$\sim$15	mW
Spectral width (FWHM)	$\sim$1	%
Peak Brilliance	10^{29}–10^{30}	photons/(s mrad^2 mm^2 0.1%bw)

to the experiment at hand. For single shot operation we used a single bunch within a single pulse, while in the experimental investigations where more energy was needed, such as for emission spectroscopy measurements that will be discussed in Chapter 5, multi-bunch mode was used with 30 bunches per pulse. The energy in each pulse is measured on a shot-to-shot basis by means of a gas monitor detector.

The time structure of the FLASH pulse, and in particular its duration, is of considerable practical interest to many parts of this work. Unfortunately it has proven very challenging to measure experimentally and it has been only very recently that the first such measurements have been successfully done. Prior to this, the temporal characteristics of the pulse were estimated from electron bunch simulations. Such estimates, which account for the SASE FEL operation which amplifies individual spikes from shot noise, have shown the pulse to be very short, on the order of 10 fs [19].

The first measurements of the pulse length were conducted by Mitzner and co-workers using the autocorrelation technique [76]. They constructed a wave-front splitting autocorrelator to produce two correlated FEL pulses, one of which can be delayed in time with respect to the other, with a resolution better than 1 fs. The two pulses are then used to generate time resolved doubly charged He ions, from which the FWHM pulse length was measured to be (29 ± 5) fs. In a different experiment by Frühling and co-workers, a terahertz-field is used to drive an x-ray streak camera with fs resolution [77]. For this to work, the terahertz radiation must be synchronized with the XUV pulse and this was made possible by the installation of an additional terahertz undulator in the electron beam path so that the *same* electron bunch generates both pulses. In this experiment, the FWHM pulse length was measured to be (35 ± 7) fs.

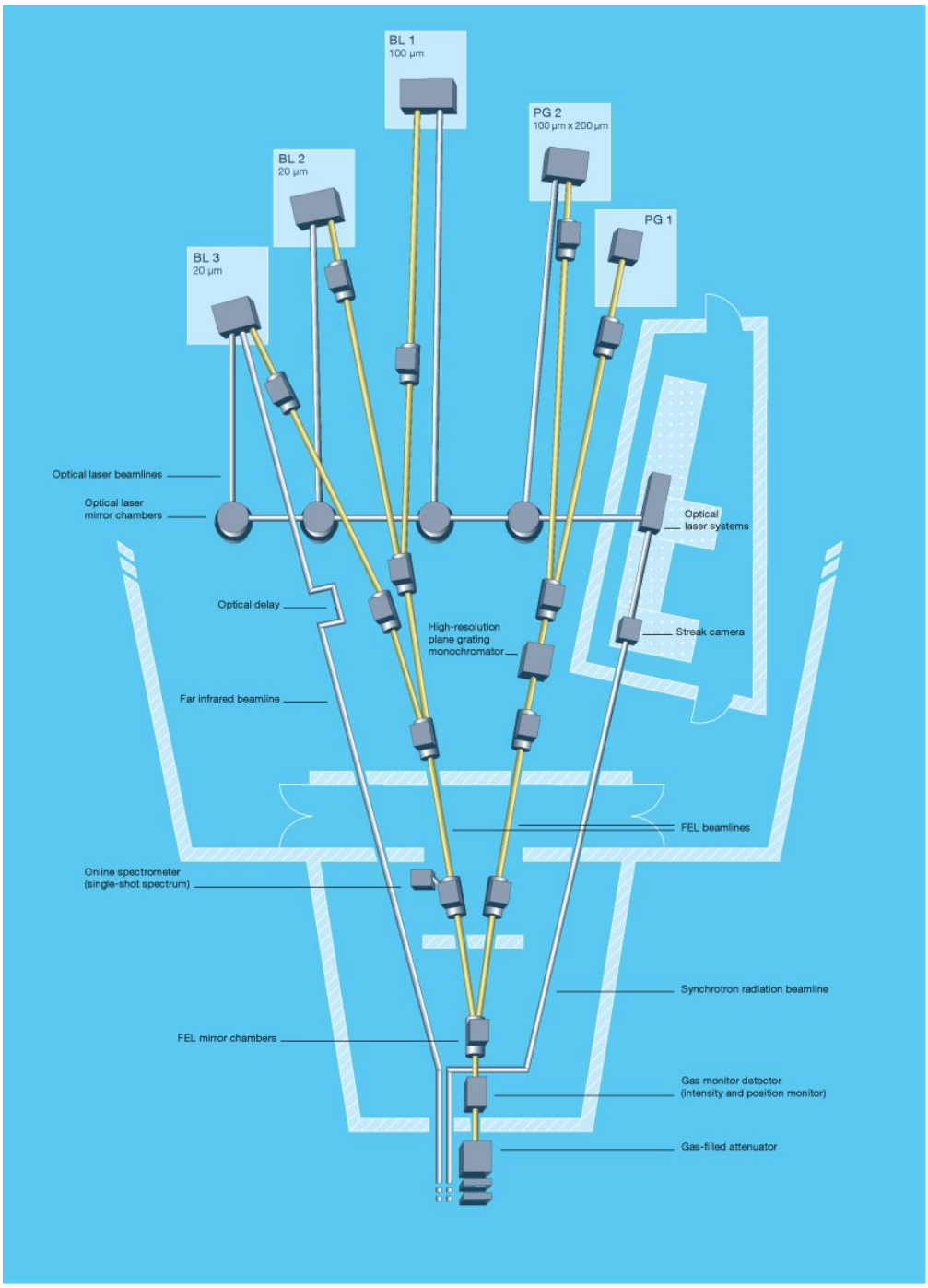

Figure 3.2: Schematic view of the FLASH experimental hall with the five beam lines BL1-3 and PG1-2. Image courtesy of DESY website [9].

3.3 Microfocusing the FLASH beam

The scope of our first experimental campaigns on FLASH was to demonstrate the possibility of creating high intensity XUV radiation at 13.5 nm. Since both the duration and number of photons in a FLASH pulse are fixed by the accelerator, the variable experimental factor is the spot size of the laser pulse. To minimize it, we used a reflective focusing scheme where the optic is an off-axis parabolic mirror (OAP) of 269 mm focal length and is coated with a Mo/Si multilayer [78]. The reflectivity of the multilayer was measured to be about 66% at 13.5 nm, when new. However, during the course of the experiment the reflectivity of the OAP decreased, due to the deposition of a thin layer of carbon in the centre of the OAP at the point of contact with the FLASH beam, and to the degradation of the multilayer due to atmospheric effects. The measured reflectivity across the OAP both before and after usage at FLASH is illustrated in Fig. 3.3(a), showing this deterioration. The coating is wavelength specific, with a rather narrow bandwidth, as can be seen in Fig. 3.3(b) for the OAP after the beam time. The two curves in this figure show the effect of the contamination in the centre (red) to the reflectivity, compared to the edges (blue), where no interaction between the FEL beam and the multilayer took place. Over almost half a year the ageing degradation is seen to be rather small. Also shown is the experimental bandwidth of FLASH during the beam time, with a specification of (13.50 ± 0.15) nm.

The spot sizes we are aiming for are one micron FWHM at best focus, or below, which would correspond to a peak intensity in excess of 10^{17} Wcm^{-2}. This places significant constraints on both the optical properties of the focusing optic and on the metrology used to measure them in virtue of the short wavelength used. The maximum intensity that can be reached depends both on the quality of the optic and on the precision of alignment. An error in either will produce aberrations that experimentally reflect in below optimal focusing performance. An especially useful way of describing such aberrations is to do so in terms of Zernike polynomials, a particular complete set of orthogonal polynomials on a unit disk [79, 80]. Spherical aberrations, coma, tilt, astigmatism, etc. can all be described in a simple way through Zernike terms, which simplifies noticeably wavefront analysis. In particular the size of these terms, when fitting the series to a measured wavefront after focusing, is a practical way of describing the combined quality of both the optic and its alignment. The surface specification to which our optic was built required that the first 36 Zernike polynomials should yield at most a 1 nm RMS wavefront error and that the RMS surface roughness is less than 0.3 nm. These 36 terms contain aberrations up to the 9^{th} order in the expansion [81].

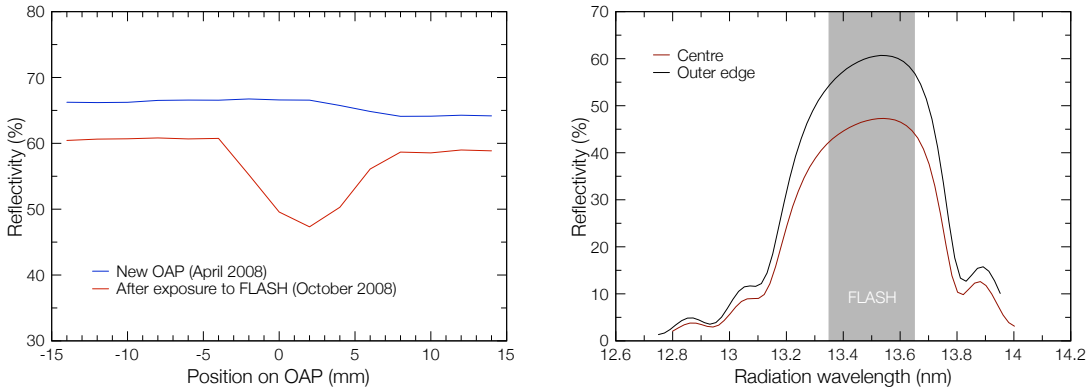

(a) (b)

Figure 3.3: Measured reflectivity of the microfocusing OAP used at FLASH. In (a) the reflectivity at 13.5 nm is shown as a function of the spatial position on the optic. The reflectivity is seen to decrease with usage as carbon is deposited in the point of interaction between the FEL beam and the multilayer. In (b) the bandwidth of the multilayer reflectivity is shown for the OAP after a period of interaction with the FEL beam. The comparison is between the portion of the OAP hit (centre) and not hit by the FEL pulse (outer edge). Also shown is the experimental FLASH wavelength. Reflectivity data courtesy of Dr. S. Bajt.

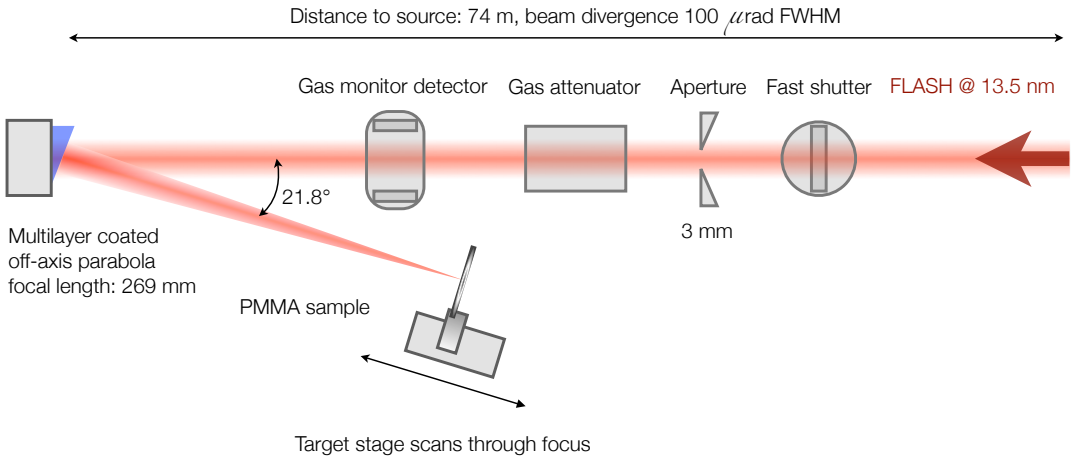

Figure 3.4: Schematic view of the setup for the FLASH microfocusing experiment conducted at FLASH beam line BL3. The off-axis parabola is focused on a PMMA target where imprints are taken at and around best focus. This technique is used for the alignment of the optic. Once aligned, the imprints are used to determine the spot sizes as a function of target position and hence give a direct measurement of the FEL intensity.

A compact way of describing the impact of aberrations on the final intensity is through the *Strehl ratio* S, which is defined as the ratio between the intensity at the Gaussian image point (best focus) in the presence of aberrations, divided by the intensity that would be obtained if no aberrations were present. This quantity is closely related to the RMS deviation of the wavefront σ [81]:

$$S = \exp\left[-\left(\frac{2\pi\sigma}{\lambda}\right)^2\right], \tag{3.1}$$

where λ is the wavelength of the radiation. A useful way to judge the quality of the focusing system is the *Maréchal criterion*, which states that the system is well corrected for aberrations if the Strehl ratio is greater than or equal to 0.8. In terms of RMS wavefront error this corresponds to $\lambda/14$, which in our case corresponds to a surface smoothness better than 1 nm RMS.

A schematic of the experimental setup is shown in Fig. 3.4. A 3 mm pinhole is used upstream so that only the central part of the FLASH pulse reaches the OAP, at which point the spot size is about 4-5 mm large due to the beam divergence of about 100 μrad

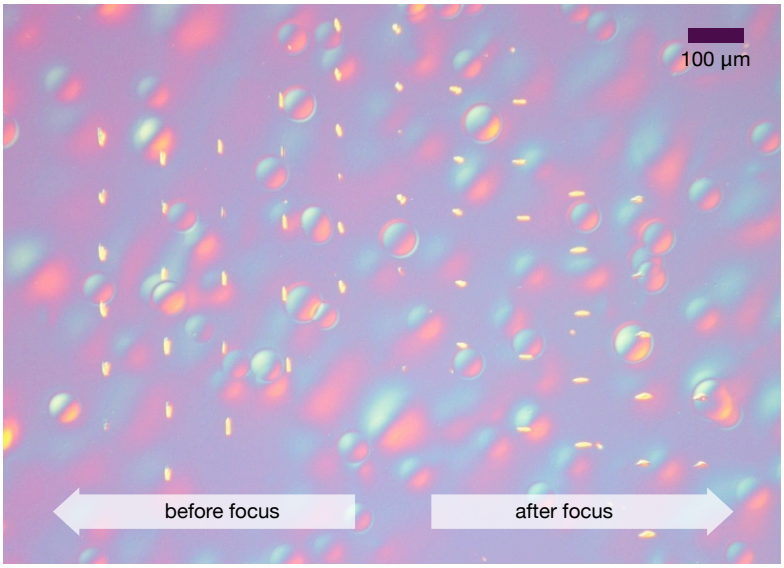

Figure 3.5: PMMA imprints displaying the OAP alignment astigmatism when scanning through focus (the ellipse rotates as we scan through focus).

FWHM. The beam is focused and imprinted on to a 5 μm thick PMMA[1]/Si(100) target in single shot operation. PMMA is used because below its ablation threshold of about 25 mJ cm^{-2} (at 13.5 nm), the laser ablation process is non-thermal and highly localized. Imprints can therefore be used for wavefront reconstruction and sub-micron spot size measurement [82]. This has been done *ex situ* by means of Nomarski differential interference contrast microscopy and atomic force microscopy in tapping mode. The energy in the incoming pulse is measured by a gas monitor detector on a shot-to-shot basis and kept below the ablation threshold of PMMA for all shots used to characterize the spot size.

3.4 Results and discussion

An example of craters in PMMA is shown in Figs. 3.5 and 3.6. From the crater analysis we have measured the minimum spot size to be < 0.7 μm FWHM. Wavefront analysis combined with beam profile simulations indicate that the OAP surface smoothness is close to $\lambda/30$, indicating minimum attainable spot sizes of below 0.35 μm FWHM [28, 78]. From these measurements it is possible to obtain a calibration relating the position of the target to the laser intensity.

[1]Poly(methyl methacrylate)

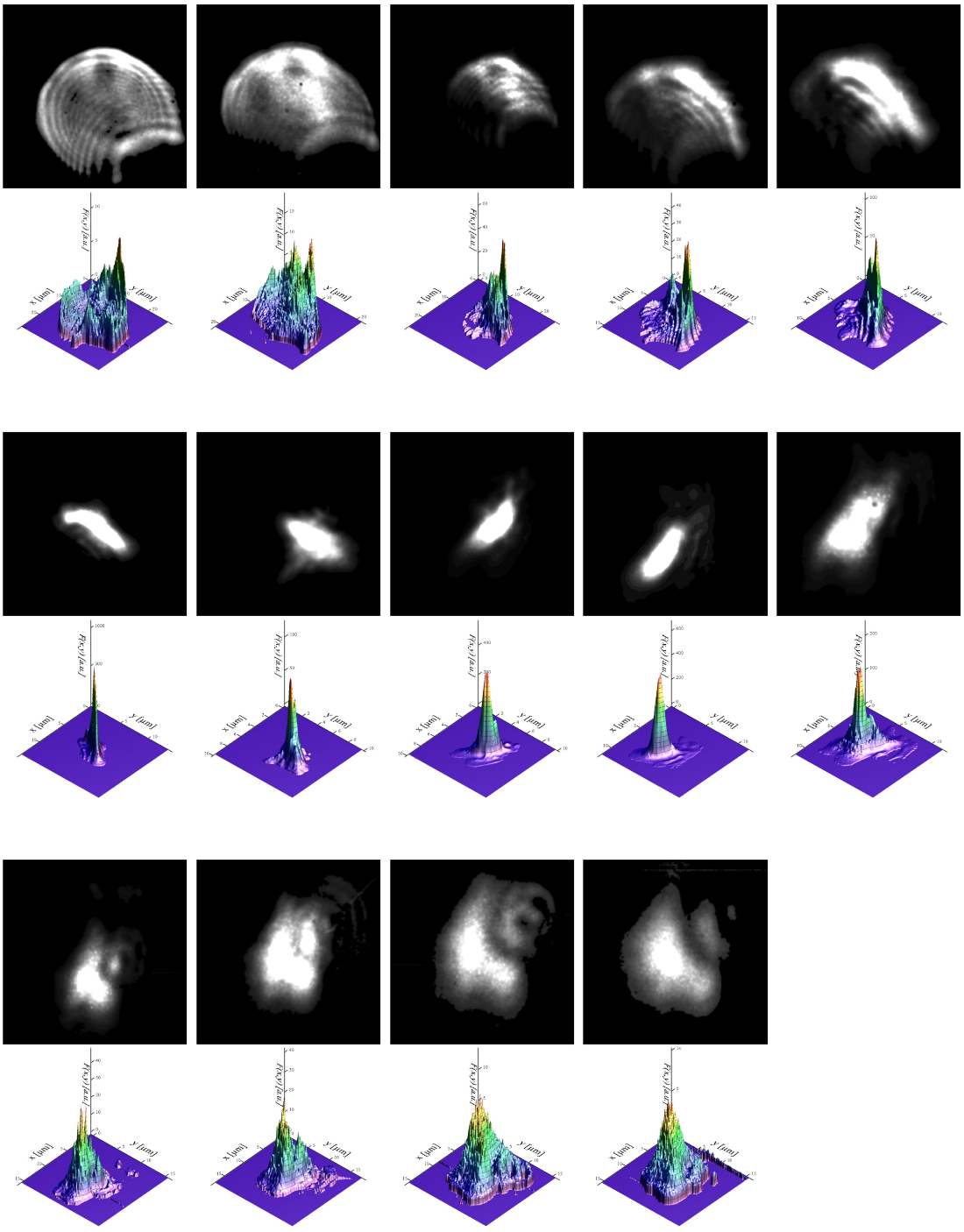

Figure 3.6: FLASH beam imprints in PMMA as the target stage is scanned through focus. Minimum spot sizes are below 1 μm FWHM, however some astigmatism can still be seen in the beam. The scanning range along the OAP focusing direction is 1.3 mm. Below the imprints are the reconstructed beam profiles for each position. Images courtesy of J. Chalupski.

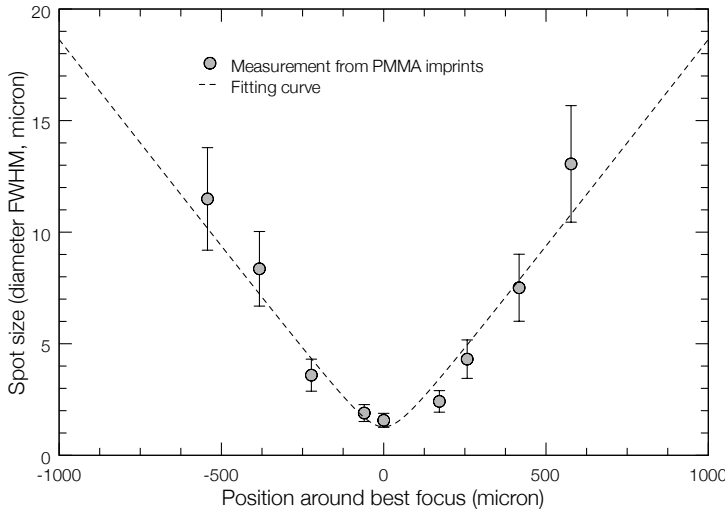

Figure 3.7: Caustic curve for the intensity calibration used for the saturated absorption measurements on Al, conducted on BL3 in July 2008. During this setup, the smallest spot size was around 1.5 μm FWHM. The calibration curve is obtained by fitting the experimentally measured point with a Gaussian focusing function (see text for more details). This is the curve used to determine the intensity scaling in Fig. 4.11.

Assuming the FEL beam to near-Gaussian, the experimental imprints can be fitted by a caustic curve of the form

$$w(z) = w_0 \sqrt{1 + \left(\frac{z}{z_R}\right)^2}, \tag{3.2}$$

where $w(z)$ indicates the waist of the beam for a particular position along the focusing axis z, w_0 the smallest spot size, and z_R the Rayleigh range. This fit is shown in Fig. 3.7, where the spot size at best focus for that particular setup is around 1.5 μm and the Rayleigh range is approximately 80 μm. This kind of calibration curves will prove very important in Chapters 4 and 5 in discussing the saturable absorption and the soft x-ray emission spectroscopy, as it gives a reliable measurement of the photon energy on target.

Although the photon energy per surface area can be estimated quite accurately through the PMMA imprints, the beam profile reconstructions show that obtaining an accurate and meaningful intensity will be more problematic. As can be observed from Fig. 3.6, the profile away from focus is not well represented by a Gaussian pulse, as the structure is very spiky wth a significant amount of energy present in the wings.

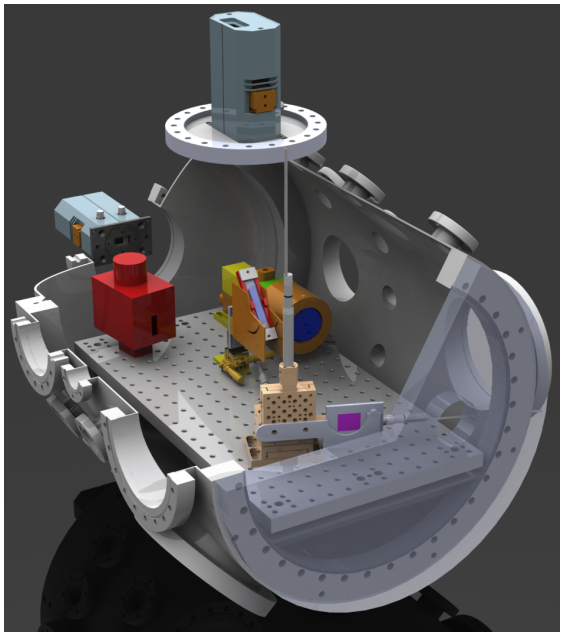

Figure 3.8: Experimental microfocusing chamber "Pizza Oven" used on FLASH, beam line BL3. Alongside the focusing optic and the target stage, two spectrometers are placed, one for the XUV region of the spectrum (at the back) and one for the x-rays (top). Image courtesy of E. Galtier.

These features are mainly due to the FLASH pulse characteristics and the effect of the optic is minimal. In addition, we also expect the temporal profile of the beam to exhibit similar features, due to the SASE operation. The combination of these two effects means that although we can determine, at a given focal position, the average photon flux and average intensity, defined as the flux divided by the FWHM pulse length, little can be said about the peak intensity. This introduces a new degree of uncertainty as for modelling purposes, we will assume the excitation pulse to be Gaussian, where the peak and average intensities are uniquely related. On the other hand, much of the physical processes of interest are non-linear and therefore depend strongly on the variation in peak intensity.

The discussion of these effects, and their implications to research on WDM, is the topic of the following two chapters, where the first experimental results will be presented regarding the absorption, heating and emission of irradiated Al samples at high intensities.

CHAPTER 4

Saturable Absorption in the XUV

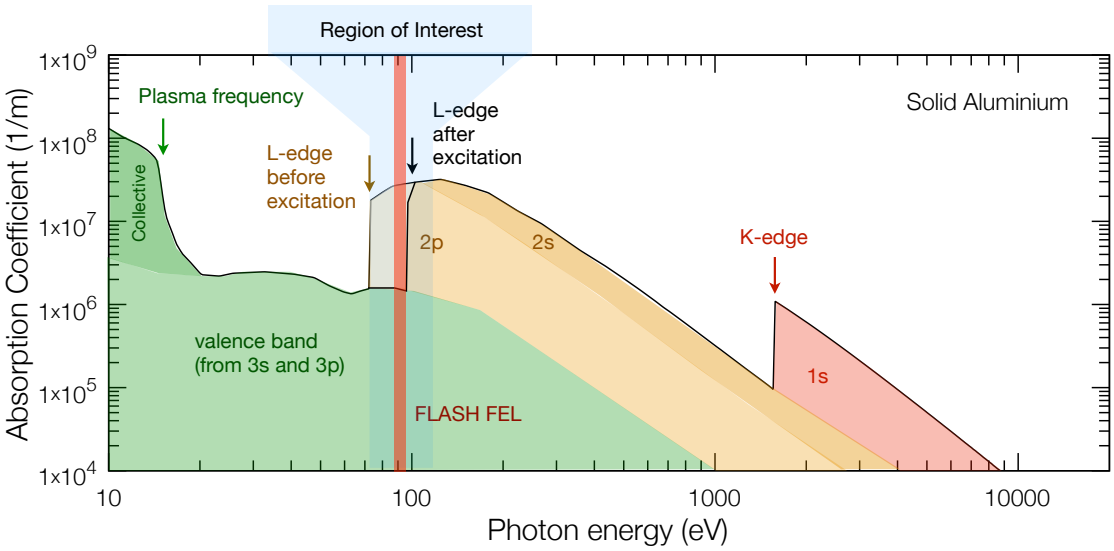

4.1 Introduction

Saturable absorption is a non-linear absorption process where by increasing the intensity of the irradiating light, the absorption in a target sample is reduced. This reduction is due to the saturation, or bleaching, of a particular electronic absorption channel when the excitation process is faster than that of re-equilibrating recombination. Saturable absorption is well known in the optical and infrared regions of the electromagnetic spectrum and is widely exploited in laser technology, where it is of particular importance in passive Q-switching and mode-locking, and allows for a simple scheme of pulse length reduction [83, 84, 85, 86, 87]. Typically used saturable materials are ion-doped YAG[1] crystals, bleachable dyes and semiconductors. Metals are not used for such purposes due to the nature of their valence bands with nearly-free, delocalized electrons, which exhibit very fast dynamics, and due to the fact that optical and infrared radiation principally excites collective excitations, plasmons, giving rise to high reflectivity and very low penetration depths in this regime.

Collective excitations and reflectivity can be overcome by exciting the sample with photons of sufficiently high energy. The energy required for this is determined by the plasmon frequency of the metal, which in turn depends on its electronic structure and, importantly, electronic density. It generally lies in the ultra-violet region of the electromagnetic spectrum. Although UV and XUV photons can be produced in several ways, the only sources of brilliant and coherent radiation at these wavelengths were, until recently, 3^{rd} generation synchrotrons, which can provide extremely stable and reliable radiation in a wide wavelength range from the soft x-ray regime to hard x-rays exceeding 60 keV [7]. However, the intensities needed to overcome the fast electron dynamics are beyond the capability of such facilities and have only become available with the recent advances in 4^{th} generation light sources: XUV and x-ray FELs. It is worth mentioning that x-ray lasers and high-harmonic generation schemes also allow access to parts of this wavelength range, however they lack the wide-range tunability of synchrotrons on one hand and the brilliance of FELs on the other.

In Chapter 3 I described the microfocusing experimental setup at FLASH, capable of delivering a high intensity radiation onto a target placed in the focus of the XUV beam. This was an important step towards investigating experimentally the detailed process of high-intensity XUV light-matter interaction, and in particular the dependence of the target opacity on the irradiation intensity.

The motivation behind this research is multiple. From the fundamental point of

[1] Yttrium aluminium garnet – $Y_3Al_5O_{12}$

view, the detailed light-matter interaction at XUV wavelengths at moderate and high intensities (10^{14} Wcm^{-2} and above) is not well known experimentally, since creating intense light sources at these wavelengths has proven challenging. The recent development of high-harmonic generation sources and FELs has now started to shed some light on this field of research. Some first efforts in this direction conducted on FLASH are described in this thesis. Various numerical codes for radiative properties of matter exist, yielding detailed information on electron transport, opacity and atomic physics in the high-intensity XUV regime (for a list of non local thermodynamic equilibrium (NLTE) codes, the reader may want to consult reference [88] p.227, Table 3). Benchmarking such calculations using reliable experimental data is essential, both to instil confidence in the theoretical models used and to improve future predictive capabilities. The importance of this extends outside the realm of FEL-matter interaction research, as these codes are widely used in several fields, such as for example in astrophysics or in studies on inertial-confinement fusion. Further, any eventual inadequacies in the numerical methods and underlining theories pave the way in the exploration and understanding of fundamental atomic and plasma physics.

High-intensity light-matter interaction is also of prime importance to the field of XUV and x-ray diffractive imaging [89, 90, 91, 92]. This is a rapidly growing field, closely tied to the availability and performance of FEL light sources, and is one of the strongest motivations behind the scientific case that is driving the construction of these expensive facilities. The imaging is done by shining the high-intensity pulse onto a sample and collecting the diffraction signal, which carries structural information of the target, averaged over the pulse length duration. One of the main concerns in these experiments is whether the image collected is representative of the system being observed. This is closely related both to the detailed absorption mechanism and to the electron and ion dynamics on femtosecond time scales. Large absorptions under high-intensity irradiation significantly heat the sample, generate very high pressures and ultimately cause the sample to degrade and explode. Work on clusters, Coulomb explosions [93, 94] and absorption in solid density matter at FLASH [29], and the first results on x-ray absorption in Ne atoms on LCLS [95], are now starting to provide the first detailed experimental information of the light-matter interaction at high intensities in atoms, clusters and solids.

Another field of research which will benefit greatly from 4$^{\text{th}}$ generation light sources, and which is perhaps the most pertinent to the following discussion, is that of high energy-density physics. As discussed in the beginning of Chapter 3, high-intensity FEL radiation in the XUV and above, impinging on a low-Z metal presents itself as an ideal

Energy shell	N (eV)	Mg (eV)	Al (eV)	Si (eV)
K	409.9	1303.0	1559.6	1838.9
L_1	37.3	88.6	117.8	149.7
L_2		49.6	72.9	99.8
L_3		49.2	72.5	99.2
Valence	3 electrons	2 electrons	3 electrons	4 electrons

Table 4.1: Energies required to excited core electrons for atomic N, Mg, Al and Si. Valence electrons are those in the highest shell that are directly involved in the bonding in the solid state. Energies taken from reference [34].

mechanism to create warm dense matter (WDM) in a controlled fashion. This chapter reports on the important first results of this investigation on FLASH, and in particular on the importance that the process of saturable absorption has in providing the ability to create very homogeneous WDM samples. As I aim to show in the following, these results place an important lower limit on the intensity needed to efficiently create well-defined states of WDM, which is an effective intensity limit on the XUV pump. Vital information regarding the other crux of WDM research – the experimental measurement of its thermodynamical properties – can also be obtained from this investigation, in particular in terms of an upper limit to the intensity, if the XUV beam is to be used as a WDM probe. A discussion of the latter constitutes the core of Chapter 5.

4.2 The process of XUV photo-absorption

The XUV absorption process consists in photo-exciting a bound electron from the system to an excited electronic state above the Fermi level. For convenience, the Fermi energy will be set to 0 eV, so all the bound states have negative energies. For isolated atoms these excited electrons may escape the system, however in a solid this is only true for the first several atomic layers, depending on the electron energy, as the electron mean free path is generally very short. The electrons excited in the bulk will therefore mainly remain in the system and loose their energy in time through electron-electron collisional thermalization. This is of relevance for the creation of hot samples as this mechanism turns out to be very efficient.

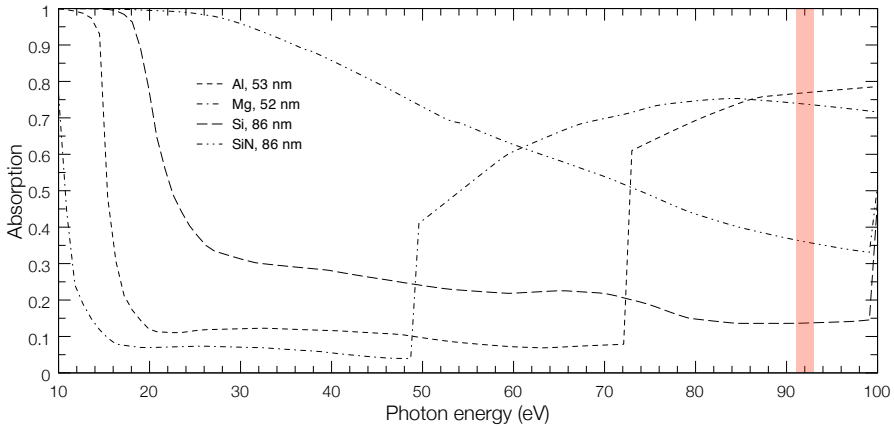

Figure 4.1: Absorption spectrum as a function of photon energy. A newly available absorption channel is seen as a sharp edge in the spectrum, since above the edge energy the additional core states can be excited. The energy levels closest to the energy of the photons have the highest absorption cross section. Contrastingly, the cross section decreases with encreasing energy difference. In red, the FLASH photon energy. Absorption data taken from reference [67].

4.2.1 Samples

We have investigated three materials, two metals and a ceramic, all at solid density:

Aluminium:	53 nm thick foil, on a mesh
Magnesium:	52 nm thick foil, coated on either side with 15 nm of Al, forming an Al-Mg-Al sandwich, placed on a mesh.
Silicon nitride:	non-stoichiometric, 86 nm thick windows in a Si wafer.

A mesh is used when the samples are too thin to be made free-standing in large sizes. Typical sizes are between 50 and 200 μm across. We took particular care to avoid hitting the mesh in all experimental investigations. All these samples have good surface characteristics, are flat, fairly inexpensive and commercially available. Importantly, they differ in the interaction with the FEL pulse as the SiN sample is an insulator, and Al and Mg are simple metals. The experimental results that will be shown and discussed were obtained for Al and SiN in July 2008 and for Mg in February 2009.

Naturally, the amount of deposited energy in the sample, its final temperature, as well as other physical processes, will depend critically on the intensity of the pulse. The characterization of the intensity is therefore of crucial importance, and is done

following the same procedures used in the microfocusing campaign described in the previous chapter:

1. The pulse duration is taken to be the same for all shots, on average (35 ± 7) fs, as measured in Ref. [77][2].

2. The total energy of the beam is measured on a shot-to-shot basis by means of a gas monitor detector (GMD). This result is cross-correlated to the measurements obtained by a photodiode for the transmission calibration (see Fig. 4.8). These measurements indicate a GMD-measured energy accuracy of around 10%.

3. The beam spot size on target, for each shot, is obtained by correlating the position of the target with respect to the best focus and a set of out-of-focus positions, for all of which the spot sizes are measured through *ex situ* crater analysis of PMMA imprints. This method is described in Chapter 3 (see Figs. 3.6 and 3.7).

From these values we conclude that the error on the intensity given by this method is expected to be around 30–40%.

The number of electrons that may participate in the absorption process is limited, through Fermi-Dirac statistics, by the energy of the excitation pulse: only those bound states with energies less than the photon energy are involved. The photon energy at FLASH was between 91-93 eV, so the number of electrons per atom that may nominally participate is as follows:

N	(Z=7)	$\Rightarrow$	valence + L_1	$\Rightarrow$ 5 electrons
Mg	(Z=12)	$\Rightarrow$	valence + L_1+$L_{2,3}$	$\Rightarrow$ 10 electrons
Al	(Z=13)	$\Rightarrow$	valence + $L_{2,3}$	$\Rightarrow$ 9 electrons
Si	(Z=14)	$\Rightarrow$	valence	$\Rightarrow$ 4 electrons

We note that there are three absorption channels, separated in binding energy: the weakly bound valence states, the L_1 shell ($2s$ electrons) and the $L_{2,3}$ shell ($2p$ electrons). The absorption cross section varies with these channels.

For N, the cross sections will be comparable for all participating electrons, as their binding energies are similar. This can be seen by the smoothness of the SiN absorption curve in Fig. 4.1. When a new absorption channel becomes available at a certain photon energy, if the cross section of the new states is significantly different, this is seen as an

[2]Our initial experiments were conducted, and the first results published, prior to this measurement. At the time, the average duration of the FLASH pulse had not been measured, and it was assumed to be of around 15 fs, this number being based on electron bunch calculations.

edge in the absorption spectrum. For Si, only the valence electrons can be excited by the FEL so this is the only absorption mechanism. This is confirmed by the smoothness of the Si curve in Fig. 4.1, up to the L-shell edge at ∼100 eV. Al and Mg are metals, and the valence electrons form a nearly free-electron gas of band width 11 eV and 7 eV. For Al, the L-shell is rather far in energy compared to the valence band and the L absorption cross section is over an order of magnitude larger than that of the valence electrons. The same holds for Mg, in particular for the L_1 shell, while the difference is slightly smaller for the $L_{2,3}$ states. This L-edge can be clearly seen for both Al and Mg in Fig. 4.1.

From these arguments it follows that or the SiN sample, all 9 electrons per SiN basis need be considered in the absorption process. For Al and Mg the main contribution will come from the 6 and 8 L-shell electrons resectively, and the valence electrons may be initially neglected.

4.2.2 Photo-excited energy levels

As discussed, a rather large number of electrons per atom are involved in the absorption process. However, it is important to stress that this holds only for the first excited electron. Whether or not several electrons may be excited in the same atom at the same time depends on a delicate interplay between the photon energy and the energy levels of the excited atom. These indeed change as a function of excitation, and in the case of core excitations, which is the dominant absorption mechanism for Al and Mg, the remaining levels see their energies adjusted to account for the newly created core hole and consequently weakened screening of the electric charge of the nucleus. For valence excitations on the other hand, such effects are expected to be small.

Aluminium	$L_{2,3}$ (eV) theor.	$L_{2,3}$ (eV) exp.	L_1 (eV) theor.	L_1 (eV) exp.
ground state	73.8	72.8 (72.9)	121.0	117.9 (117.8)
single $2p$ hole	91.1	93.4	134.6	139.2
double $2p$ hole	108.6		147.9	
single $2s$ hole	87.4		138.6	
double $2s$ hole	100.4		-	

Table 4.2: Theoretical edge energies calculated using reference [96] (see text for details). Experimental data taken from reference [97] and [34] (in parentheses).

The energy required to photo-excite a core electron depends in detail on the atomic structure. This energy is estimated by calculating the difference in energy of the elec-

Magnesium	$L_{2,3}$ (eV) theor.	$L_{2,3}$ (eV) exp.	L_1 (eV) theor.	L_1 (eV) exp.
ground state	51.1	49.9 (49.6)	92.4	89.0 (88.6)
single $2p$ hole	66.9	68.0	105.3	108.2
double $2p$ hole	82.9		117.7	
triple $2p$ hole	99.3		129.9	
single $2s$ hole	64.0		109.1	
double $2s$ hole	76.0		-	

Table 4.3: Theoretical edge energies calculated using reference [96] (see text for details). Experimental data taken from reference [98] and [34] (in parentheses).

tronic configurations corresponding to both before and after photo-excitation. For this, the Los Alamos Atomic Physics Code was used [96]. It is based on the Hartree-Fock method, and can compute excited states. For example, the ground state $L_{2,3}$-edge for Al is approximately given by the energy difference:

$$E_{\text{ph}} = E[1s^2 2s^2 2p^5 3s^2 3p^2] - E[1s^2 2s^2 2p^6 3s^2 3p^1] = (73.8 - 0)\text{ eV} = 73.8\text{ eV}, \quad (4.1)$$

and in the same way the energy of the Al L_1-edge, in the presence of a single hole in the $2p$ state, as

$$E_{\text{ph}} = E[1s^2 2s^1 2p^5 3s^2 3p^3] - E[1s^2 2s^2 2p^5 3s^2 3p^2] = (208.4 - 73.8)\text{ eV} = 134.6\text{ eV}. \quad (4.2)$$

These results for Al and Mg are summarized in the theor. columns in Tables 4.2 and 4.3. Experimental results for the ground state L-edges are rather easy to find. Henke's all-encompassing paper in particular contains the absorption edges for all elements [34]. The L-shell electron energy in the presence of a single core hole, $\tilde{E}(\text{L}')$, is in turn directly measured by K LL′ Auger spectroscopy, since for this process the energy conservation requirement is [97]:

$$E(\text{K}) - E(\text{L}) = \tilde{E}(\text{L}') + E(\text{K LL}'), \quad (4.3)$$

where $E(\text{K})$ and $E(\text{L})$ are the K and L-shell energies and $E(\text{K LL}')$ is the kinetic energy of the ejected Auger electron. The Auger energies for Al and Mg are taken from references [97, 98], and the resulting calculated core-hole absorption edges given in the exp. columns in Tables 4.2 and 4.3. Where experimental results are reported, the errors are of ±0.1 eV. The calculations are less accurate and seem to overestimate the ground

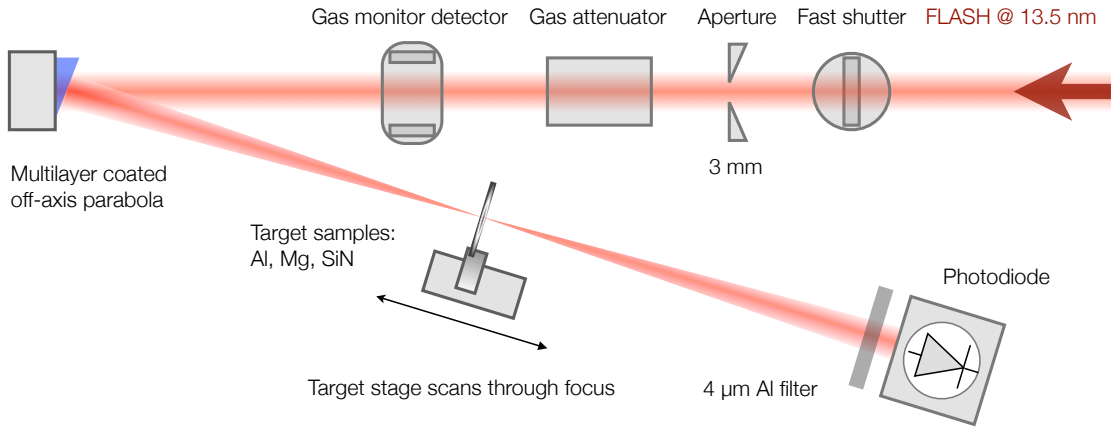

Figure 4.2: Experimental setup for transmission measurements.

state energy by around 1–3%[3]. Conversely, the calculated excited state energies are underestimated compared to experiment, by a similar amount. Note that these results were obtained using the *configuration mode* in the atomic code. They may be improved upon significantly if the *fine structure mode* is used (ground state accuracy is better than 0.5%), but with the added complication of having to account for the (many) fine-structure levels. For the purpose of this discussion, where we are interested only in the total number of electrons per atom that can be excited with the FEL pulse, such a level of detail is not required.

Considering the excitation wavelength in our experiment (see Table 4.4), it follows that only one core hole per atom may be created in the Al sample, in the $2p$ state. For Mg the situation is slightly more complicated: we may have up to three $2p$ core holes per atom, or alternatively a single $2s$ core hole and up to two additional $2p$ core holes (not shown in Table 4.3, the $L_{2,3}$ edge with a single $2s$ and $2p$ hole is 79.3 eV; with an additional $2p$ hole the edge shifts to 95.1 eV), but the $2s$ hole must be created first.

4.3 Experimental setup

The experiment consists in focusing the high-intensity FLASH pulse on to solid targets and studying the light-matter interaction and target evolution by several diagnostics, including optical, XUV and x-ray spectrometers, electron and ion time-of-flight detectors and measurements of the transmission using either a CCD or a photodiode. I will discuss

[3]Note that some degree of overestimation of the ground state is expected due to the variational theorem.

Target	GMD energy (μJ)	Photon energy (eV)	Transmission (%)
Al	(28 ± 11)	(91.0 ± 0.1)	$\sim$23 ($\sim$15 with oxide)
calibration	(27 ± 13)	(91.1 ± 0.2)	100
Al-Mg-Al	(28 ± 12)	(92.9 ± 0.6)	$\sim$16 ($\sim$12 with oxide)
calibration	(25 ± 15)	(92.9 ± 0.5)	100
SiN	(17 ± 10)	(91.8 ± 0.2)	$\sim$64
calibration	(17 ± 10)	(91.8 ± 0.2)	100

Table 4.4: Summary of the FLASH operation for the transmission data collected on FLASH for the three different samples. The GMD-measured single-pulse energies and photon energies are obtained from the statistical analysis of the shots shown in Figs. 4.9 and 4.10. The errors quoted are one standard deviation. Nominal transmissions are taken from the CXRO x-ray interactions with matter database [67] and are also shown in Fig. 4.1.

the transmission measurements in this Chapter, and the XUV spectroscopy results in the next.

The setup closely resembles that of the microfocusing experiment and is situated at FLASH beam line BL3, that was described in the previous chapter. A schematic layout is illustrated in Fig. 4.2. A multi-layer coated off-axis parabola (OAP) is used to focus the beam on to a solid target, behind which, at a distance roughly equal to the OAP focal length, a photodiode is used to measure the time integrated transmitted energy. As the full beam energy is used, in order to prevent diode saturation over the range of transmitted energies expected, the photodiode was coated with 350 nm of molybdenum and 500 nm of silicon, and additionally screened by a 4 μm thick Al filter. The FLASH FEL is run in single-shot mode using a fast shutter to select individual pulses, otherwise available at 5 Hz repetition rate. A 3 mm aperture placed upstream is used to cutoff any wings in the beam, to improve pointing stability and wavefront quality for focusing. Given the natural divergence of FLASH, the spot size on the OAP is larger than this, around 4 mm.

The reflectivity of the samples, given the small wavelength of the radiation and the normal-incidence geometry, is negligible. A measurement of the transmission is therefore simultaneously also a measurement of the absorption in the sample. The energy measured at the GMD is not the energy that is delivered on target, due to various losses

in the beam line which is not perfectly transmissive ($\sim$ 58%) and the focusing optic reflectivity, of about 60%. As a result, the on target energies are, on average, about 35% of the energy measured by the GMD, so 9.7 μJ for the Al and Al-Mg-Al samples, and 5.9 μJ for the SiN sample. The energy jitter is seen to be significant.

4.4 Transmission measurements

The data was collected on two separate experimental beam times, both using the same setup and settings. A summary of the FLASH operation characteristics for all the shots used to study the transmission of the three different samples is given in Table 4.4. The GMD-measured single-pulse energies and the photon energies are obtained from the statistical analysis displayed in Figs. 4.9 and 4.10. The errors quoted are one standard deviation, and are given as an indication of the energy and wavelength jitter during the course of the data collection, which was around six hours per sample. It is important to note that the wavelengths displayed in Fig. 4.10 are not measured directly, but are deduced from electron beam characteristics. The wavelength measurement can be done accurately using a spectrometer, but is a destructive technique, and as such not available on a shot-to-shot basis [4]. For all measurements the nominally requested wavelength was 13.5 nm (91.8 eV).

The transmission is measured in the following way: the FEL beam is aligned to hit the parabola, focus on to a well defined point on the target and centrally hit the photodiodes which are placed behind the target, about one OAP focusing distance away. The target is then removed, the FEL pulse shone straight through to the diode and its signal acquired on an oscilloscope. Apart from the mentioned 65% beam line and OAP attenuation, the energy measured from the diodes and the GMD should be the same, so these two results are cross-correlated to provide a reference and an absolute diode energy calibration. These calibrations are shown in Fig. 4.8 for the three samples. The black line shows a linear fit to the data, with a one-sigma confidence band indicated by the red lines. Once the calibration is done, the sample is moved into place at a given focal position which determines the laser intensity, and the transmission is measured by the diode, with the GMD energy measurements acquired as the reference. Through the diode calibration, assuming linearity in the response over the energy range of interest, the GMD and diode signals can be compared and the absorbed or transmitted fraction extracted. This measurement is then repeated for a set of focal positions so that a large

[4] This has changed recently after a diagnostics upgrade at FLASH, and the wavelength can now be continuously monitored.

range of on-target intensities may be obtained.

For each sample, between 5 and 10 calibration sets, and between 10 and 20 different focal position measurements were conducted. This was done so that any potential changes during the data acquisition could be monitored. The plots in Fig. 4.8 show all the calibration shots. We observed a slight systematic drift in time of the mean value of the calibration from the diode–GMD correlation plots. To avoid any influence from such effects on the final results, only the closest calibration run is used for every focal scan of the transmission, rather than all of them combined. However, a comparison to the results obtained using the single, combined calibration, shows that these affects are of minor importance.

Another feature of interest is the indication of non-linear behaviour in the diode-GMD calibration, in particular in the low energy region below 5 μJ. This is the reason for the linear fitting function not passing through the origin in Fig. 4.8, as would be expected since a null signal on the photodiode necessarily corresponds to a null signal on the GMD. However, given the energy distribution of Fig. 4.9, most shots lie outside the problematic region, where a linear fit is meaningful. Moreover, a threshold discriminator is used to eliminate potentially problematic diode signals of very low-energy from the analysis, when the shape of the signal cannot the reliably established. This turns out to remove most shots that were measured by the GMD to have an energy below 1 μJ, for both the Al ad SiN samples. For these reasons, and because the calibration confidence band is rather large, non-linear effects will not be considered in the transmission analysis. Note that for the Al-Mg-Al sandwich sample, a large amount of poor diode signals is observed, which correlate less well with low energy pulses as measured by the GMD. This can be observed in Fig. 4.9 by comparing the light and dark grey histograms, and indicates a problem in the setup, perhaps with the alignment, that leads to rather noisy data (see the single-shot and intensity-grouped data in Fig. 4.12).

An Al foil in contact with air oxidises very quickly and a surface layer of Al_2O_3 is created, the thickness of which is generally around 10 nm [99]. For thin foils, such as those we are using, where the oxide layer is of comparable thickness to the sample, the oxide contribution to the transmission must be considered. For this purpose, after the transmission measurements on the 53 nm Al foil at FLASH, the cold sample transmission was measured on the Advanced Light Source synchrotron in Berkeley to be 15%. The cold transmission measured on FLASH is in agreement with this result, which is also consistent with the expected oxide layer thickness of approximately 10 nm on each side of the foil, and a remaining Al thickness of 38 nm in between.

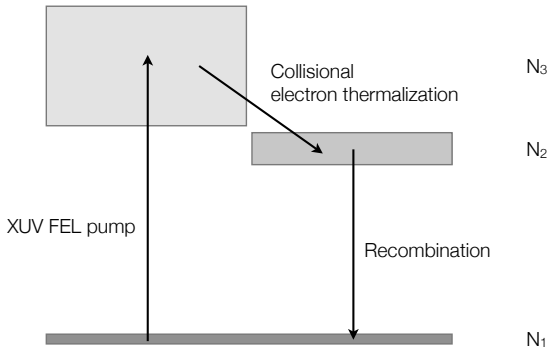

Figure 4.3: The effective absorption three-level system comprised of a core state of population N_1, the ground state valence band with a population N_2 and the energy region above the valence band with population N_3. The depletion of N_1 is responsible for the saturation of the absorption.

4.5 Saturable absorption

As shown in Figs. 4.11 and 4.12, the data for Al and Mg shows a trend that indicates saturation of the main absorption channel, when the FEL fluence is increased above a given threshold. A simple model can be constructed to yield some insight into the dynamics on the absorption and saturation processes on ultra-short time scales.

4.5.1 Theoretical model

The interaction of both Al and Mg with the high intensity FEL pulse can be modelled by considering an effective three-level system. The first level is represented by the occupancy N_1 of the core states ($2p$ or $2s$), the second level by the ground state valence band occupancy N_2, and the third by the occupancy of the band structure energy space above the valence band, N_3. This scheme is illustrated in Fig. 4.3, where the excitation FEL pulse predominantly interacts with the core states and excited them well above the valence band, by several tens of eV. These excited electrons then loose their excess energy and thermalize with the valence electron on a femtosecond time scale and eventually recombine with the core holes. The opacity of the sample depends strongly on the population of the dominant absorption channel N_1. Considering that the pumping is off-resonance with respect to the recombination, stimulated emission need not be considered

and a simple rate equation for N_1 can be written in the form

$$\frac{dN_1}{dt} = -W(t)N_1 + \frac{(N_{\text{val}} + N_{\text{core}} - N_1)(N_{\text{core}} - N_1)}{N_{\text{val}}}\frac{1}{\tau} \tag{4.4}$$

$$N_1(0) = N_{\text{core}}. \tag{4.5}$$

Here N_{core} and N_{val} are constants representing the number of excitable core electrons and the number of valence electrons in the ground state system. In the case of Al we have, for example, $N_{\text{val}} = 3N_{\text{core}}$. Furthermore we have assumed the transition $N_3 \to N_2$ to be very fast, i.e., quasi-instantaneous thermalization, so that $N_3 \simeq 0$ for all t. The population of the N_2 state following this notation is therefore given by $N_{\text{val}} + N_{\text{core}} - N_1$. The first term on the rhs of Eq. (4.4) is the FEL driven excitation, given by (e.g. see page 65 of Ref. [100]):

$$W(t) = \frac{\kappa_c}{\rho}\frac{1}{h\nu}\mathcal{P}(t), \tag{4.6}$$

where κ_c is the absorption coefficient of the core level in the low intensity limit, ρ the atomic density, $h\nu$ the FEL photon energy and $\mathcal{P}(t)$ the FEL beam profile, which contains all information on the shape and intensity of the pulse.

The second rhs term of Eq. (4.4) represents the relaxation which is driven mainly by Auger decay and is as such dependent on the number of electrons present in both states involved in the transition. The constant τ is the core hole life time, taken to be 40 fs for Al and 30 fs for Mg. Equation (4.4) is simple to solve computationally to yield the time-dependent population of the dominant absorption channel throughout the duration of the pulse, and after. An example for various conditions relevant to this investigation is depicted in Fig. 4.4.

The time-dependent transmission through a foil of thickness d can now be simply evaluated by considering the combined effect of the saturable core absorption channel and the non-saturable valence channel:

$$T(t) = \exp\left[-\left(\frac{N_1(t)}{N_{\text{core}}}\kappa_c + \kappa_v\right)d\right]. \tag{4.7}$$

To compare the calculations with the experimental values two additional considerations must be made. First of all, a non-saturating absorption term must be added to Eq. (4.7) to account for the oxide layer which is present on both sides of the experimental sample. Secondly, from the experiment only the total transmitted flux F at a given intensity is

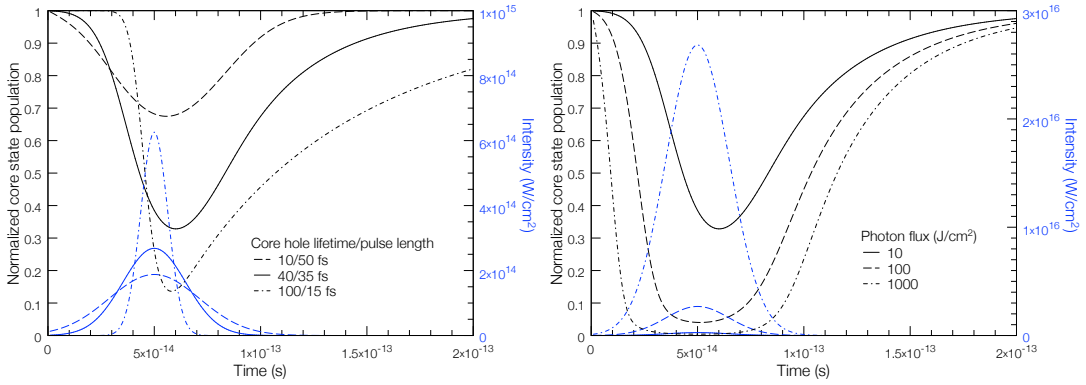

(a) Photon flux constant at 10 Jcm^{-2}

(b) Pulse duration 35 fs (FWHM), core hole lifetime 40 fs

Figure 4.4: Core level population for Al ($2p$ state) irradiated by a Gaussian pulse. The population curve depends on the pulse shape and duration, as well as on the core hole lifetime, dominated by Auger recombination, and the excitation photon flux. The effect due to the interplay between pulse length and recombination time scales is illustrated in a) while b) shows the population at various fluences, exhibiting the saturation effect.

measured, which can be obtained by integrating Eq. (4.7) over the duration of the pulse:

$$F(I) = \frac{\int dt\ \mathcal{P}(t)T(t)}{\int dt\ \mathcal{P}(t)}. \tag{4.8}$$

This transmitted flux, as a function of the FEL pulse intensity constitutes the theoretical absorption model in Figs. 4.14 and 4.15.

4.6 Target heating

The efficiency at which a target can be heated to multi-eV temperatures by volumetric photo-excitation is of considerable practical interest for creating well-defined samples of high energy density matter. Taking into consideration that almost all the energy from the FEL pulse is absorbed by the Al L-shell states by bound-free absorption, a simple transmission measurement suffices to estimate the total amount of energy absorbed in the focal region, and by it, the peak temperature attained. To illustrate this point, consider a FEL beam of very short duration and known fluence hitting a well-defined area of a thin Al sample. If only a single core electron can be excited from each atom during the pulse, the total number of excited atoms can be obtained by simply dividing

the total energy lost by the beam and the photon energy. The energy that each of these atoms gain in the absorption process is given by the difference in energy of the atomic bound state, E_b and the photon energy E_{ph}. For the case of the $2p$ level in Al and 92 eV excitation, this amounts to 19 eV. The maximum temperature that can be achieved at a given intensity, considering only the excitation process, can then be calculated assuming this energy is equilibrated among the valence band electrons.

For simplicity, consider the initial state to be composed of the electron population after an instantaneous excitation and before any equilibration or recombination takes place. This is illustrated by the blue curve in Fig 4.5, for a set of FEL fluences, corresponding to different numbers of excited electrons. The valence band occupancy is obtained by multiplying the free-electron DOS, $g(E)$, with the Fermi-Dirac distribution function $f_T(E)$ at room temperature. All the excited electrons from the $2p$ core are peaked at 19 eV above the Fermi energy, which is set to the origin. The electron density in the pre-equilibration valence band, in terms of electrons/atom, is given by the integral

$$N_v^i = \int_{-E_f}^{\infty} g(E) f_T(E) dE = 3. \tag{4.9}$$

The excited electron density N_{ex} in turn depends on the photon flux. The integral over this peak at 19 eV is given by

$$N_{ex}^i = \int h(E) dE, \tag{4.10}$$

and is for the four cases in Fig. 4.5 equal to 0.1, 0.25, 0.5 and 1.0 electrons/atom. The mean energy of the system is given in a straightforward manner by

$$\langle E \rangle^i = \int_{-E_f}^{\infty} [\, g(E) f_T(E) + h(E) \,]\; E \; dE, \tag{4.11}$$

and is uniquely determined by the energy absorbed by the system from the FEL.

The blue curve in Figure 4.5 shows the excited electron distribution which is strongly out of thermal equilibrium. The system will equilibrate on time scales dictated by valence band collision rates to a certain temperature T' following Fermi-Dirac statistics and will be characterized by a mean energy given by

$$\langle E \rangle^f = \int_{-E_f}^{\infty} [\, g(E) f_{T'}(E) \,]\; E \; dE. \tag{4.12}$$

If we assume that during this equilibration process no energy is lost from the system (e.g., through transverse electron transport), the energies must remain the same and we

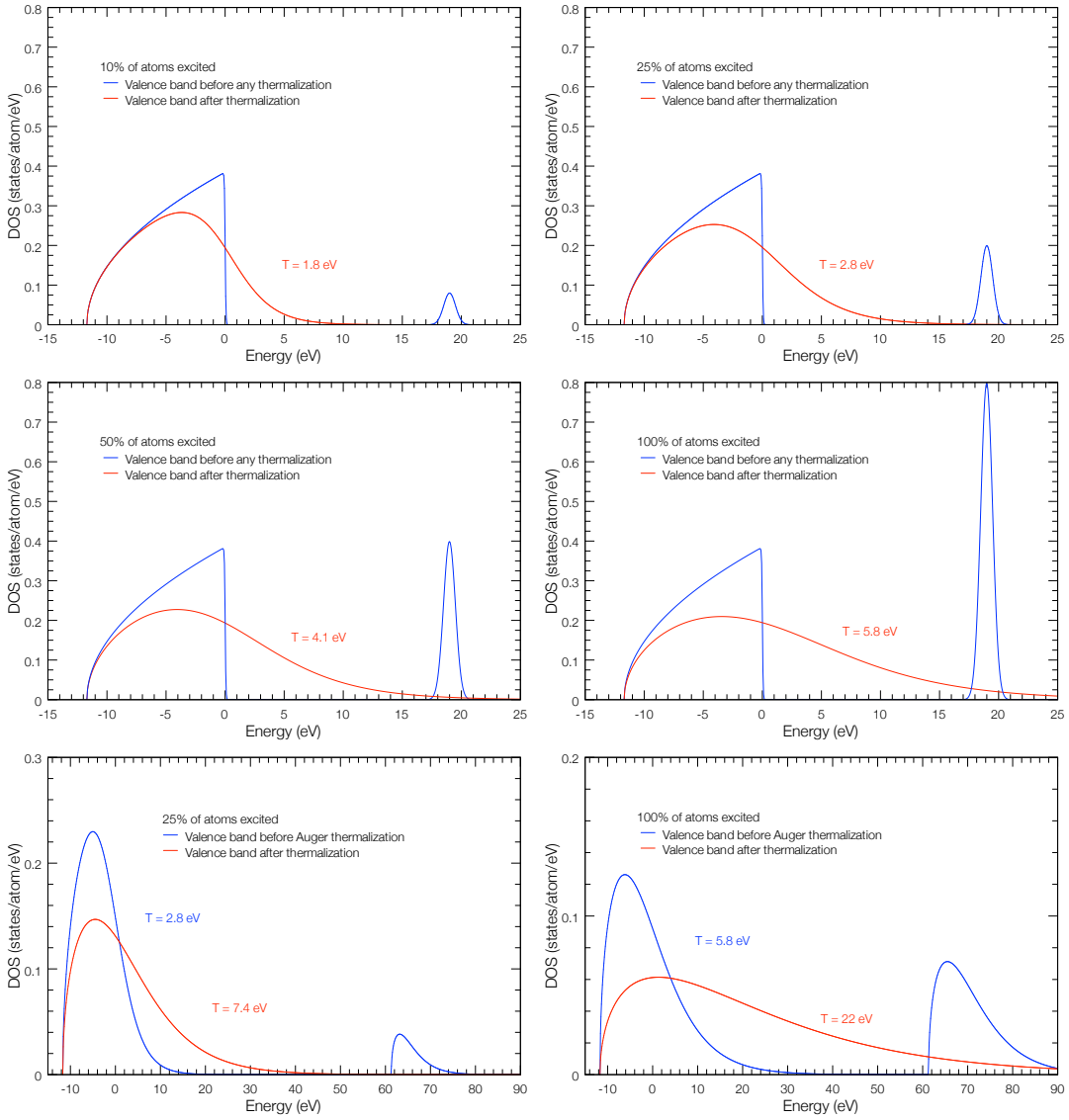

Figure 4.5: Electron distributions before and after equilibration. The first four represent the photo-excitation final state after four different FEl intensities. The final two show the electron distribution after equilibration of the excitation energy and after the Auger process, but before Auger equilibration. The amount of energy provided by the Auger effect is significantly higher than that provided by direct photo-excitation of the bound states.

must have

$$\langle E \rangle^i = \langle E \rangle^f. \tag{4.13}$$

This equation defines the final equilibration temperature T' in terms of the excited electron density $h(E)$ which in turn depends on the pulse fluence. The equilibrated distributions that satisfy Eq. (4.13) are shown in red in Fig. 4.5, from which we find the highest temperature that can be achieved to be just below 6 eV. Note that the FEL beam profile has a certain structure, which even in the context of this simple treatment will translate initially into inhomogeneous heating within the region of the focused spot size. This is on the order of several μm and whether electron collisional thermalization can equilibrate such differences within a few femtoseconds is questionable. A given flux can therefore exhibits a range of temperature profiles, however, as this estimate makes use only of the total flux of the FEL beam, the maximum temperature is insensitive to the beam's temporal and spatial profile, provided only one electron can be excited per atom.

It is important to point out that photo-excitation is not the most efficient sample heating process. As noted previously, during this excitation only about 19 eV per atom are deposited into the valence band of Al for each electron that absorbs a photon of 92 eV. Most of the energy goes into overcoming the bound state potential of the nucleus. After the excitation however, the system is left with a number of core holes and the way in which these recombine is very important. Radiative recombination is of great interest as it allows us to extract some information about the system, as will be discussed in detail in Chapter 5. From the energy prospective however, this process is insignificant as the potential energy contained in the core hole state is passed over to the photon and is ejected from the system. Higher order effects do allow some energy to be retained, and this, again, will be discussed in the following chapter, but the overall contribution to the energy budget due to radiative recombination is negligible.

Direct valence band absorption is a strong candidate for efficient heating as an excitation of one of the three highest-lying electrons keeps all the energy of the photon in the system, in stark contrast with bound state excitation. However, we note that at the energies that are being considered here, free-free absorption is almost two orders of magnitude weaker than the bound-free part. This is illustrated by the cross sections of the green and orange regions at 92 eV in Fig. 1.1. It follows that we expect the free-free absorption to only have a marginal effect on the peak temperatures.

As mentioned, radiative recombination of a core hole is energy-neutral. However, this process in Al is negligible: only about 0.24 % of all the $2p$ core hole states recombine this

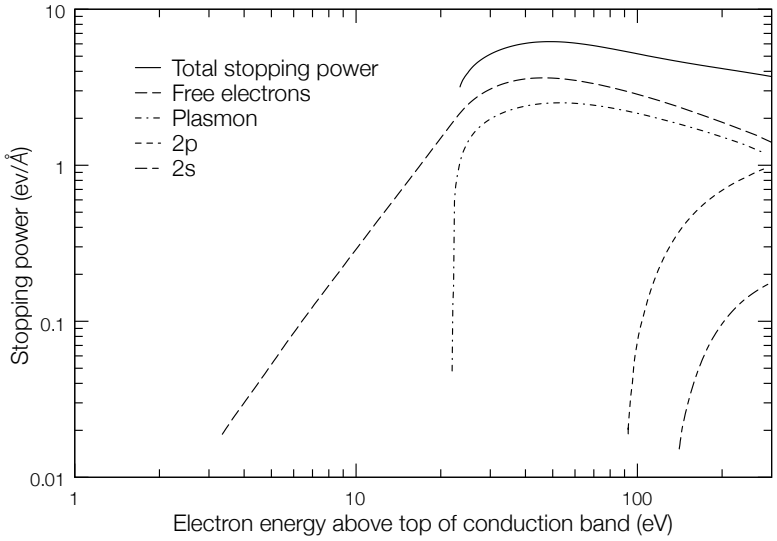

Figure 4.6: Electron stopping power in Al, decomposed into the various contributions. Data taken from reference [102].

way [101]. The vast majority recombine non-radiatively, through the LVV Auger effect, where an electron from the valence band fills the core hole and the energy released by this is given to a second electron in the valence band, which is excited. This process is very important for heating, since the main free path of an electron at $\sim$73 eV in Al is only a few lattice spacings [102] and these excited electrons mostly heat the valence band rather than leave the sample. The peak temperature considering only Auger recombination can be estimated following the same approach taken to obtain the photo-excitation temperature, i.e., Eq. (4.13), but changing the term $h(E)$ in Eq. (4.11) to account for the peak at 73 eV. In this case, the highest temperatures that can be reached assuming all atoms have a single core hole is 15 eV. The combined contribution of photo-excitation and Auger recombination is illustrated in the last two plots in Fig. 4.5 for two intensities and the peak temperature reached is 22 eV.

Thermalization timescales

The time it takes to thermalize the excited electrons and create a hot valence band is of considerable interest, especially in materials where hot electrons significantly effect the band structure of their environment. In some recent calculations this has been shown to be the case for metals like Au, but not for Al [103].

A simple estimate of the thermalization time can be obtained by considering the

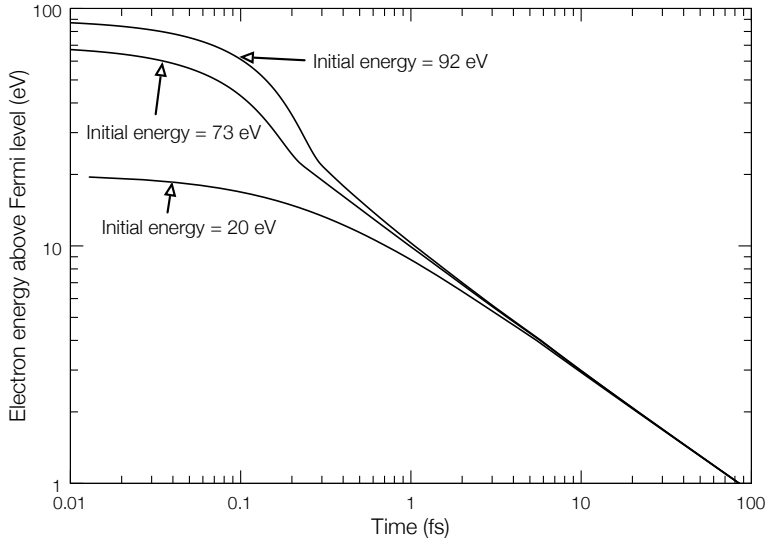

Figure 4.7: Temporal evolution of electron thermalization for electrons starting with 92 eV, 73 eV and 19 eV, corresponding to the processes of valence photo-excitation, Auger recombination and core photo-excitation.

stopping power $S(E)$ of an electron of kinetic energy E in bulk Al. According to free-electron theory, which is rather accurate in describing the valence band electrons of Al, this quantity is given by [102]:

$$S(E) = \frac{2m_e e^2}{h}\frac{1}{E}\int_0^E d\omega\ \omega \int_{q_-}^{q_+}\frac{dq}{q}\ \mathcal{I}m\left[-\frac{1}{\varepsilon(q,\omega)}\right], \tag{4.14}$$

with the integration limits in q-space

$$q_\pm = \frac{\sqrt{2m}}{\hbar}(\sqrt{E} \pm \sqrt{E-\hbar\omega}). \tag{4.15}$$

Here $\varepsilon(q,\omega)$ is the electronic dielectric function. For this discussion I will use the stopping power considered initially by Ashley *et al.* [102], which includes several corrections to the RPA dielectric function. The underlining approach remains unchanged, however the details of the electron energy loss are changed slightly producing a more realistic model that can be compared with experimental data on Al. Separated into its multiple contributions, the stopping power is shown in Fig. 4.6.

Given the stopping power, the temporal evolution of the energy loss can be obtained in a straightforward manner by integrating Eq. (4.14) in energy. There are two basic

heating channels: photo-excitation of a valence band electron or $2p$ core electron by an FEL photon and the subsequent Auger recombination of the core hole. Roughly 1-5 % of the photons are absorbed by the valence band. This creates an energetic electron with about 80-90 eV of energy above the Fermi level. All the other photons are absorbed by a core electron which is excited to 19 eV above the Fermi level. These processes are extremely fast and occur throughout the duration of the excitation pulse. Later on, the core holes recombine predominantly by Auger recombination. Through measurements of the Auger electrons the time scale on which this happens is seen to be (40 ± 20) fs [104]. The final state of this process has an electron of energy 60-70 eV above the Fermi level.

The electron energies as a function time after their initial excitation are shown in Fig. 4.7, from which we note that most of the excitation energy is ceded to the remaining valence band within the first 10 fs. As this time scale is shorter than that of radiative recombination, we expect the system to be close to thermal equilibrium when the fluorescence is emitted. Clearly, as the emission takes place, the large amount of Auger recombination will cause additional heating, so that only an average temperature can be obtained.

4.7 Results and discussion

As can be seen from the transmission measurements in Figs. 4.11 and 4.12, both the Al and the Al-Mg-Al targets show a significant change in the transmitted light with increasing pulse intensity. This trend is consistent with the saturation of the L-shell absorption channels, in the atoms of the metals. The remaining opacity of the sample at highest intensities is due to the valence band absorption, which is small, and to the absorption from the oxide layer. In turn, the SiN sample does not seem to exhibit saturable absorption for intensities below 10^{16} Wcm^{-2}, as can be seen from Fig. 4.13, at least not within the rather large experimental error. Again, given the target thickness and the number of electrons per atom, available to participate in the absorption process, this observed result is not surprising.

The results shown in Fig. 4.14 and 4.15 provide the first experimental observation of saturable absorption in the XUV region of the spectrum in solid targets. This is of fundamental interest because it demonstrates that it is both possible as well as practical to tune the absorption of a solid sample by carefully choosing the wavelength of the excitation pulse. If, for example, the FEL pulse irradiating the Al foil had a photon energy only a couple eV higher, an additional $2p$ electron per atom could be excited and the transmission curve of Fig. 4.11 would change significantly, shifting to higher

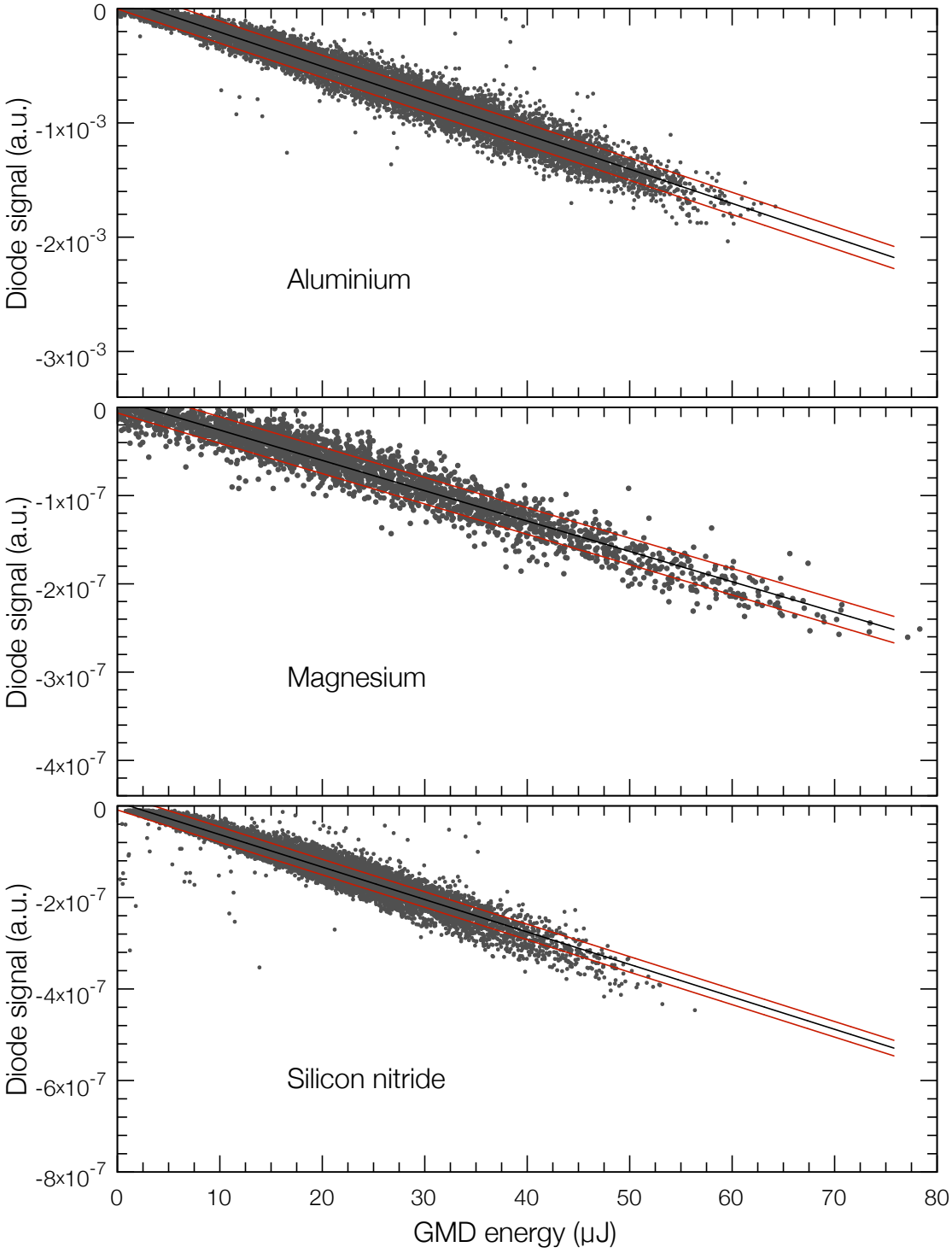

Figure 4.8: Diode-GMD calibration curves. Red lines indicate the 1-σ confidence band.

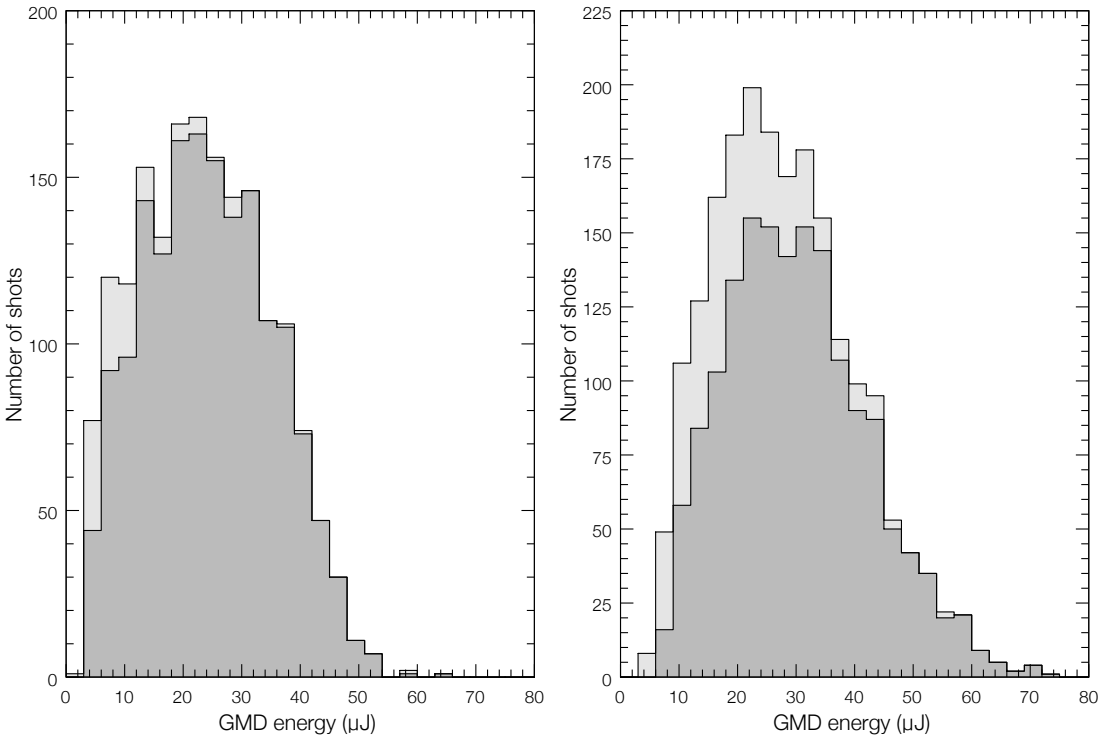

(a) Aluminium

(b) Magnesium

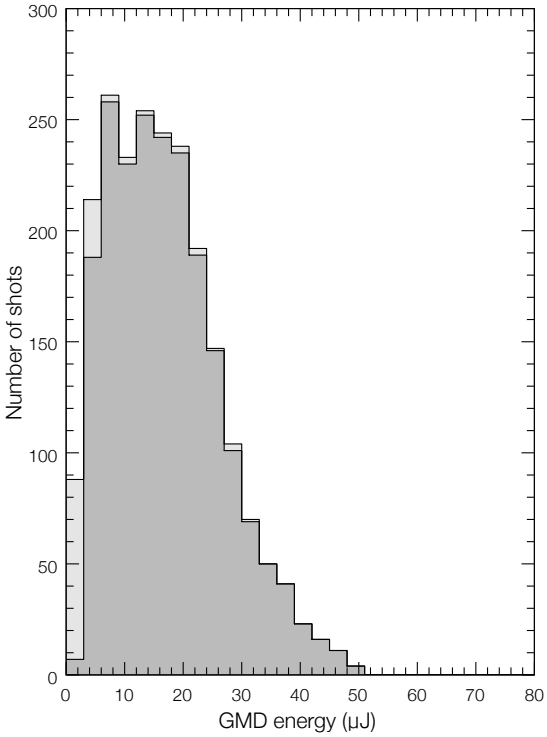

(c) Silicon nitride

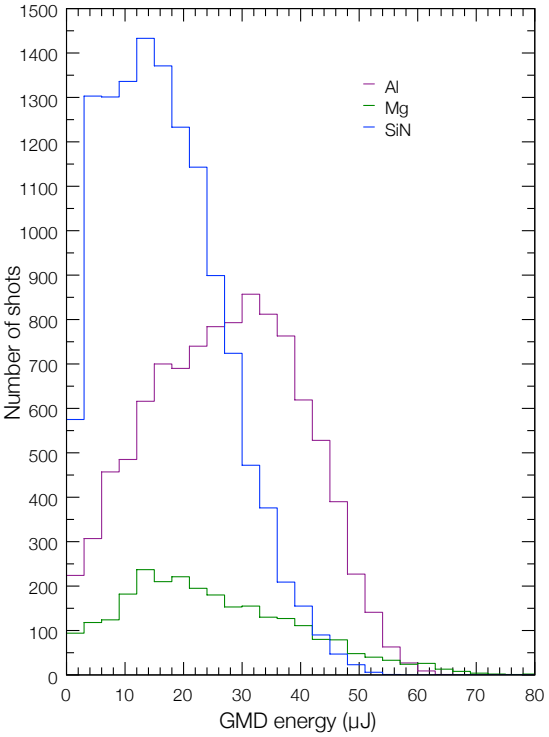

(d) Calibrations

Figure 4.9: FEL pulse energy distribution for transmission measurements.

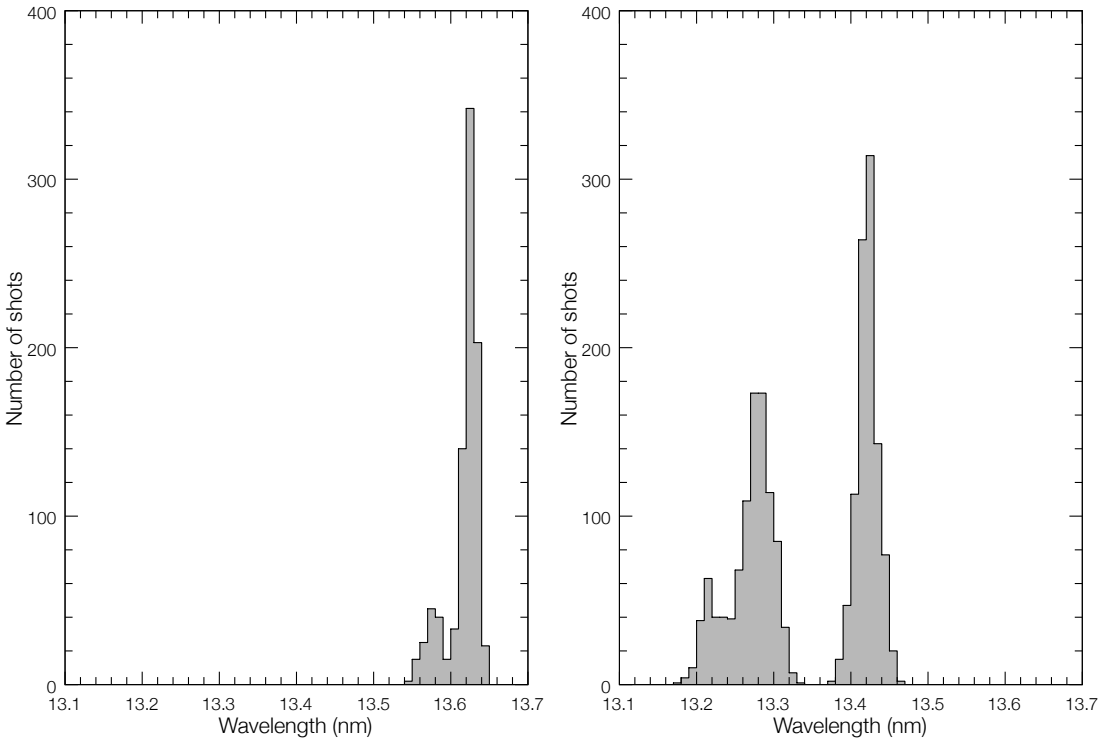

(a) Aluminium

(b) Magnesium

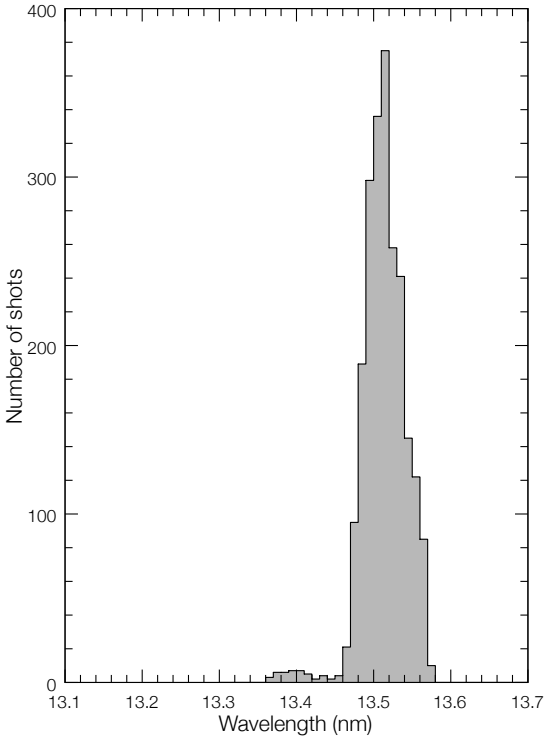

(c) Silicon nitride

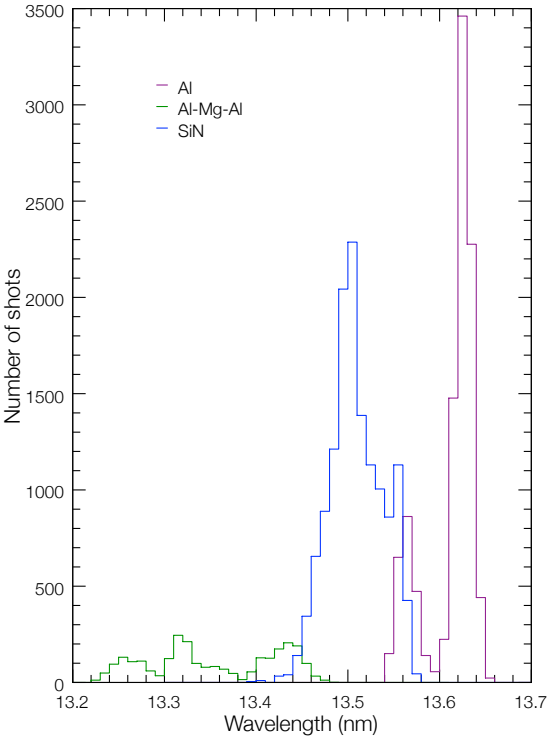

(d) Calibrations

Figure 4.10: FEL pulse wavelength distribution for transmission measurements on Al.

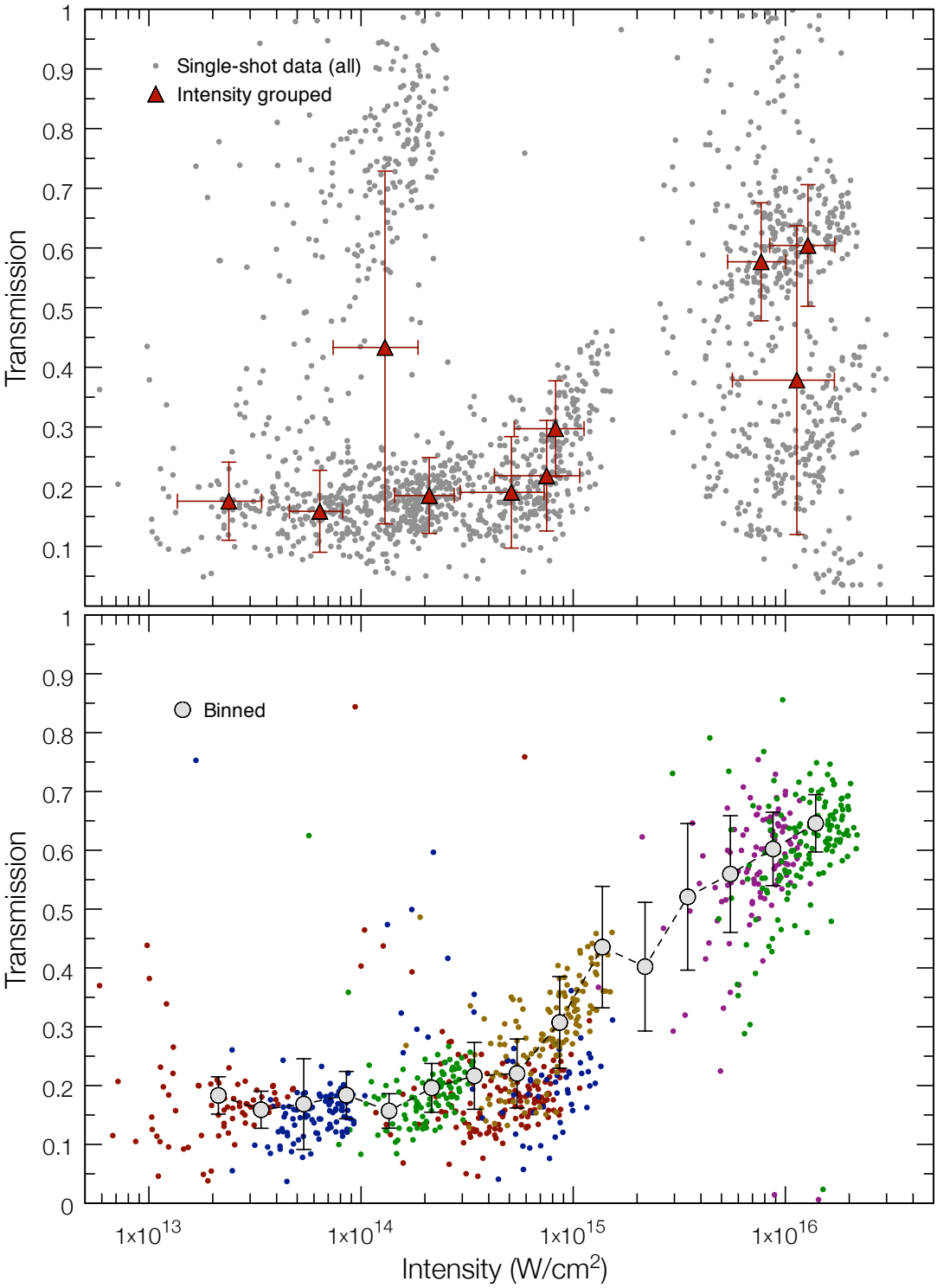

Figure 4.11: Transmission as a function of intensity in Al. Top plot shows all single shots (above a set pulse energy and diode signal threshold, in grey) and the average transmission value for a given position in focus (red). Bottom plot shows the single shot results after a selective filtering (colours indicate the focal position) and the corresponding binned results in intensity. See text for further details.

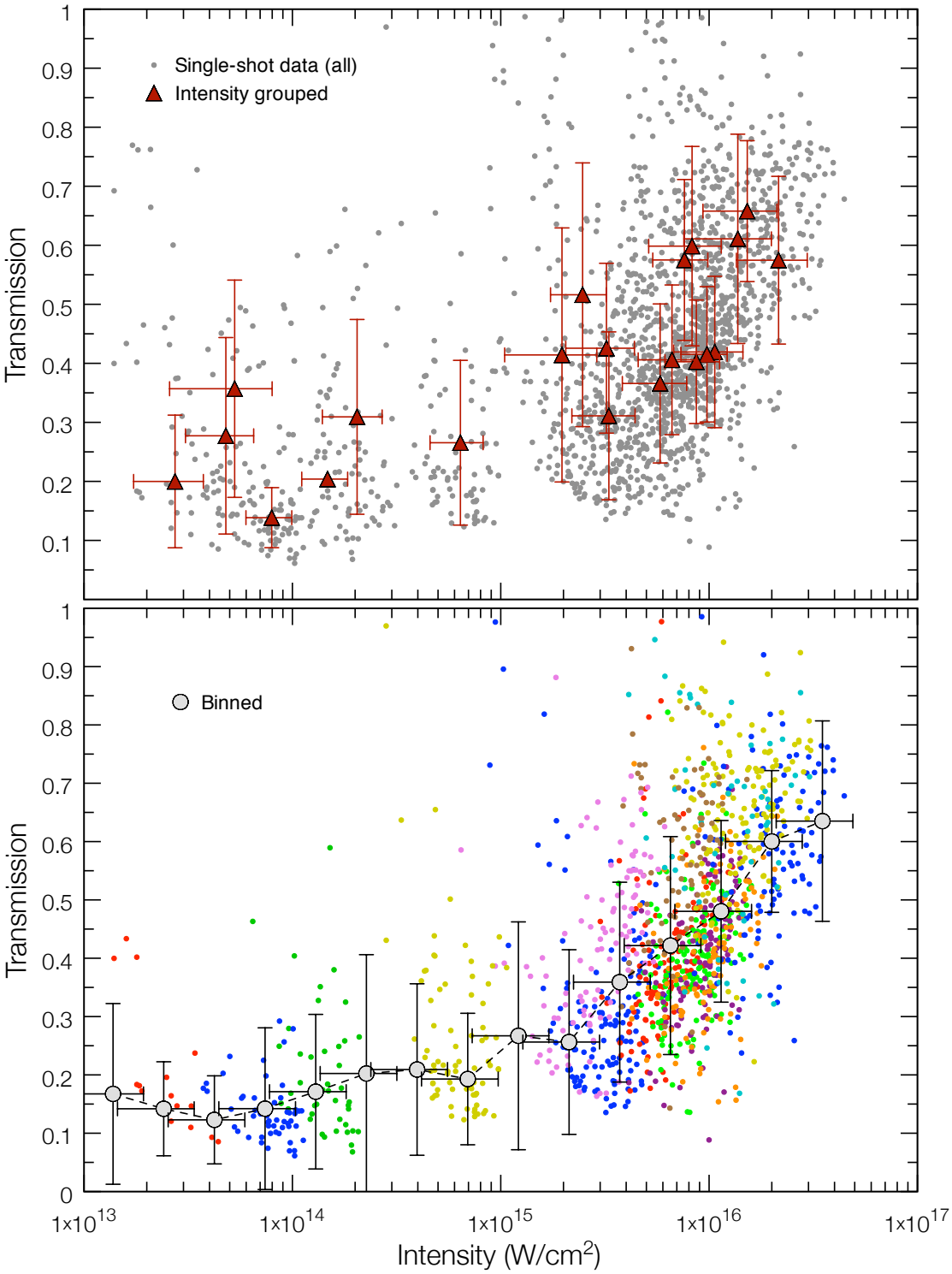

Figure 4.12: Transmission as a function of intensity in the Al-Mg-Al sandwich sample. Top plot shows all single shots (above a set pulse energy and diode signal threshold, in grey) and the average transmission value for a given position in focus (red). Bottom plot shows the single shot results after a selective filtering (colours indicate the focal position) and the corresponding binned results in intensity. See text for further details.

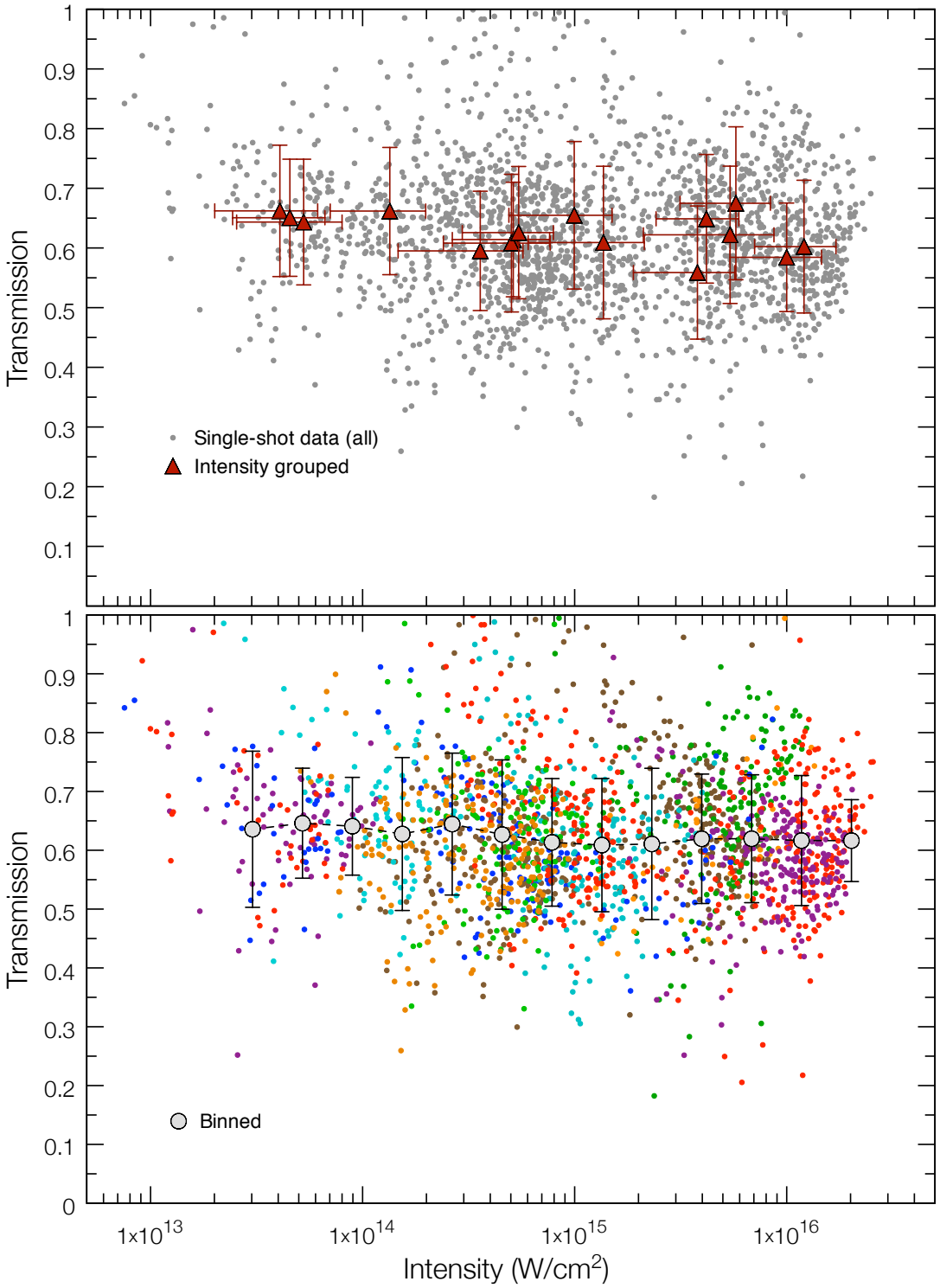

Figure 4.13: Transmission as a function of intensity in SiN. Top plot shows all single shots (above a set pulse energy and diode signal threshold, in grey) and the average transmission value for a given position in focus (red). Bottom plot shows the single shot results after a selective filtering (colours indicate the focal position) and the corresponding binned results in intensity. See text for further details.

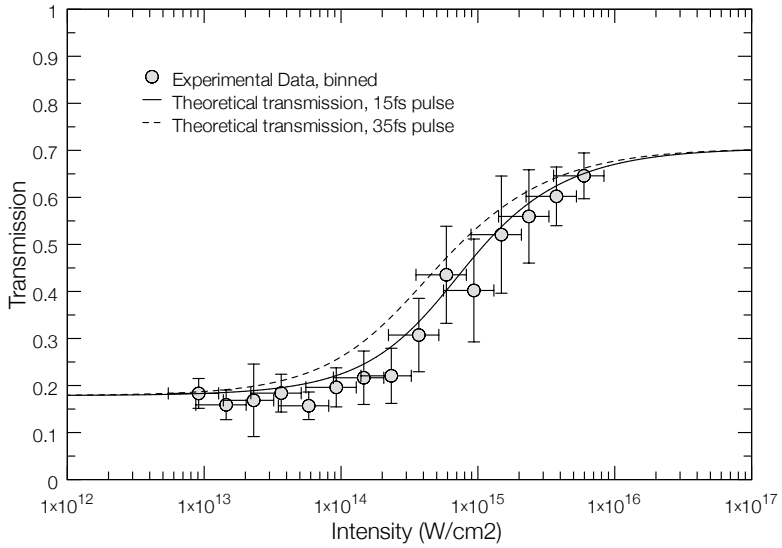

Figure 4.14: Saturable absorption in Al. The coloured region indicates the theoretical transmission spectrum following the simple model outlined, with Auger rates between 20 and 40 fs for the Al $2p$ recombination. The red line is the theoretical curve published in [29], which considers a full rate equation model.

intensities.

It is interesting to note at this point that for both Al and Mg, the theoretical curves predict saturation at slightly lower intensities than measured. This could be due either to an underestimation of the number of photons needed to produce a given number of core holes, or to an overestimation of the experimental intensity. Both these points can be understood by considering the spatial profile of the FLASH beam. As shown by imprints in PMMA in Fig. 3.6, the beam out of focus cannot be considered to be Gaussian as the profile contains several high intensity spikes situated on a larger, low intensity background. This holds both spatially and temporally. Since the saturation of absorption will only be driven by the photons in the spike where the highest intensity is achieved, the total fluence, or the total intensity, obtained by dividing the fluence by the generalized pulse length, can be a misleading quantity which is not directly linked to this process. However, given the randomness of the beam profiles from shot to shot due of the SASE scheme, this effect is very difficult to account for in an independent manner[5]. This peculiar pulse structure is the main uncertainty on the measured intensities, and is

[5]It could be argued that the difference between the measurement and the theory provides an indication of the amount of energy stored in the main peaked pulse, however, this is not an independent measurement, depending on the simulation of the saturable absorption process.

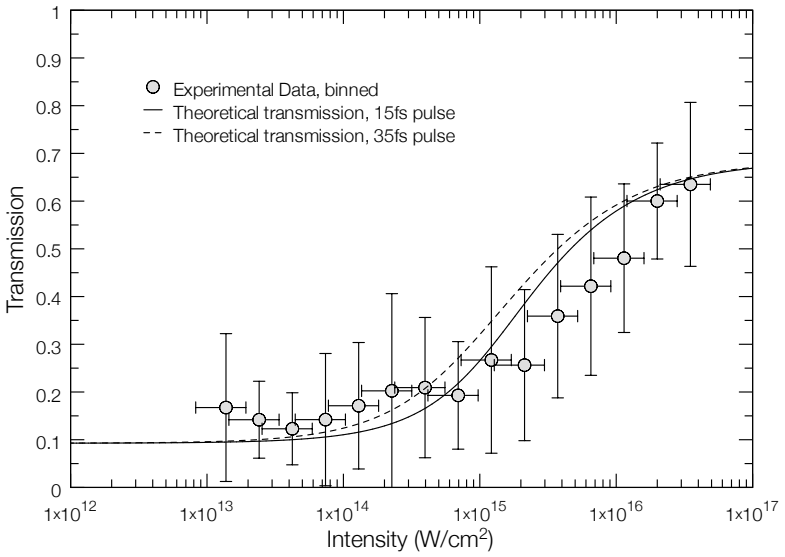

Figure 4.15: Saturable absorption in Mg. The coloured region indicates the theoretical transmission spectrum following the simple model outlined, with Auger rates between 20 and 40 fs for the Al core hole recombination, and half that for the combined recombination of the Mg core holes [104].

contained in the experimental errors in Figs 4.14 and 4.15. To provide some information on the dependence of the presented results to this uncertainty the theoretical calculations are presented for two different gaussian pulses, of 15 fs and 35 fs. In both cases the pulse fluence is the same.

The time over which the sample remains saturated depends on the recombination time of the transition of interest. For Al, this is about 40 fs, which is very short compared both to the time needed for electron-ion relaxation and to the time scale of ion movement. The temperature equilibration between electrons and ions occurs on the picosecond time scale [105], so it is reasonable to assume the ions to still be at room temperature. This assumption is confirmed by soft x-ray emission spectroscopy, which will be discussed in the following chapter. Even considering the Al nuclei having a kinetic energy of 1 eV, in 40 fs the distance traveled would only be about 1.5 Å, a fraction of the lattice spacing. As such, the saturable absorption effect, which takes place within the duration of the FEL pulse, is a purely electronic feature and no change in the transmission could have occurred due to ion movement.

Given this ultra-fast time response, the material undergoing saturable absorption becomes a rather efficient femtosecond light switch. The opaque–transparent–opaque

sequence takes place in Al in only around 40 fs and is independent of the intensity, provided it is sufficient to saturate and the excitation pulse length is short. The pulse length and the recombination time are strongly entwined in this process so if one is known, an appropriately designed experiment could offer the possibility to measure the other. Further, the saturation effect could be used to increase contrast on the XUV or x-ray pulse and potentially also shorten it to its diffraction limit.

Saturable absorption has, importantly, far reaching consequences to the field of WDM research, which is troubled by the experimental difficulty of creating thermodynamically homogeneous, finite-temperature and solid density samples. Although FEL light sources in the XUV and x-ray regime provide a large improvement over conventional optical lasers in terms of target heating due to the larger penetration depth, the absorption of light remains an exponential function of target thickness. For a saturable absorber this is not the case, because as the first layers of the sample become transparent due to the saturation of the main absorption channel, the penetration of the radiation increases and more energy is deposited deeper into the sample. Within the saturated region, the decrease in energy within the target is not exponential but linear, and much more homogeneous samples can be created. Alternatively, thicker samples can be used. An example of this effect is shown in Fig. 4.16, where the energy deposition, and hence the electron temperature, is shown for two samples, one in the linear absorption and the other in the saturated absorption regime. An estimated order of magnitude more homogeneous sample of the same thickness, or alternatively, an order of magnitude thicker sample with comparable temperature gradient, can be created by following this scheme. The practical applicability of this result seems quite universal. Indeed, virtually any sample of interest can be heated within the saturable absorption regime by matching the photon energy to a particularly well suited, strongly absorbing, core state, and selecting the appropriate intensity and sample thickness. The tunability and high peak brightness of current and future x-ray FELs, such as LCLS, SCSS and XFEL, make them therefore a unique and invaluable tool for the investigation of WDM.

The absorption results are supported by a rather extensive set of spectroscopic measurements. Shortly after the core states are excited, recombination takes place with electrons from the valence band filling the core holes. Such recombination is both radiative, where a photon is emitted, and non-radiative, dominated by the Auger effect. Although the Auger effect, which scales with the atomic number, accounts for most of the recombination, a sufficient number of core holes is created so that the fluorescence signal can be collected with an XUV spectrometer. These measurements provide a rich data set of information about the sample on the recombination time scales and provide support

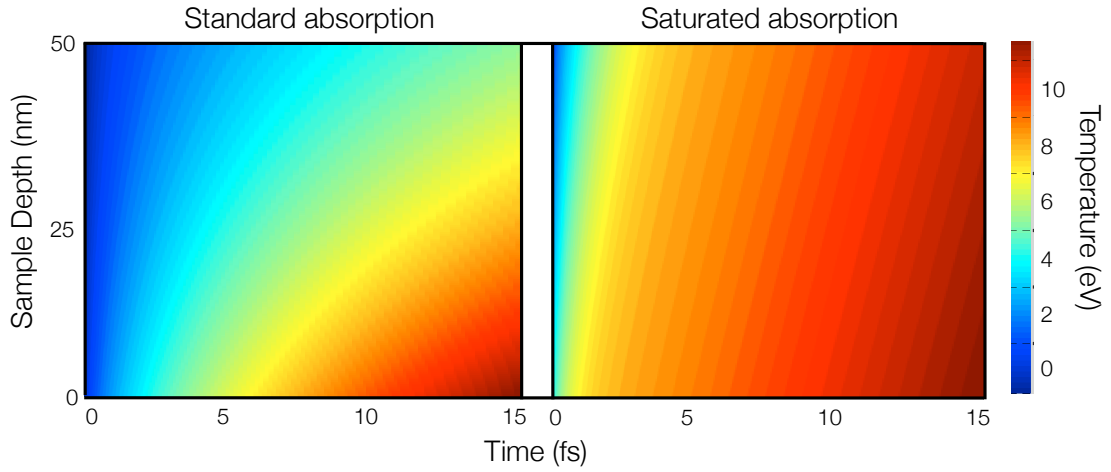

Figure 4.16: Homogeneous creation of WDM through saturated absorption. A 15 fs pulse is propagated through a 50 nm think Al foil with and without saturated absorption. The electron temperature is computed considering the volumetric energy deposition. At the end of the pulse the temperature gradient on the z-axis is seen to be much smaller is saturation of the absorption channel is possible. Calculation courtesy of Dr. B. Nagler.

to our claims that homogeneous WDM is created in the process. The next chapter is dedicated to the study of the XUV spectra, and the extraction of information, which affords the potential to elucidate details on the high-intensity absorption process, on the electronic structure of strongly photo-excited systems and on its subsequent evolution into the WDM state.

CHAPTER 5

Electronic Structure of a Photo-generated Aluminium Plasma

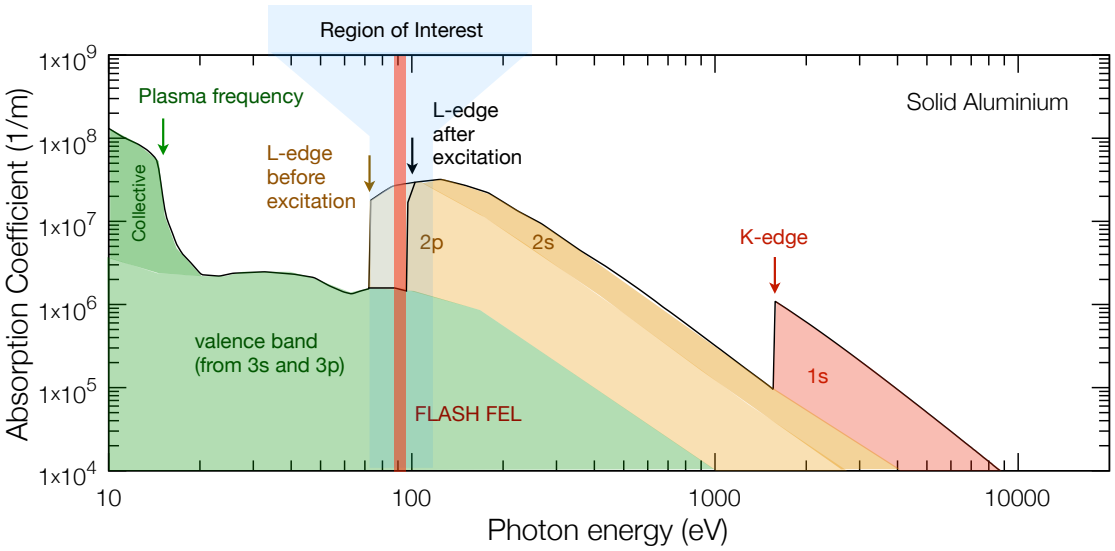

5.1 Introduction

Free-electron laser high-intensity XUV radiation is proving to be an invaluable tool in the field of high energy-density physics. As was shown in the previous chapter, very efficient mechanisms of sample heating on ultra-short time scales can be employed, which allow for the creation of strongly ionized, yet crystalline, solid density systems. While this is a very promising way to address the elusive goal of controlled creation of homogeneous warm dense matter, a major issue remains—the accurate experimental measurement of its physical properties. Of crucial importance are naturally the temperature and density of the sample, but other parameters are also of significant interest. These include the ionization state, ion and electron correlation functions, energy band gaps, as well as other properties pertaining to the electron and ion subsystems.

One of the more promising techniques in this regard is x-ray Thomson scattering. This is an extension of the classical scattering of light by charged particles[1] into the XUV and x-ray regimes, which, due to the larger penetration depth of light at these wavelengths, is an adequate probe for dense systems. By measuring the scattered light, information on the electron density and temperature, on the ionisation state, collisional rates and structure factors may in principle be obtained [106, 107, 108]. That this is also experimentally viable has been successfully verified for several systems such as warm-dense lithium [109], shock-compressed plastic [110], and warm-dense hydrogen [111]. The adaptation of this probing technique to FEL light sources, in particular LCLS, is a very active and intriguing area of current research.

There is however another direction that may be taken for probing the properties of warm-dense solids, which is soft x-ray emission spectroscopy (XES). XES yields in some aspects similar and in other aspects complementary information to that obtained through x-ray Thomson scattering, as it provides information about transitions between electronic states and maps the local structure. Traditionally, emission spectroscopy in low-density plasma physics encompasses the spectrum covering all wavelengths from the optical to the x-ray regime consisting of plasma line emission. Within certain limitations these spectra, both in absorption and in emission, are invaluable for measuring the basic plasma parameters in terms of line configurations, intensity ratios and linewidths. In this chapter we will investigate a very specific XES process: the fluorescence emission produced by electron transitions between the valence band and the L-shell, of a low-Z

[1] This nomenclature can trace its origin to the use of optical Thomson scattering for probing under-dense plasmas; in the x-ray regime this process would usually be referred to as Compton scattering. When referring to x-ray Thomson scattering in the following, I am considering both the elastic and inelastic scattering of free and bound electrons.

metal, Al, at solid density. As will be discussed, the physical parameters of this system are such that it is possible to measure on ultra-fast time scales and in a very simple manner the valence electron density and temperature. It is worth noting that a part of the electron density of states is directly mapped[2] by XES, so that in addition to the standard density and temperature we also gain insight on the electron distribution, the band structure, the ion structure and on the ionization.

In this Chapter I will present the first measurements of the valence band structure immediately after the absorption of the FLASH excitation pulse, give a detailed description of the steps taken to interpret this data and discuss the information that can be extracted. This study also sheds light on the absorption process of high-intensity XUV radiation in solids and complements the experimental observation of saturable absorption in the XUV, as described in the previous Chapter. Importantly, it also shows promise as a method to measure the electronic structure of a strongly photo-excited system as it evolves into the warm-dense matter state in a time resolved fashion, provided a pump-probe experimental measurement is conducted.

5.2 Theory of soft x-ray emission

The soft x-ray or XUV emission from a sample is the light that is emitted due to a radiative recombination process, where an atomic core hole is filled by an electron originating from some higher electronic state. Naturally, also non-radiative processes such as Auger recombination can occur, in which case no radiation is emitted. Atomically, the final state of the Auger process includes an electron emitted into the continuum. This in principle holds also in the case of a solid, however the electron cross section is relatively high and only those electrons emitted from a very thin surface layer actually escape the sample. For volumetric excitation, as is usually the case when soft x-rays are used to created the initial state with core holes, the majority of the energetic electrons created by Auger recombination are confined to the sample and the energy that is released from the core-hole recombination is eventually ceded to the valence band through electron collisional thermalization. The time scale on which this occurs is of significant importance for high energy-density research, since for low Z materials this is the dominating heating mechanism, as I will illustrate shortly.

Radiative and Auger recombination are competing processes and their importance varies throughout the periodic table as a function of the atomic number Z. For low

[2]This is due to angular momentum selection rules. The full DOS can be extracted from the data if a combined measurement of K and L-shell recombination is made.

Z, Auger is the dominant recombination process, whereas for high Z radiative emission prevails. In our experiments we have studied Al, for which $Z = 13$. The particular emission channel that we are interested in is that of the filling of a single core hole created in the $2p$ state, that is under normal conditions fully occupied with six electrons per atom. Compared to Auger recombination, radiative emission for this channel in Al is very weak, accounting for only about 0.24 % of the total recombination [101].

5.2.1 Density of states

The density of states $\rho(E)$ of a system (DOS) which is described by the Schrödinger equation

$$\mathcal{H}\varphi_n = \varepsilon_n \varphi_n, \tag{5.1}$$

where $\mathcal{H}$ is the Hamiltonian operator, φ_n its eigenfunction corresponding to a certain energy band n and ε_n the respective eigenvalue, is defined by the following expression:

$$\rho(E) = \sum_n \langle \varphi_n | \varphi_n \rangle \delta(E - \varepsilon_n). \tag{5.2}$$

Consider a complete set of functions that satisfy the closure relation

$$\sum_i |\psi_i\rangle\langle\psi_i| = \mathbf{1}. \tag{5.3}$$

This set can be used as a basis on which the eigenfunctions may be projected. We can then re-write the DOS in the form

$$\rho(E) = \sum_i \sum_n \langle \varphi_n | \psi_i \rangle \langle \psi_i | \varphi_n \rangle \delta(E - \varepsilon_n) \tag{5.4}$$

$$= \sum_i \rho_i(E), \tag{5.5}$$

where $\rho_i(E)$ is the projected DOS (pDOS), given by

$$\rho_i(E) = \sum_n |\langle \psi_i | \varphi_n \rangle|^2 \, \delta(E - \varepsilon_n). \tag{5.6}$$

Of particular interest is the case where $\{|\psi_i\rangle\}$ is the set of spherical harmonics as we may then decompose the DOS based on angular momenta. Another set of interest is that where the basis is chosen to be complete in real-space, normalised within a given sphere centred on a particular atom. Then, $\rho_i(E)$ represents the local DOS, with the index i

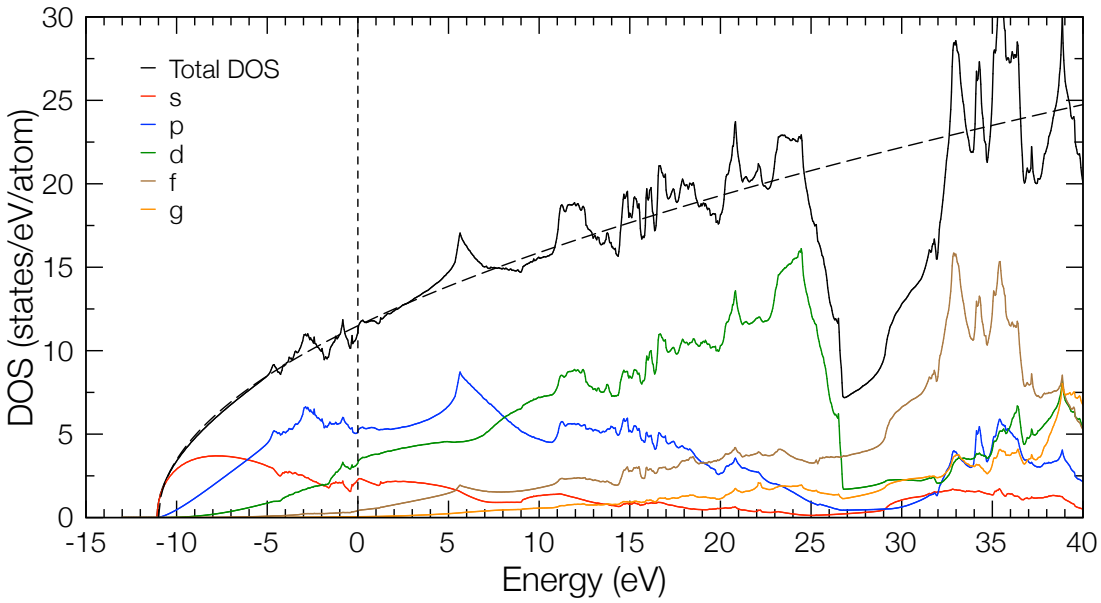

Figure 5.1: Projected density of states of Al. The Fermi edge is set to 0 eV so the occupied states at T=0 are at negative energies. Up to 25 eV, where a band gap opens between the d and f components, the system is well approximated by the free-electron DOS curve following the typical $\sqrt{E}$ dependence. Calculation performed with the *Abinit* code, 1 atom/cell, in the GGA approximation with 3 electrons in the valence.

indicating the atom around which the DOS is projected. An example of the DOS and pDOS can be seen for Al in Fig. 5.1.

5.2.2 Emission spectrum

The total power emitted by a single radiator, averaged over all directions and polarisations, in the energy range $E + dE$ is given by the expression [112]:

$$I_0(E) = \frac{4e^2hE^2}{3m_e^2c^3}|M_{if}|^2, \tag{5.7}$$

where E is the quantum of energy in the radiated photon and M_{if} the transition matrix between the initial states φ_i and the final states φ_f:

$$M_{if} = \langle\varphi_i|\nabla_{\mathbf{r}}|\varphi_f\rangle. \tag{5.8}$$

For the emission process of interest, where the transition takes place from the dense set of Al valence band levels $|\varphi_n\rangle$ of band index n, to a sharp inner core $2p$ level $|\psi_{2\mathrm{p}}\rangle$, this expression must account for the density of states in the valence band, as given by Eq. (5.2), yielding

$$I(E) = \frac{4ne^2h}{3m_e^2c^3}E^2 \sum_n |\langle\psi_{\mathrm{core}}|\nabla_{\mathbf{r}}|\varphi_n\rangle|^2\delta(E - E_{2\mathrm{p}} + \varepsilon_n), \tag{5.9}$$

where n is the radiator density. By comparing Eqs. (5.6) and (5.9) we notice a similarity in the expressions, both in terms of the angularly-projected and of the local DOS, since the core wave functions have well-defined angular symmetry and are spatially confined to a small region around the atoms. Indeed, considering the dipole selection rules for the transition in question the emission can be approximated reasonably well by the angularly projected DOS.

The result in Eq. (5.9) holds for a single particle transition. While this succeeds in representing the majority of the effect, it is not a complete description of the transition, as several other effects come into play. The simplest to account for is the effect of level broadening due to finite core-hole lifetimes. Indeed, the sharp energy levels that appear in Eq. (5.9) are in principle only valid if the states participating in the process are long-lived. For the core-hole, $E_{2\mathrm{p}}$, this trivially does not hold and an energy broadening due to the time-energy uncertainty principle is introduced. In the valence band electron-electron interactions cause a similar effect as they limit the lifetime of the electronic states. Another important effect which is promptly observed experimentally is that due to semi-Auger transitions. Illustrated in Fig. 5.2(b), this is a two-body transition where the primary electron fills the core hole and one part of the energy from this relaxation is used to excite a secondary electron, while the other part is emitted as a photon. As a result, the bandwidth of the emission doubles in size. These effects can be rather tedious to include in full and a discussion of the details this would involve is outside the scope of this discussion. It is nevertheless beneficial to illustrate in a simplified way what the contributions of such effects are on the final emission spectrum. For this we use a simple one-parameter empirical broadening model as initially introduced by Landsberg [113]. In this scheme, the global effect of all interactions and finite core-hole life times is described by an energy-depended broadening function for the initial and

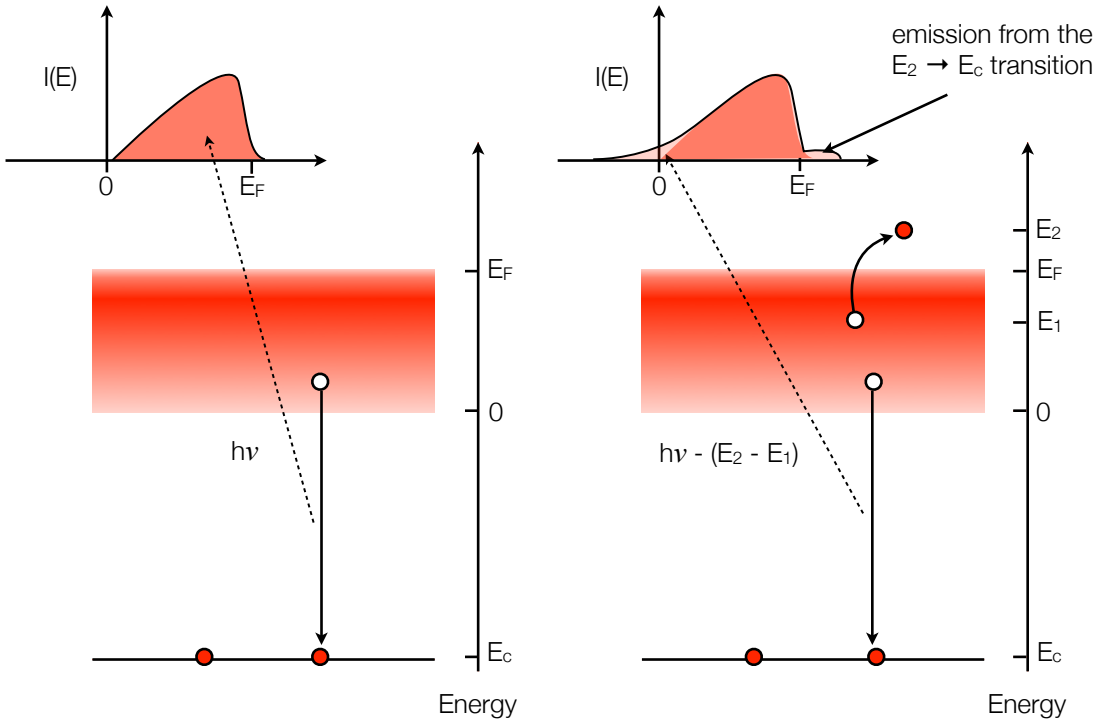

(a) one-body transition

(b) two-body transition

Figure 5.2: Semi-Auger contribution to the emission spectrum. In a) the one-body recombination is shown which maps the available density of states from the valence band. The contribution due to two-body recombination is shown in b), which adds a tail to the emitted spectrum of the primary electron recombination, as part of the energy that would otherwise go to the photon is used to excite a secondary electron.

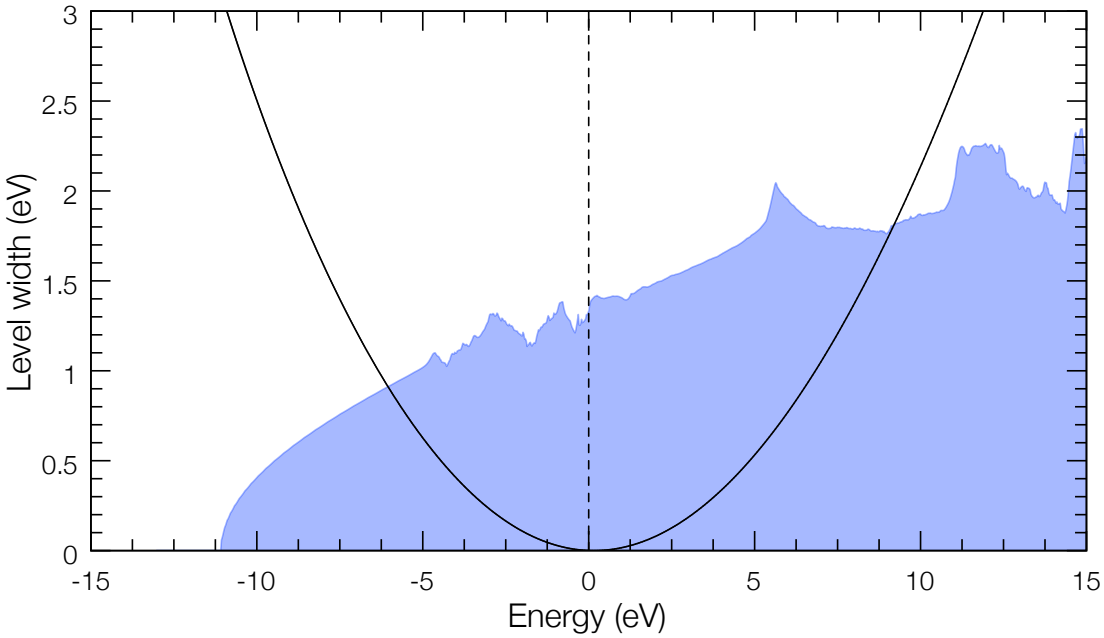

Figure 5.3: Valence band level widths according to Eq. (5.11). In blue the valence density of states for Al. The Fermi level is set to 0, with occupied bands at negative energies.

final states of the transition [114]:

$$\Delta(E) = E_F \Bigg\{ \left(\frac{k}{\lambda} - \frac{3\lambda}{4k} \right) \arctan \left(\frac{2k}{\lambda} \frac{k_F^2 - k^2}{k_F^2 + 3k^2 + \lambda^2} \right) + \frac{k_F^2 - k^2}{2\lambda^2} \left(\frac{k_F^2 - k^2}{2k\lambda} \arctan \frac{2k\lambda}{k_F^2 - k^2 + \lambda^2} - 1 \right) + \ln \frac{(k_F^2 - k^2)^2 + 2\lambda^2(k_F^2 + k^2) + \lambda^4}{4\lambda^2 k^2 + \lambda^4} \Bigg\}. \tag{5.10}$$

This line broadening is shown as a function of energy in Fig. 5.3. The effect of this broadening is zero at the Fermi level and increases with decreasing (and increasing) energy. The level-broadened DOS that is used to estimate the emission spectrum from Eq. (5.9) can then be calculated according to the expression:

$$\tilde{\rho}(E) = \frac{1}{2\pi} \int \frac{\Delta(E')\rho(E')}{(E - E')^2 + (\Delta(E')/2)^2} dE', \tag{5.11}$$

where $\rho(E')$ is the non-broadened DOS.

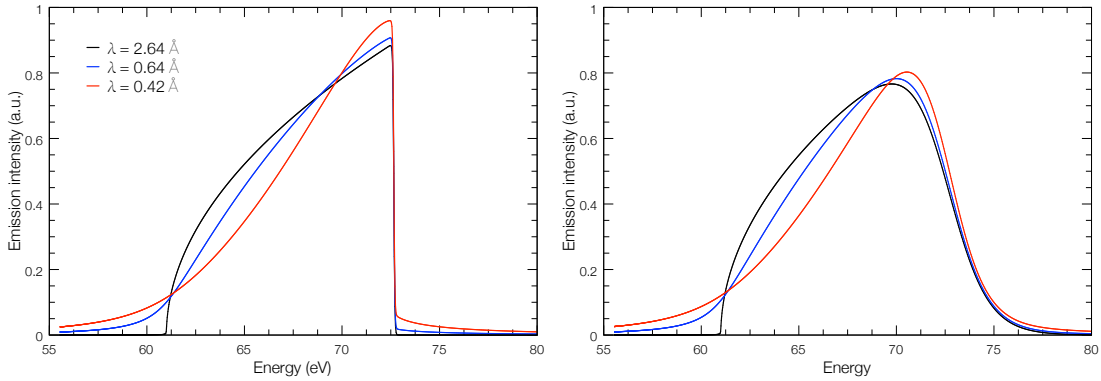

(a) $T_e = 300$ K (b) $T_e = 1.0$ eV

Figure 5.4: Effect of the Landsberg level broadening on the emission spectrum, here shown as a function of the broadening parameter λ and the electron temperature T_e, for a simple $\sqrt{E}$ emission model.

5.3 Soft x-ray emission spectroscopy at FLASH

The experimental aim is to measure the soft x-ray emission spectra (XES) of the $L_{2,3}$ core-hole recombination in aluminium over a large range of FEL radiation intensities. In principle this technique affords the potential of measuring the electronic properties of the Al sample such as temperature and density, since the transition maps the valence band onto the $2p$ core state. The opportunity to measure the electronic structure of a system as it evolves from the solid to a plasma state is one of great practical interest as accurate probing of solid-density and near-solid-density systems is notoriously difficult. The advent of high-brilliance FEL sources in the XUV and x-ray regime now enable us to conduct such measurements on femtosecond time scales. We are naturally interested in particular in the novel high-intensity regime, as it is there where we expect a deviation from the standard Al L-shell XES, which has been widely investigated precedently [115, 116, 117, 118, 119]. The experimental results pertaining to this chapter were obtained on the FLASH free-electron laser operating at 13.5 nm (92 eV). The relevant characteristics of FLASH have been described in Section 3.2.

5.3.1 Experimental Setup

Two separate experimental setups were used to collect the emission data. This was done to cover the largest possible range of intensities - of over three orders of magnitude - as will be shown in the following. The results at lower intensity were obtained on FLASH

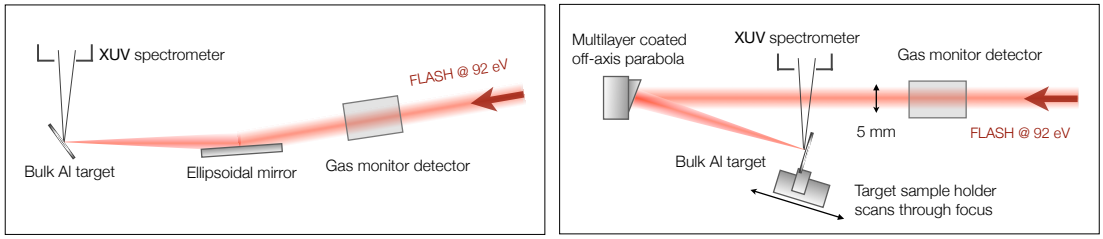

(a) Beam line BL2

(b) Beam line BL3

Figure 5.5: Focusing and spectrometer setup for soft x-ray emission spectroscopy. All other experimental details are the same as those described in Chapter 3 and illustrated in Fig. 3.4.

beam line BL2, on the Thompson scattering experimental chamber [3]. Higher intensities were generated and used on the FLASH microfocusing beam line BL3. Both the microfocusing setup and the spot size characterization used to calculate the intensities reached are described in detail in Chapter 3. Apart from a few important differences, the two experimental setups are very similar. A schematic representation for both is given in Fig. 5.5. In the first setup on beam line BL2, the beam focusing was provided by an ellipsoidal mirror and the laser spot size was kept constant on target at 20×30 μm^2. A gas attenuator in the beam was used to attenuate the total energy of the pulse delivered on target, which was between 1-50 μJ. Considering an average pulse length of $\sim$35 fs (as discussed in Section 3.2), this corresponds to an intensity range of $(5 \times 10^{12} - 2 \times 10^{14})$ Wcm^{-2}. The microfocusing capabilities that we developed on beam line BL3 gave us the opportunity to reach even higher intensities. In this setup, the target was moved with respect to the best focusing position of the off-axis parabola (OAP), which provided a range of effective spot sizes between 1-10 μm. Although the gas attenuator was not used in this setup, a range of energies of about 1-10 μJ was delivered on target, primally due to variable FEL operation. This is also the main reason for the generally lower energy delivery on BL3 compared to BL2. A 3 mm pinhole was placed upstream in the beam to improve the pulse wavefront on the OAP. The wavefront quality is of relevance to the focusing of the 13.5 nm radiation to micron and sub-micron spot sizes (see Chapter 3 for discussion). The achievable range of intensities on this experimental setup is therefore $(3 \times 10^{13} - 3 \times 10^{16})$ Wcm^{-2}. In both setups the total energy within the beam was monitored on a shot-to-shot basis by means of a gas monitor detector [19].

[3] Some additional details on the setup may be found in [111] and references therein.

5.3.2 Spectroscopy

The target for the spectroscopy measurements is pure, bulk Al, with a surface oxide layer estimated to be about 10 nm thick. Given the penetration depth of the FEL radiation, the emission will be mainly volumetric and the overall contribution of the oxide layer negligible. Indeed, the emission spectrum of Al_2O_3 [120] is not present in the measurements that will be discussed. Nevertheless some spectra obtained on BL3 do show features that could be associated to the emission from Al_2O_3. This is most probably due to an alignment close to grazing incidence of the spectrometer so that a larger amount of the surface is sampled compared to the bulk. Although these results are not used in the following discussion, they show that such features are simple to discriminate against.

The emission was recorded using the high-throughput XUV spectrometer HiTRaX. It features a toroidal focusing mirror and a variable line space reflection grating, with a spectral range of 5-35 nm and a maximum resolution of $\lambda/\Delta\lambda = 220$ at 13.5 nm. Further details of the spectrometer can be found in [121]. For each recorded spectrum the exposure time was between 10-60 s, depending somewhat on the incoming pulse energy, so as to accumulate a similar amount of fluorescence photons each time. The pulse rate used is 5 Hz which is delivered to a continuously moving target sample so that a fresh portion is irradiated at each shot. This is to avoid that multiple shots create a crater in the sample, which would have two main drawbacks: the interaction region shifts, defocusing the spectrometer, and the photons are deposited deeper in the crater so that the emission at an angle off the normal is affected stronger by reabsorption.

5.4 Density functional theory and the projector augmented wave method

From Eq. (5.9) it is clear that in order to calculate the emission spectrum from first principles, both the wave functions and energies of all electrons, core and valence, are needed. For this purpose, the electronic structure of Al will be computed for a range of systems using the finite-temperature density functional theory (FT-DFT) approach [26], as implemented in the *Abinit* code[4] [122, 123, 124, 125, 126]. This is a plane wave code adequate for describing dense and solid systems, and is optimized to use projector aug-

[4]The *Abinit* code is a common project of the Université Catholique de Louvain, Corning Incorporated, the Université de Liège, the Commissariat à l'Energie Atomique, Mitsubishi Chemical Corp., the Ecole Polytechnique Palaiseau and other contributors.

mented wave potentials (PAW). The ionic structure is computed in turn using classical molecular dynamics.

PAW potentials

It is common practice to separate the core and valence electrons in DFT calculations. This is computationally convenient because the bonding in the solid state originates only from the behaviour of the relatively small number of valence electrons. Most of the electrons lie in core states but provided they are reasonably far in energy from the valence band, these states do not change based on the chemical environment surrounding the atom. The core states and energies can therefore be calculated to good approximation considering a single isolated atom and need not be re-evaluated when the atoms are placed together to form a solid. The valence electron states on the other hand are different in the solid compared to the states the electrons would occupy in a single atom and are fully dealt with in the representative DFT calculation. This method of disregarding the core contributions when treating the valence is referred to as the *frozen core approximation*. The core however is still important as it screens the nucleus and due to the Pauli exclusion principle sets constraints, such as orthogonality, on the valence wave functions close to the nucleus. This translates into valence wave functions that are highly oscillatory in this region, which poses problems to codes that use a plane wave basis set [127].

A standard way of dealing with this issue is to use an effective pseudopotential to describe the real potential of a nucleus. The pseudopotential is equal to the real potential in the region where bonding takes place but is modified for positions very close to the nucleus so as to produce smooth wave functions for the valence electrons. This results in a far more efficient and accurate plane wave decomposition of the wave function and consequentially, a more efficient calculation of the DFT ground state. The price to pay is that the information on the electron charge density close to the nucleus is lost. Alternatively, instead of using a plane wave bases set in the core region, atomic-like partial waves can be used. Outside this region a set of envelope functions can then be used to account for the bonding. This is the augmented wave method, and the solutions from different spatial regions are matched at the core boundary.

The PAW method, initially proposed by Blöchl [128], generalizes these two approaches by creating pseudopotentials that are soft inside the core, with the respective wave functions smooth, enabling an efficient plane wave decomposition, but still retaining full information of the valence density close to the nucleus. Although a rigorous

theoretical description of the PAW method is beyond the scope of this discussion, I will introduce it briefly, as some aspects will be of importance in the following when I discuss the construction of PAW potentials for photo-excited matter. I will closely follow the discussion presented in references [127, 129].

The standard problem in DFT is to solve the Schrödinger-like Kohn-Sham equation

$$\left(-\frac{\hbar^2}{2m_e}\nabla^2 + V_{\mathrm{KS}}\right)|\psi_n\rangle = \epsilon_n|\psi_n\rangle, \tag{5.12}$$

which through the Kohn-Sham potential V_{KS} maps the interacting many-electron system onto a fictitious non-interacting single particle system, simpler to solve, yet yielding the same electron density

$$\rho(\mathbf{r}) = \sum_n |\langle \mathbf{r}|\psi_n\rangle|^2. \tag{5.13}$$

The solution is found in a self-consistent manner by minimizing the total energy of the system, which is a functional of the density:

$$E[\rho] = K[\rho] + V_{\mathrm{ext}}[\rho] + V_{\mathrm{H}}[\rho] + V_{\mathrm{XC}}[\rho]. \tag{5.14}$$

Here $K[\rho]$ indicates the kinetic energy, $V_{\mathrm{ext}}[\rho]$ the potential due to the ions (and also any other contribution that is external to the electron system), $V_{\mathrm{H}}[\rho]$ the direct Coulomb (Hartree) energy and $V_{\mathrm{XC}}[\rho]$ the energy contribution due to Coulomb exchange and to correlation effects. This energy minimization is constrained through Lagrange multipliers which insure that the single particle wave functions are orthogonal. The various pseudopotential approaches are designed to tackle the V's in Eq. (5.14). The aim is to modify them in some way so that the resulting solutions to Eq. (5.12), the wave functions, $\psi_n(\mathbf{r}) = \langle \mathbf{r}|\psi_n\rangle$, are smoothened in the regions close to the nuclei, making the plane wave decomposition more efficient and decreasing the amount of time needed to minimize $E[\rho]$.

The basis of the PAW method is the search for a linear transformation $\mathcal{T}$ that links the all-electron wave functions $|\psi_n\rangle$ to an auxiliary set of wave functions $|\tilde{\psi}_n\rangle$, which are numerically convenient for expansion in plane waves

$$|\psi_n\rangle = \mathcal{T}|\tilde{\psi}_n\rangle. \tag{5.15}$$

Far from the core $|\psi_n\rangle$ is smooth and therefore satisfies this requirement, so for this region of space no modification is needed. Close to the core however, in the augmentation spheres, $\mathcal{T}$ must transform the auxiliary smooth function into the correct all-electron

form with the full nodal structure. Based on these requirements, the transformation is given in the form

$$\mathcal{T} = 1 + \sum_r \mathcal{S}_r, \tag{5.16}$$

where the index r runs over all atomic sites. As $\mathcal{S}$ necessarily contains atomic-like wave function information it is convenient to define it in terms of partial wave solutions to the Schrödinger equation for an isolated atom $|\phi_i\rangle$. Within the augmentation sphere of radius r_c the real wave function can be expanded on this basis as:

$$|\psi_n\rangle = \sum_i c_i |\phi_i\rangle, \quad r < r_c \tag{5.17}$$

with the coefficients c_i. Auxiliary partial waves are then defined, for each atomic site, by

$$|\phi_i\rangle = (1 + \mathcal{S})|\tilde{\phi}_i\rangle, \tag{5.18}$$

and this transformed set of partial waves is used to decompose the auxiliary wave function within the augmentation sphere, which by construction must have the same expansion coefficients as the all-electron wave function given in Eq. (5.17):

$$\begin{aligned} |\tilde{\psi}_n\rangle &= \sum_i \langle \tilde{p}_i | \tilde{\psi}_n \rangle |\tilde{\phi}_i\rangle \quad r < r_c \\ &= \sum_i c_i |\tilde{\phi}_i\rangle, \end{aligned} \tag{5.19}$$

which defines the projector functions $|\tilde{p}_i\rangle$, which are closely tied to the auxiliary partial wave functions

$$\sum_i |\tilde{\phi}_i\rangle\langle\tilde{p}_i| = 1, \quad r < r_c \tag{5.20}$$

$$\langle \tilde{p}_i | \tilde{\phi}_j \rangle = \delta_{ij}. \tag{5.21}$$

It follows that

$$\mathcal{S}|\tilde{\psi}_n\rangle = \sum_i \mathcal{S}|\tilde{\phi}_i\rangle\langle\tilde{p}_i|\tilde{\psi}_n\rangle = \sum_i (|\phi_i\rangle - |\tilde{\phi}_i\rangle)\langle\tilde{p}_i|\tilde{\psi}_n\rangle, \tag{5.22}$$

and the transformation operator that links the all-electron wave function to the smooth

auxiliary wave function is given by

$$\mathcal{T} = 1 + \sum_i (|\phi_i\rangle - |\tilde{\phi}_i\rangle)\langle\tilde{p}_i|. \tag{5.23}$$

These three functions, needed for the PAW transformation, are illustrated in Fig. 5.6, for a basis of 6 functions and a core radius $r_c = 2.2$ bohr (1.16 Å). The expectation value of a given operator A on the valence states, i.e., the matrix elements, can now be calculated either from the auxiliary or from the reconstructed true wave function

$$\langle A\rangle = \sum_n f_n\langle\psi_n|A|\psi_n\rangle = \sum_n f_n\langle\tilde{\psi}_n|\mathcal{T}^\dagger A\mathcal{T}|\tilde{\psi}_n\rangle, \tag{5.24}$$

where f_n indicates the occupation number of the valence state n. Importantly, since the valence wave functions obtained in this manner are formally correct in all space (which is not in general true for a pseudopotential DFT calculation), the calculation of matrix elements between core and valence states, which is required for the soft x-ray emission intensity, is straightforward. In this sense the PAW potentials are quite different from other pseudopotentials and are often called all-electron frozen-core potentials[5], since they contain the full information of the electronic structure near the nucleus through the projector functions.

5.4.1 PAW potentials for photo-excited matter

To study the electronic structure of Al under intense XUV radiation two types of Al atoms are needed: ground state Al, which describes both the structure of the emitting atom and that of an atom which has not been excited, and an atom with a core hole in the $2p$ state which represents a photo-excited atom. We propose to model this combined system by creating specific potentials to describe these two different kinds of atoms. As discussed earlier, the energy of 92 eV can only excite one core state per Al atom. If however the energy of the radiation is sufficiently high, several core hole state can be formed and each such state would in principle require a specific potential.

For this purpose we will use the *Atompaw* code [130], which constructs PAW potentials which can be ported simply into a format that can be used by *Abinit*. A PAW potential for ground state Al was built and tested against the several other PAW potentials that are available [131], and compared to known experimental results. The excited

[5]The frozen core approximation, although generally convenient, is not necessary for PAW potentials. It is however necessary for the creation of excited state potentials with the technique that I will illustrate in the following.

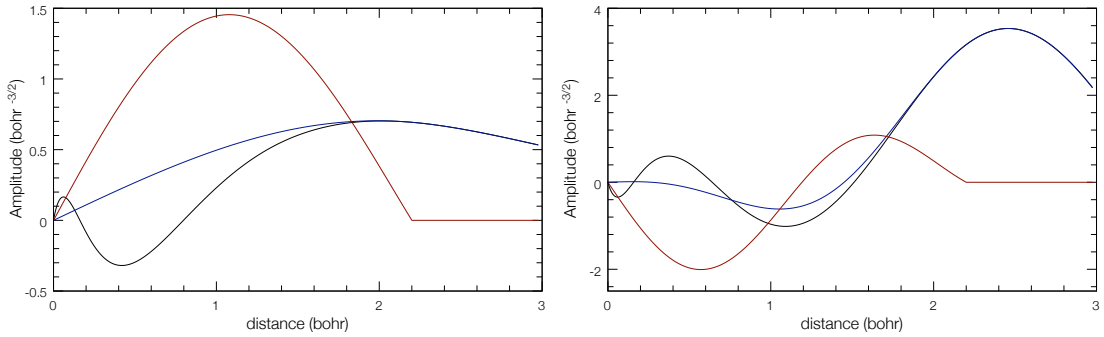

(a) s_1

(b) s_2

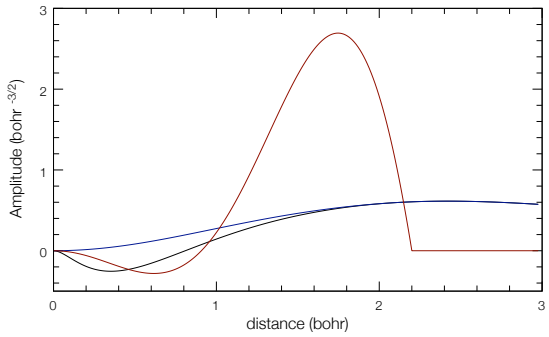

(c) p_1

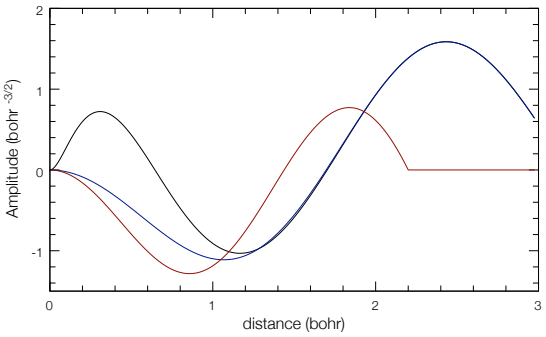

(d) p_2

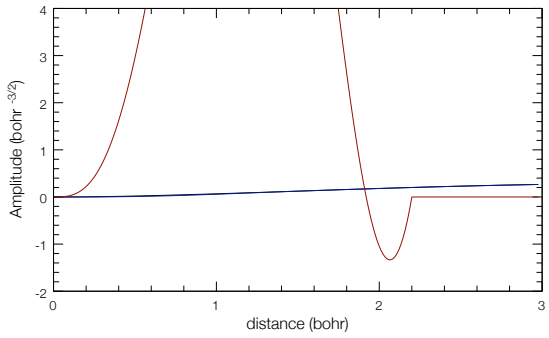

(e) d_1

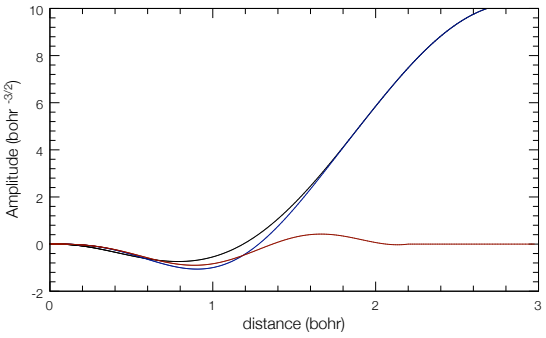

(f) d_2

Figure 5.6: PAW basis within the augmentation sphere ($r_c = 2.2$ bohr) for the valence electrons in ground state Al, containing two partial waves for the s, p and d orbitals. The all-electron partial wave functions $\phi_i(r)$ are shown in black, the auxiliary partial wave functions $\tilde{\phi}_i(r)$ in blue and the projectors $\tilde{p}_i(r)$ in red.

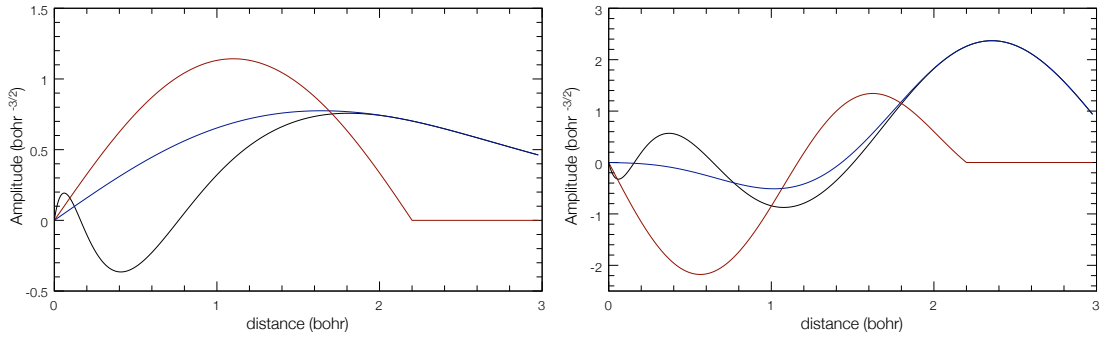

(a) s_1 (b) s_2

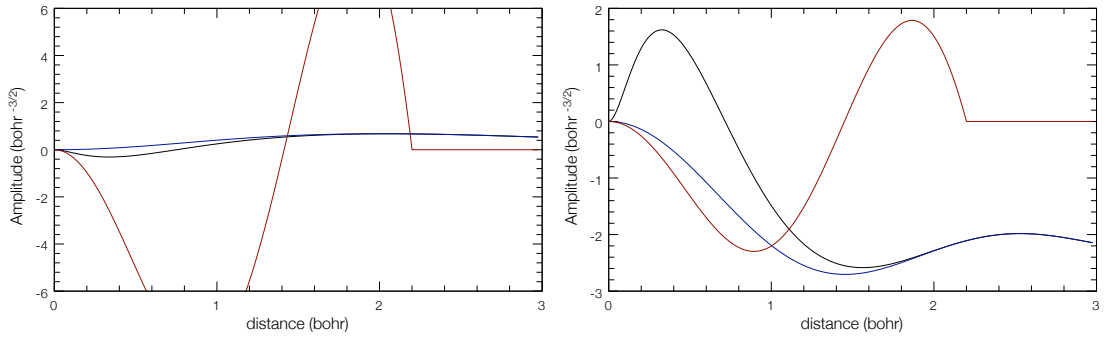

(c) p_1 (d) p_2

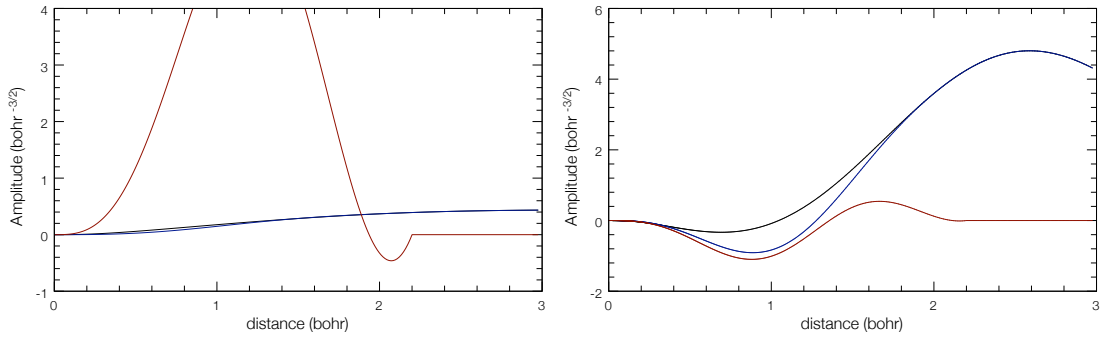

(e) d_1 (f) d_2

Figure 5.7: PAW basis within the augmentation sphere ($r_c = 2.2$ bohr) for the valence electrons in Al with a core hole in the $2p$ state, containing two partial waves for the s, p and d orbitals. The all-electron partial wave functions $\phi_i(r)$ are shown in black, the auxiliary partial wave functions $\tilde{\phi}_i(r)$ in blue and the projectors $\tilde{p}_i(r)$ in red.

potential was constructed starting from the ground state potential and modifying only those parameters which are influenced by the occupation of electronic states. This is the first step in ensuring the quality of the core hole potential, which is otherwise difficult to assess.

The electronic configuration of atomic Al is [Ne]$3s^2 3p^1$; in the solid the last three electronic shells merge into a valence band. The partial wave basis then requires a minimum of two functions - one for the s shell and one for the p shell. This proves to be insufficient to calculate accurately the atomic bound states so an additional partial wave is added for each angular momentum. In addition to this, we also explicitly add two d waves to add to the completeness of the basis set (formally completeness is assumed, see Eqs. (5.19) and (5.20); in practice the series is quickly converging making this technique computationally advantageous), which has now six partial waves. The electronic configurations used to construct the PAW potentials are then

$$\begin{aligned} \text{ground state} &\qquad 1s^2\ 2s^2\ 2p^6\ 3s^1\ 3p^1\ 3d^1 \\ \text{core hole} &\qquad 1s^2\ 2s^2\ 2p^5\ 3s^2\ 3p^1\ 3d^1, \end{aligned}$$

with the black states in the frozen core, and the red ones in the valence. Note that both of these states are excited[6]. For the first, this is only formally the case, since the frozen core is in the ground state and the valence electron states will be computed by a DFT calculation, which will yield the global ground state of the system regardless of the configuration used to construct the potential[7]. The partial wave basis for both potentials is shown in Figs. 5.6 and 5.7. As can be clearly seen from the cutoff in the projector functions, the augmentation sphere radius is $r_c = 2.2$ bohr (1.16 Å). The additional partial waves add to the complexity of the calculation and decrease performance, however the accuracy of the potential is improved. This was verified by comparing the pDOS for a solid-state Al system at high energies (above the Fermi energy) calculated with the PAW potential, to all-electron calculations.

Convergence efficiency and other properties are tested through a DFT calculation for a solid Al system, modelled by a primitive FCC cell. For both potentials, an energy cutoff of 430 eV is seen to be sufficient to converge the total energy to within about 1 meV. Using a test-bed 1-atom system, the k-point sampling necessary for similar energy convergence is a $10 \times 10 \times 10$ Monkhorst-Pack grid. Again, both potentials show

[6] Unfortunately is was not possible to create a ground state potential with d orbitals as there are some convergence issues with empty orbitals so an excited state is used.

[7] This claim was tested comparing the DFT results of calculations using PAW potentials created with several different electronic configurations for the valence electrons.

comparable convergence trends. Using this converged Brillouin zone grid and plane wave cutoff energy, a coupled DFT-MD calculation was conducted to obtain the ground state lattice spacing. A value of (4.05 ± 0.01) Å was found, equal to both the experimental value and other DFT-MD predictions, within error.

5.5 Ab initio calculation of the soft x-ray emission spectrum

The L-shell soft x-ray emission spectrum depends strongly on the band structure of the excited target that is emitting the radiation, in particular on its density of states. How the spectrum relates to the band structure in the low limit of irradiation intensities was an active area of research some 30–40 years ago (see for example [115, 116, 118]) and yielded precious information that was successfully coupled to the emerging field of *ab initio* electronic structure calculations, such as DFT.

In the experiments at FLASH we aim to take this approach a step further to explore the possibility of using this technique to characterize, in a time resolved manner, the creation and evolution of strongly coupled plasmas and warm dense matter. The differences between the emission from samples excited by XUV FEL radiation and more standard low-intensity sources such as synchrotrons are significant. First of all, the FEL pulse is extremely short, on the order of the core-hole recombination time, or shorter. This enables us to take snap shots of the system without having to average across various states as the system evolves in time. Also of relevance is the possibility to generate matter at finite temperatures and solid density in a straightforward manner by exploiting the various possible focusing schemes to create high-intensity radiation. The emission spectrum will give us in principle three pieces of very important information: the averaged temperature of the system, the electronic density and an indication of any electron-driven changes to the band structure. These three will be strongly interweaved and in order to maximize the amount of information that we extract, must be decoupled. The electronic density, which is a function of the width of the valence band, and the temperature, given by the slope on the high-energy edge of the spectrum (assuming Fermi-Dirac statistics) are fairly straightforward to extract once the DOS of the system is known. Obtaining the DOS is however far from trivial. For a free-electron-like simple metal, such as Al, at solid density and room temperature the problem simplifies, since the typical $\sqrt{E}$ free-electron behaviour may be assumed. The s and p components of the DOS may then be approximated roughly by $E^{1/2}$ and $E^{3/2}$. Multiplying this DOS by the Fermi-Dirac distribution

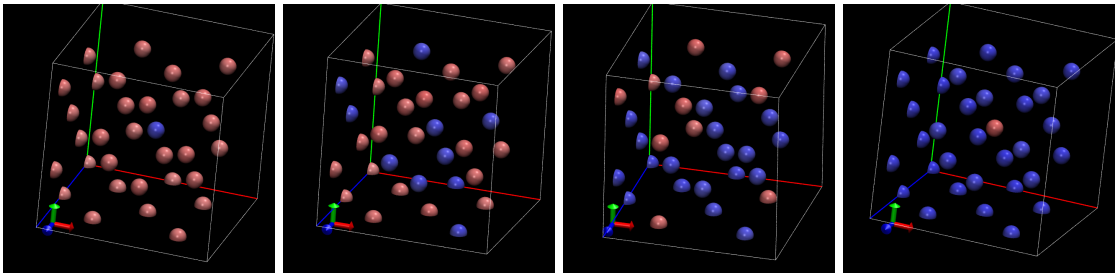

(a) 1 core hole (b) 10 core holes (c) 20 core holes (d) 31 core holes

Figure 5.8: 32-atom supercells used in the DFT-MD calculation containing 1, 10, 20 and 31 atoms with a core hole. Each box corresponds to a different intensity regime.

for the correct electron density and temperature gives the simplest approximation of the emission spectrum that is qualitatively correct. Adjusting the temperature and density in the distribution to best fit the experimental spectra then provides the required information. In the case of a metal that does not have a free-electron DOS, or of any system at higher temperature and/or containing a significant fraction of excited atoms, the band structure at the time of emission is in general not known. We will concern ourselves with its calculation from first principles, for an arbitrarily excited sample of Al at a temperature up to several eV, and compare our results to experimental spectra obtained at FLASH over a large range of intensities.

5.5.1 Electronic structure of a photo-excited Al plasma

The calculations for the ground state electronic structure was performed using the DFT-MD code *Abinit* at finite-temperatures, with the pseudopotentials discussed earlier. The target sample is simulated by a face-centred cubic (FCC) supercell containing 4, 32 or 128 atoms, all corresponding to a density of 2.7 g cm^{-3}. The box size is seen to give convergent results for cell sizes of 32 atoms or higher. The positions of the ions are found by equilibrating a molecular dynamics calculation at 300 K, which is the effective temperature of the ion subsystem throughout the emission process. Experimentally this is consistent with the fact that the emission arises from the first $\sim$40 fs in the evolution of the system, which is far too fast for the ions to respond in any way to the potentially modified electronic field.

In the following we will indicate atoms by their core state charge, as this is convenient when describing core hole excitation processes. It is understood that the system is

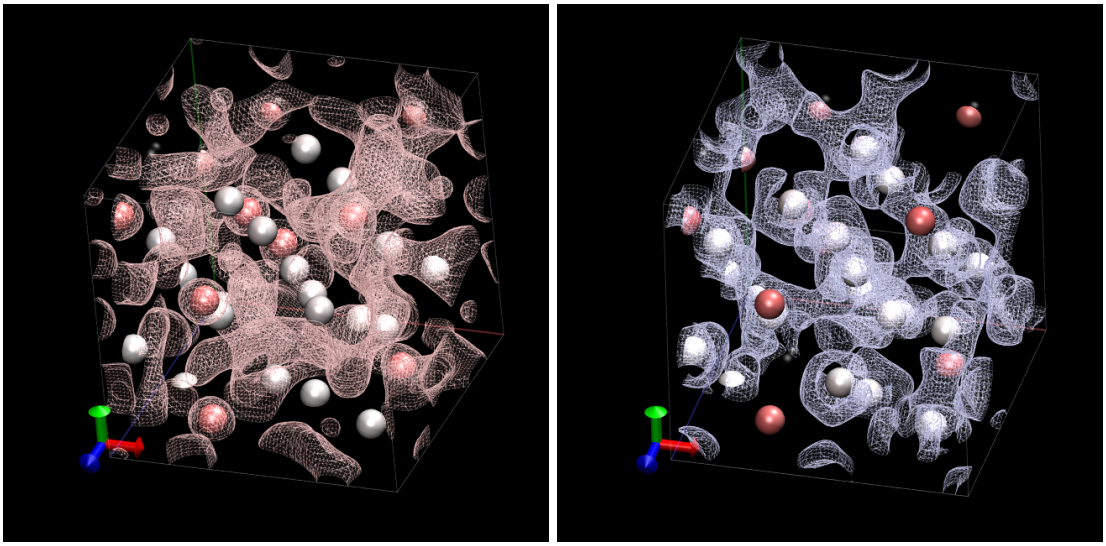

(a) Ground state valence density (b) Excited valence density

Figure 5.9: Density isosurfaces corresponding to the valence electrons from the ground state Al atoms show delocalised characteristics (a), while those due to the excited, fourth electrons, are more localized.

globally neutral[8], so any electrons missing in the core are implicitly assumed to be somewhere in the valence band. In this notation, ground state Al atoms are dubbed Al^{3+} (10 electrons in the core and 3 in the valence) and atoms with a single core hole Al^{4+} (9 electrons in the core and 4 in the valence).

As we wish to describe the high-intensity irradiation regime, an additional effect must be considered. It is a well known result from quantum mechanics that only the final state of the emission process should be considered in Eq. (5.9). This is known as the final state rule [132]. As the emission is intrinsically local to the atom in which the recombination has occurred, this means that only the final quantum state of the atom contributes to the emission intensity, i.e., the atomic ground state with a filled core hole and three electrons in the valence band. At standard intensities such as those routinely available on synchrotrons it is quite unlikely that during the emission the atom is surrounded by neighbours in a photo-excited state rather than in the ground state. Since the range of locality of the emission process does not extend beyond nearest neighbours, it is common practice to assume that the requirement of a local ground state in the emitting atom

[8]This might not be strictly true at the surface of the sample over a thickness of order 1 nm. Since the attenuation length of 13.5 nm radiation in Al is about 30 nm, surface effects are expected to be negligible.

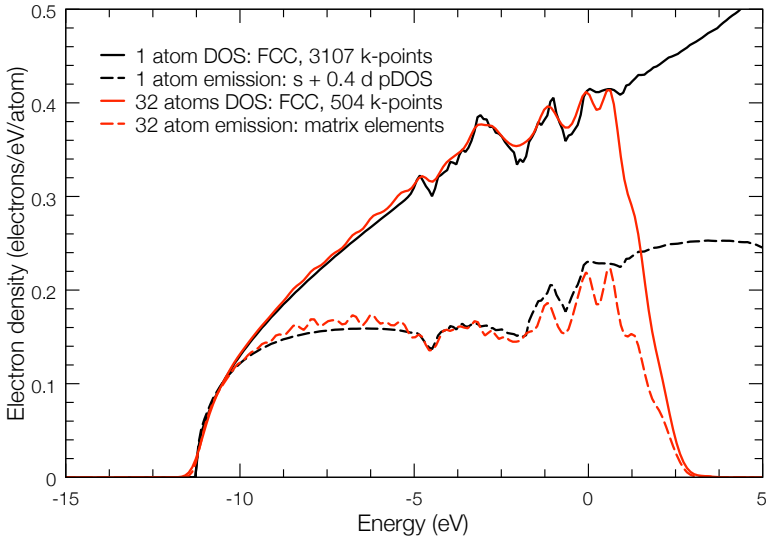

Figure 5.10: Comparison of the DOS computed with a 1-atom/cell and a 32-atom/cell, with a different number of k-points (solid line). The emission spectrum is obtained in the 32-atom case by calculating the full matrix elements of the transition (in the dipole approximation, as defined in Eq. (5.9)), while for the 1-atom case it is given directly by the $(s + \frac{2}{5}d)$ part of the pDOS.

(final state rule) is equivalent to requiring the entire system to be in the ground state. This considerably simplifies the calculation since a ground state DOS is sufficient to calculate the emission intensity through Eq. (5.9), with no reference to the excitation process nor to the excited states in the sample.

Above a certain intensity, $I_{\min}$, this will no longer necessarily be the case, as if the number of photons approaches the number of atoms in the interaction region, neighbouring atoms will necessarily be excited during the emission process. I will refer to these conditions as the high intensity regime and it is instructive to estimate the intensity at which such effects start becoming important. The average laser intensity above which an emitting atom will have a nearest neighbour in an excited state can be roughly estimated for a cubic system by

$$I_{\min} = \frac{gE_{\mathrm{ph}}}{a^3\tau} 3\eta(E_{\mathrm{ph}}), \tag{5.25}$$

where g is the ratio between the number of atoms in the unit cell and the number of nearest neighbours, E_{ph} is the excitation photon energy, a the lattice constant, τ the core hole recombination time and η the penetration depth within the sample. For bulk Al, $I_{\min}$ is of order 2×10^{13} Wcm^{-2}, which is readily accessible in our experimental

setup. Above this intensity the emitting atom has a non-negligible probability of having a Al^{4+} atom as its neighbour, and thus the relevant final state of the system, which is probed by the soft x-ray emission spectroscopy, is in fact given by the local DOS of an Al^{3+} ion surrounded by neighbours that can be either Al^{3+} or Al^{4+}, in a proportion that is a function of the XUV laser intensity. The goal is therefore to calculate the electronic structure of a system that is composed of a mixture of Al^{3+} and Al^{4+} atoms, and use it to predict the emission spectra pertaining to Al samples under high intensity irradiation.

Supercells of 32 atoms, containing between 0 and 31 core hole atoms are used in a finite-temperature DFT calculation, minimizing only the valence electrons. The number of electrons in the calculation then ranges from 96 to 127, which although large, is still practical and tractable on computer systems with a moderate number of CPUs (a converged DFT run and matrix element calculation with 96 electrons takes less than 2 hours on 128, 2.67 GHz Intel Xeon CPUs).

The sampling of the Brillouin zone is done with 504 k-points. Although the energy minimization of the DFT self-consistent cycle is converged with far less k-points, this higher resolution is necessary to accurately calculate the spectrum. The core wave functions $|\psi_{\text{core}}\rangle$ are calculated using an all-electron DFT calculation for atomic aluminium, used to generate the all-electron forzen core PAW pseudopotentials that represent the two different types of ion cores. The PAW-DFT calculation produces the eigenvalues $\varepsilon(n,k)$ and eigenfunctions $|\varphi(n,k)\rangle$ for the valence electrons for each k-point and energy band n. The wave functions are used to calculate the transition matrix elements and the eigenvalues are used to obtain the density of states. Summing over all k-points and occupied bands gives the radiated emission power of Eq. (5.9).

5.6 Assumptions

Several important assumption have been made for the analysis here presented, either implicitly or explicitly. These inevitably influence the final results and conclusions, and also to some degree the understanding of the absorption/emission process at high intensities. I have attempted to discuss all of these points in the preceding text and, before discussing the results, for the benefit of the reader, they are summarized below:

1. The excitation pulse consists of 92 eV photons that can excite at most one electron per atom of aluminium to the conduction band.

2. The excitation pulse is (significantly) shorter that the emission lifetime.

3. The conduction band electron-electron thermalization lifetime is significantly shorter than the emission lifetime. Fermi-Dirac temperature is meaningful.

4. Electron-hole interactions may be neglected.

5. Ion motion plays no role in the emission.

6. Many-body effects do not change significantly with intensity.

5.7 Results and discussion

As discussed in the beginning of this chapter, the emission spectrum is closely tied to the local pDOS. Given the p-like nature of the core hole, symmetry considerations suggest that only the $(s + \frac{2}{5}d)$ partial components of the DOS will contribute to the recombination process [133]. This contribution, compared to that of the entire valence band, can be estimated from Fig. 5.1. For a DFT calculation with only 1 atom in a primitive FCC cell, the pDOS can be efficiently calculated very accurately, using the tetrahedron method [134], and the emission spectrum is then automatically given. This is illustrated by the black curves in Fig. 5.10, where 3107 k-points were used for high resolution, which provide a rather stringent benchmark for the significantly more involved 32-atom calculation, for the simplest, ground state case. The 32-atom DOS is calculated directly by summation of the eigenvalues over all bands and k-points, following the definition given in Eq. (5.2), with the δ-function approximated by a Gaussian. The k-grid is reduced to 504 points, partially because the effective Brillouin zone is smaller, and partially because of computational constraints as the calculation grows in complexity and memory requirements. The emission spectrum in the 32-atom case is calculated through the full dipole matrix elements as given by Eq. (5.9). The agreement between the two calculations is very good. Note that the cutoff displayed by the 32-atom curves is due to the limited number of bands used in the calculation.

Such tests are clearly only possible for the ground state case. For the other more interesting cases, involving both ground state and excited atoms in the final state, only 32-atom calculations are conducted. The emission spectra resulting from four different mixtures of Al^{3+} and Al^{4+} atoms are shown in Fig. 5.11. The high-energy edges of all spectra are set to zero to facilitate the comparison of features. The lower curves represent the emission from an atom that was singly excited and the upper curves from one that was doubly excited. As such, in the experimental spectrum these would appear at two different energies, corresponding to the L-edge position given by the excitation:

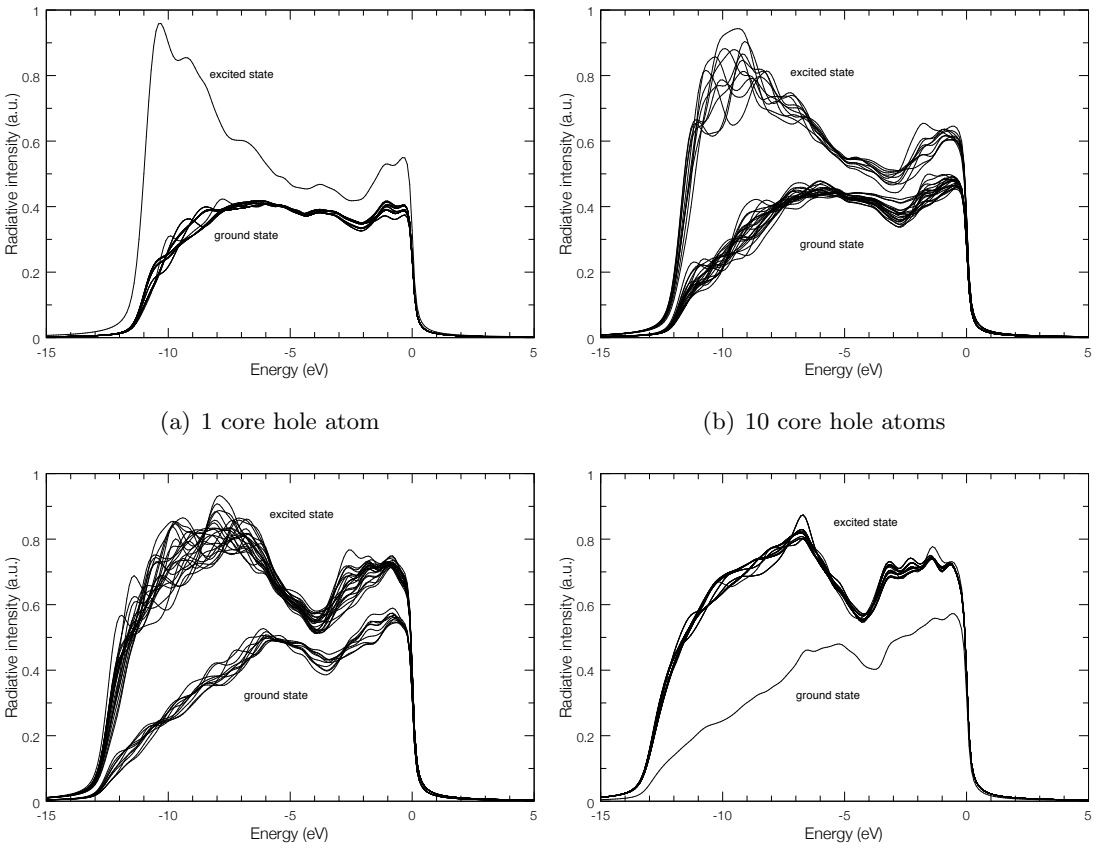

(a) 1 core hole atom

(b) 10 core hole atoms

(c) 20 core hole atoms

(d) 31 core hole atoms

Figure 5.11: Effect of micro-states on the emission spectrum for a 32-atom supercell calculation. Each curve represents the radiative intensity for a single atom either in the ground state or with one core hole in the final state (excited). The initial states corresponding to these spectra would be composed of singly and doubly excited atoms. The high energy edges, normally at 73 eV and 93 eV, have been set to zero for comparison.

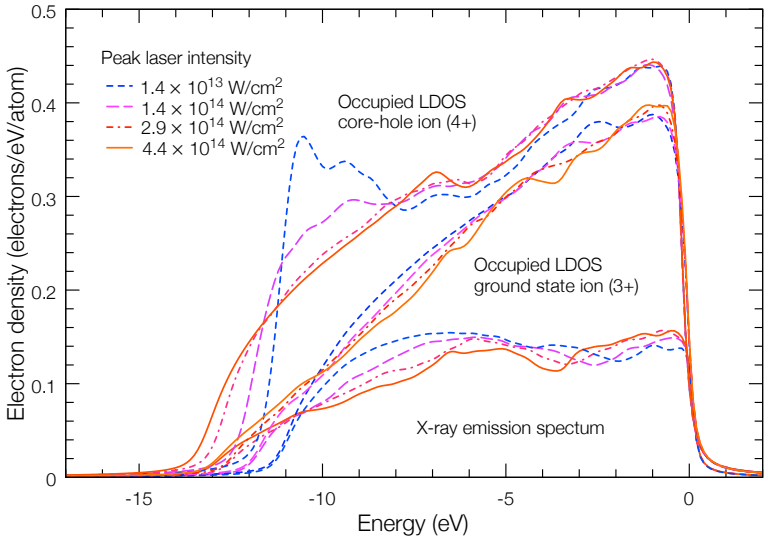

Figure 5.12: Average local electronic density in a system with a varying number of excited atoms. Also shown is the emission spectrum calculated according to Eq. (5.9), for an atom with a single core hole in the initial state. The number of excited atoms per 32-atom supercell are 1 (blue), 10 (purple), 20 (red) and 31 (orange), which are translated into photon intensity by the relation given in Eq. (5.25).

73 eV and 93 eV. Fig. 5.11 also shows the importance of micro-states, i.e., the effect that the geometrical arrangement within the cell of the excited atoms has on the final spectrum. Due to the rather strong confinement of the excess charge by the excited core and the localization of excited electrons, these effects are seen to be small. This justifies only considering average values over each type of atom as representative of the system in whole. These averages are shown for the emission spectrum in Fig. 5.12, together with the local electronic structure for both excited and ground state Al atoms. At low intensities, when a small number of excited atoms is present in the sample, the structure is very similar to that observed in $(Z, Z+1)$ binary alloys, such as Al/Si [135] and Mg/Al [136], where the impurity strongly modifies the bottom of the valence band locally. This indicates that the excited Al atom is seen by its neighbours as if it were a Si atom, since the excited core is efficiently screened and the electron contribution to the valence band per excited atom is four instead of three. As the intensity grows, so does the number of excited atoms and in the band structure around the Al^{4+} atoms starts returning to the typical free-electron-like shape, but with four electrons per atom in the valence band instead of three.

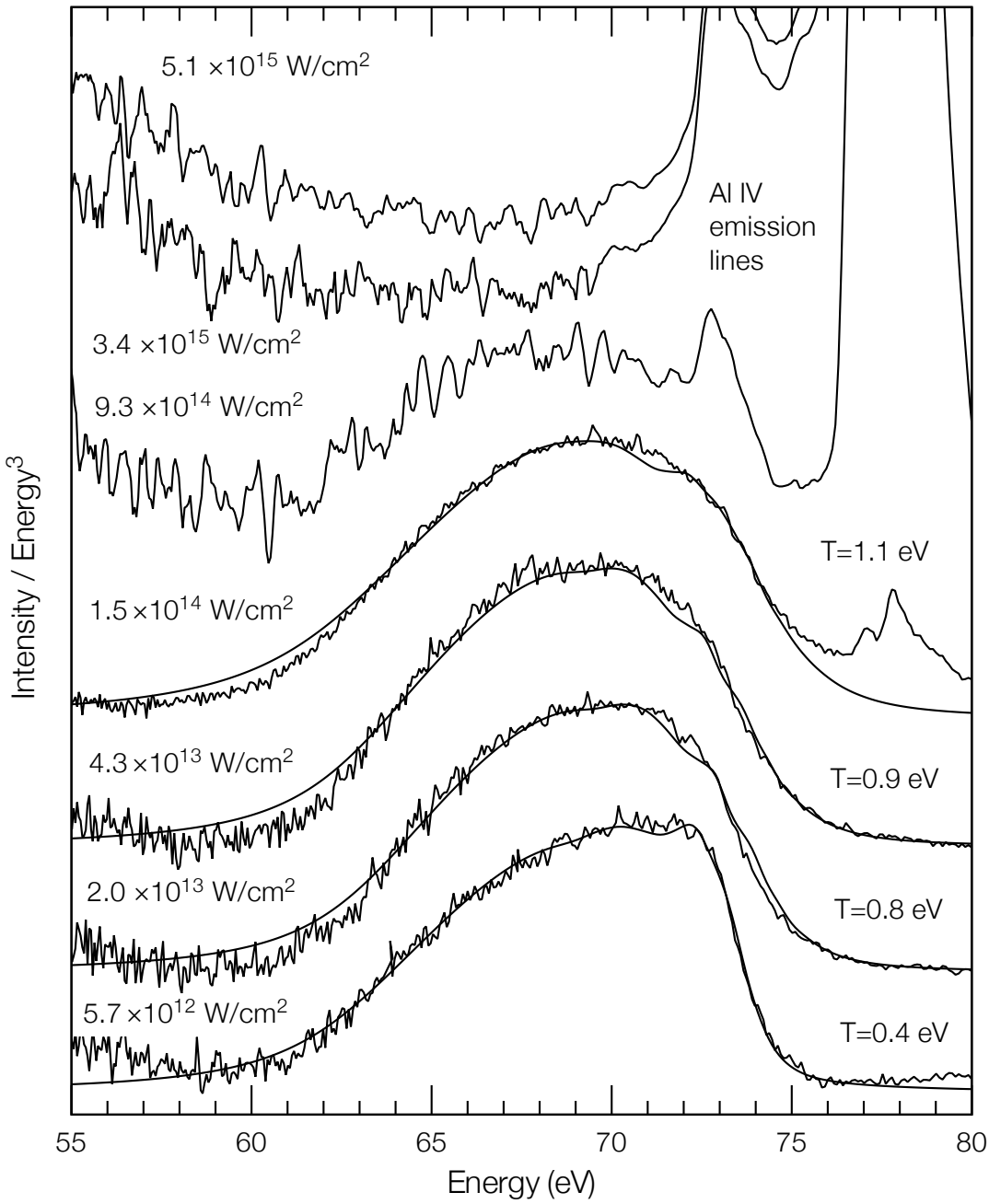

Figure 5.13: Soft x-ray emission spectra as a function of on-target intensity measured on FLASH. The emission corresponds to the radiative filling of a $2p$ core hole in Al. At higher intensities plasma line emission starts to dominate. The emission calculated through DFT-MD is given by the smooth superimposed line.

The experimental data acquired is summarized in Fig. 5.13. The bottom four curves were obtained on beam line BL2, while the top three are from beam line BL3 (see Fig. 5.5). The main feature of interest is the $L_{2,3}$ fluorescence peak with the high energy edge at 73 eV. Although the spectrometer is integrating over all time, some temporal information can be obtained from it since different features correspond to different emission times. The fluorescence peak is one of the first features to emerge, as it is governed by the core hole lifetime of around 40 fs. The energy width of the peak provides a direct measurement of the valence electron density. This bandwidth, together with the shape of the spectrum, gives indirect information on the ion density as well, since the valence band structure that is measured corresponds to a defined atomic arrangement. The high-energy slope provides a measurement of the temperature of the electrons. However, it is important to note that this temperature is averaged over all positions in the target and reflects the effects of portions irradiated at different intensities due to the FEL pulse profile. The electron temperature in the focus is most probably significantly higher. Also, the spectrum is collected over several shots and therefore over a range of intensities, due to the intrinsic energy fluctuation of the FEL beam.

In any case, significant average temperatures in the eV range are measured even at mid-range intensities. This indicates a large energy density is deposited in the sample during the femtosecond pulse heating, which will eventually be transferred from the electron system to the ions, causing the target to expand hydrodynamically. Recent investigations indicate that the time scale for this is on the order of several picoseconds [105]. As the density decreases below approximately 1 g/cm^3, the sample disassembles and plasma line radiation of this under-dense system dominates the emission spectrum. At intensities above $\sim 10^{14}$ Wcm^{-2}, these processes swamp the relatively weak soft x-ray emission, making the evaluation of the fluorescence features impossible. Interestingly, the highest ionization states that are observed correspond to Al IV (Al^{3+} ions).

The solid lines in Fig. 5.13 correspond to the DFT-MD calculated spectra. These are obtained through Eq. (5.9), considering a DOS level broadening given by Eq. (5.11) with the free parameter $\lambda = 0.53$ Å^{-1}, obtained by fitting the curve to the spectrum at lowest intensity. The electronic structure calculation is conducted taking as in input the core hole density and electronic temperature. The density is assumed to be an average value given by the mean experimental intensities (shown in Fig. 5.13). The results are very weakly dependent on this input, since, as can be promptly observed from Fig. 5.12, the density differences are small for intensities up to 1.5×10^{14} Wcm^{-2}, which is the highest for which reliable experimental data has been collected. Furthermore, the effect of Landsberg broadening contributes to reducing the density variations. The temperature

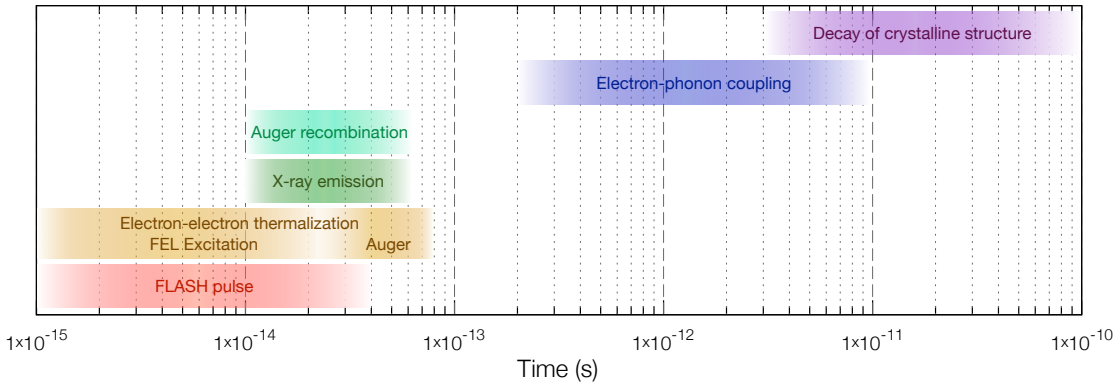

Figure 5.14: Timescales of occurrence of excitation, emission and equilibration processes in Al, relative to the 35 fs FLASH excitation pulse.

is obtained by fitting the experimental emission with a Fermi-Dirac distribution, and is the input into the FT-DFT-MD calculation. The temperatures obtained in this manner are given in Fig. 5.13. We note that this measurement confirms experimentally the prediction that the band structure of Al does not change significantly with temperatures, at least up to several eV [103].

It is tempting to compare the temperatures obtained by XES to those that follow from a basic absorption model, as derived in the previous chapter in Section 4.6. Following this model, the expected temperatures corresponding to the spectra shown in Fig. 5.13 are 0.8 eV, 1.2 eV, 1.8 eV and 3.2 eV, with an error of ± 0.1 eV. These values are, even before taking Auger recombination into account, about double those deduced from the measured spectra. This considerable difference may be due to several factors. First of all, in the model we have assumed that full thermalization occurs before the emission takes place. This turns out to be a rather poor assumption for the experimental conditions, given the similar lengths of the FEL pulse and the recombination time, as can be observed by referring to the relevant time scales depicted in Fig. 5.14. Another important point is that the pulse structure of the FEL beam is not known, and it is hard to estimate how much of the total energy of the beam is within the high intensity peak. That a meaningful amount of energy is located outside the main pulse would not be surprising given the SASE operation of FLASH. This effect and its consequences have been discussed in the previous chapter, based on the transmission measurements, and lead to an overestimation of the energy deposition, consistent with our observations here. A further effect to consider is transverse electron equilibration, where the heated region is larger than that excited, due to the finite primary and secondary electron mean free paths. Also, some

energy will inevitably be lost from the surface region as energetic electrons escape the sample. Although this effect is neglected in the bulk model, experimentally some surface effects will be present.

The electron thermalization process is overall very complex and an exhaustive theoretical study is beyond the scope of this thesis. The current results however do point out the need for such an investigation to help understand the way in which the deposited energy is equilibrated in the photo-excited system. Furthermore, a refinement of the experimental measurements could also significantly contribute to this understanding, in particular by measuring the electron temperature and density after all equilibration has occurred, but before much energy is lost to the ionic system. As indicated in Fig. 5.14, a probe delayed by 100–200 fs after the high-intensity excitation pulse could provide such information. Regrettably, such a pump-probe measurement using soft x-ray emission spectroscopy is currently beyond our experimental capability.

Several additional improvements can be made to these experimental results. The first is to work towards obtaining the spectra in single shot mode operation. While such a signal was seen to be too weak to be useable during the described campaign, at the time of writing we have already achieved this at LCLS and believe it possible at FLASH as well, due to the latest upgrade of the facility. Experimentally more challenging is the goal of obtaining spatially and temporally resolved emission spectra. Spatial resolution would allow to sample only the central part of the focused heating beam and study the highest temperatures. Picosecond temporal resolution on the other hand would permit the discrimination of solid-density effects from the very intense, but later-in-time occurring plasma line emission, and would allow us to observe the fluorescence at the highest intensities. Furthermore, measurements that would provide the ability to study the plasma emission evolution on these timescales would naturally be of great interest in their own right.

These first results are most promising as they indicate that by measuring the characteristics of the valence band through soft x-ray emission spectroscopy, electron temperature and density information can be extracted in a rather straightforward manner on the timescale of the probing beam. In our experiment, where the pump and the probe are the same pulse, this method yields the electronic structure right after the excitation and provides insight into the properties of the sample that will then evolve into warm dense matter. Future investigations using the XUV pulse solely as a probe following some alternative pump for the heating afford the potential to characterize the electronic structure as the sample transits from a solid to a warm dense plasma in a time resolved way.

CHAPTER 6

Conclusions and Outlook

I have presented some of the first results pertaining to the interaction of high intensity FEL light with solid density metallic samples. Much of the effort has been placed into establishing a detailed microscopic understanding of the absorption process and the related energy deposition. A substantial body of experimental work was conducted on the FLASH FEL in Hamburg, at a photon energy of 92 eV. In Al, this energy is sufficient to excite predominantly L-shell core electrons and the principal mechanism is bound-free absorption. As the intensity of the FLASH beam is raised above 10^{15}–10^{16} Wcm^{-2}, a strong bleaching of the transition occurs, yielding a saturation of absorption, which we have observed for the first time. This effect has far reaching consequences in the field of laser generated high energy density matter. The free-free absorption process has also been studied, below the Al L-edge at 73 eV, and our theoretical results indicate a behaviour in the WDM state which is significantly different from that predicted by standard plasma models based on inverse bremsstrahlung. We have not yet conducted experimental investigations in this regime, however we hope to do so in the near future. In addition to creating samples with high energy densities and observing the effect of high intensity radiation, we have also looked at how microscopic structural information could be extracted from such systems in a direct and possibly simple manner. To this end we have performed measurements of the soft x-ray emission spectra, emanated on short time scales from such samples, which have provided some initial, yet very promising results. Furthermore, I also hope to have conveyed the importance that XUV and x-ray

FELs, such as FLASH, LCLS[1] and others, bear to high energy density research as a tool to both create and probe such systems. I am certain they will prove invaluable in the years to come.

Outlook

The microfocusing setup described in the third chapter of this thesis has proved extremely successful and has paved the road to the series of high-intensity results that I have proceeded to illustrate in the subsequent chapters. This kind of setup continues to provide, at the time or writing, the highest intensities that can be reached at FLASH and will be used for at least another two experimental campaigns in 2011. The first aims at measuring directly the core-hole life time in a pump-probe scheme, exploiting the high intensity photo-induced transparency. The other is an experiment on x-ray diffraction imaging. On LCLS, different focusing schemes are being put in place due to the higher photon wavelength regime. These are based on Beryllium lens systems [137] or Kirkpatrick-Baez focusing pairs [138], which enable comparable intensities, and even intensities exceeding those reached by us in the XUV, to be obtained all the way into the hard x-ray regime. Importantly, such tight focusing schemes are incorporated into the facility beam lines so that the end user is no longer required to construct specific setups to reach the high intensity regime. The potential this has for future work on high energy density matter is considerable.

With the microfocusing setup on FLASH, we have demonstrated, for the first time, saturable absorption in the XUV region of the spectrum in solid density, metallic samples. The intensity of the FEL is sufficiently high to overdrive a core absorption channel into saturation, effectively bleaching it and rendering it transparent in that photon energy range for the duration of the core-hole lifetime, on the order of 20-40 fs. As this process intimately relates the pulse length to the recombination time, it can in principle be used to measure one of the two, provided the other is known. An experimental campaign aimed at using this femtosecond switching mechanism to measure the L-shell core-hole life time in Al is scheduled to take place in 2011. Furthermore, saturable absorption provides a new scheme that can be used to produce homogeneous samples of WDM efficiently. Indeed, above the saturation threshold, the energy deposition is far more volumetric and can improve the temperature homogeneity of the sample by up to an order of magnitude.

The condition of saturable absorption occurs for photon fluxes exceeding one photon

[1]These two are already operating as user facilities.

per each atom in the interaction region. In these conditions, the system is in a highly excited state of matter. Soft x-ray emission spectroscopy measurements in Al have shown that some vital information on this system can be obtained directly, in particular a mapping of the valence band through the core-hole recombination process. I have illustrated how the electron density and temperature can be extracted from this data, in addition to providing some information on the band structure, immediately after the excitation pulse. Several important improvements, such as collecting spectra from a sample after a single FEL pulse and resolving the spectra spatially afford the potential to significantly improve these results further and provide more detailed information.

First principles calculations based on FT-DFT-MD are proving to be a significant asset for the study of WDM systems. In this thesis, these calculations have been used to shed light on the opacity of matter undergoing a solid-plasma transition, as well as to predict the soft x-ray emission signal of a highly excited crystalline system.

The benefit to the study of soft x-ray spectroscopy is significant as DFT allows one to calculate the complete electronic structure, maximizing the information content. This provides substantially more information than can be simply retrieved from the measurements, and a reduction from the complete electronic band structure to the emission spectrum is needed. However, since a full data set is available computationally, we can infer certain additional details on the experimental system that would be otherwise hard to evaluate because of a strong convolution of competing effects. For example, some information has been deduced of the electron band structure (shape of the emission peak), the localization of excited and ground core electron states (overlapping region of the matrix element integrals), and ion-ion structure factor (that of an FCC lattice). Naturally, some of these effects are more important than others, and the weight each has in the final spectrum determines the detail and confidence level of the information that is retrieved. Based on this kind of reasoning we can conclude that for the measurements on FLASH, the electron band structure in Al does not change significantly with temperature up to over 1 eV, and is in fact comparable to that of cold Al. Further, the lattice is not modified during the first $\sim$100 fs. Of course, this last statement could be assumed trivial as the ions are inertially confined on these time scales, however it is important to note that this information is contained explicitly in the spectrum, i.e., even if the core-hole life time were significantly longer, the statement would still hold, provided the same spectra were measured. By nature of its electron gas and its behaviour at high temperatures, Al is a prototypical system, the band structure of which is only weakly dependent on the high intensity excitation. This is not generally the case, and some preliminary measurements on higher Z elements such as silver and gold indicate

that the importance of being able to model the photo-excited system accurately could be even more important. Based on the results presented, it would seem that soft x-ray emission spectroscopy could be an extremely useful source of information on the electronic structure of WDM and the solid-plasma transition in a pump-probe experimental investigation. Our observations indicate that the probe intensity should be kept under a threshold intensity of approximately 10^{14} Wcm^{-2}, whereas the pump should ideally exceed this value to provide significant heating. The main anticipated difficulty is the separation of signals between pump and probe, but it could be overcome, in principle, by employing an ultra-fast streak camera.

The theoretical work on the free-free absorption has proven illuminating in many ways. The rather extensive set of calculations have shown that an opacity model for WDM based on simple interpolations between the solid state absorption and that in a hot plasma neglects important effects. In particular this refers to the peak in absorption at temperatures around the Fermi temperature, which has been confirmed by FT-DFT-MD calculations and which provides a separation between models that show this effect and those which do not. Our semi-analytical calculations use the basis of inverse bremsstrahlung theory which includes electron degeneracy and temperature through the RPA dielectric function, and beyond, and employs the solid state-based pseudopotential theory to describe the interactions between electrons and ions. This potential corresponds to the effective crystalline potential and is weak, which justifies using the weak scattering (or second order Born) approximation. As shown shortly after the publication of our first results, similar, if not better results can be obtained using an atomic, or strong, potential, provided that the theory is expanded beyond the Born approximation [39]. The dependence of absorption calculations on pseudopotentials raises concern on the accuracy of such models: since the empirical solid state pseudopotentials are constructed *ad hoc* to yield reasonable results in solid systems, the extrapolation of these to WDM conditions, where they are untested, is problematic in the case the dependence of the model on the pseudopotential is strong. This illustrates one aspect of the theoretical difficulties in WDM and experimental results in this regime would be, once again, extremely valuable.

Additionally, several problems have emerged in the DFT opacity calculation. These calculations also employed pseudopotentials, however in contrast to the empirical empty core, these are parameter-free, all-electron, frozen core PAW potentials. Nevertheless, careful investigations have revealed several deficiencies in the potentials currently supplied with the VASP code which come into effect at photon energies significantly above the Fermi energy. Indeed, for the calculation of the absorption from first principles, the

band structure is needed for a very large range of energies since the initial and final states are linked by the absorbed photon, e.g., for the absorption of a 50 eV photon, the band structure (or the DOS) must be known for Al from 50-60 eV above the bottom of the band. As it happens, this proves to be beyond the accuracy of most potentials, which leads to inaccurate DFT results for the opacity. This is a very important observation as such calculations become more widespread. Fortunately, taking specific care in the development of high-quality potentials at high energies can substantially reduce, or indeed eliminate this problem altogether. The most recent work on this topic concerning the opacity of solid state, cold, crystalline Al is extremely promising, showing excellent agreement with experimental data over the full energy range [139]. These results are in preparation and are to be published shortly. Together with experimental measurements in this regime, first principles DFT calculations with the significantly improved potentials are the main goals for the near future in the study of the optical properties of WDM.

APPENDIX A

Some Blog Comments on Saturable Absorption

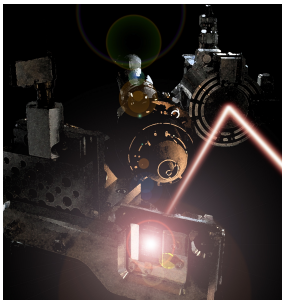

The following (unedited) comments were taken from the blogosphere shortly after Oxford University issued a press release on 27 July 2009, following our publication in Nature Physics of the observation of saturable absorption in the XUV (*Turning solid aluminium transparent by intense soft x-ray photoionization* [29]). Some are quite enjoyable!

- I'm going to make a t-shirt: "I took the energy used by an entire city and fired it through a laser at a tiny piece of aluminum 1/20th the size of a human hair and all I got was 10^{-15}th of a second of transparent aluminum"
- Pics or it didn't happen.
- This does not mean this process can be used to make transparent armor or other applications for super-strong glass. The article states that the x-rays were focused to a spot with a diameter smaller than a human hair's, the aluminum was transparent to ultraviolet, and the state lasted 40 femtoseconds. Details left out of the summary. Nonetheless, this is incredibly cool. The new state of matter that is being boasted about is one where a non-valent electron is removed from atoms. Very cool.
- 1. It's not invisible to the naked eye - only to "extreme ultraviolet radiation" 2. It's not anything like what was described in Star Trek 3. It's only "invisible" for milliseconds. Neat stuff for physicists, but not for anyone else, at the moment, as far as I can tell.

- Worlds most Powerful soft? X-Ray laser? Anyone see something wrong with those statements? The first is an oxymoron, and while Im no scientists, but dosent a laser imply focused light, not RADIATION?

  Answer to above: Visible light, X-rays, radio waves, etc are all forms of electromagnetic radiation. As for the soft X-Rays, from what Ive read it seems to be a new technique for using X-Rays to measure the electronic properties of materials.

- I've always wondered how experiments like this come about. Do they have an idea of what is going to happen or are they like, "We've got this new bad ass laser. Let's shoot it at something and see what it does."

- New state of matter? It's a solid, isn't it? See, in my high school chemistry class, when a particle had the wrong number of electrons, it was called an "isotope", not a "new state of matter".

- Point of note: another country moves forward in the field of scientific progress, while America watches "So you think you can dance?" and "Ghost hunters" on their "science channels."

- Salvaged from an alien spacecraft, just like shape memory alloy.

- They don't mention what happens after the 40 femtosecond period. The sample will produce both auger electrons and all classifications of x-ray radiation. Unless enduring stabilization of the electronic structure is possible, this so-called "new state of matter" would be incredibly lethal.

- Two reasons why article title is misleading: * Only last 40 femtoseconds (a unit of time so small I'm pretty sure they made it up just to describe this experiments brevity). * Only "nearly" (nearly!?) invisible under extreme ultraviolet radiation, so it's not exactly "invisible" to our range of sight, even if we could register the change in 40 fem-dom-seconds.

- Erm ... maybe the super powerful FLASH laser that is brighter than the light from a whole city actually *burnt a hole* through the really thin aluminium?!

- Did anyone consider the possibility that the X-ray may have knocked the sample into a parallel universe for 40 femtoseconds? Therefore, it would have appeared in this other dimension for 40 femtoseconds and surprised an innocent bystander in that universe. ;)

Bibliography

[1] https://lasers.llnl.gov/about/.

[2] N. B. Meezan et al. National ignition campaign hohlraum energetics. *Physics of Plasmas*, 17(5):056304, 2010.

[3] E. E. Salpeter. On convection and gravitational layering in Jupiter and in stars of low mass. *The Astrophysical Journal*, 181:L83–L86, 1973.

[4] J. J. Fortney and N. Nettelmann. The interior structure, composition, and evolution of giant planets. *Space Science Reviews*, pages DOI 10.1007/s11214–009–9582–x, 2009.

[5] J. J. Fortney, S. H. Glenzer, M. Koenig, B. Militzer, D. Saumon, and D. Valencia. Frontiers of the physics of dense plasmas and planetary interiors: Experiments, theory, and applications. *Physics of Plasmas*, 16:041003, 2009.

[6] R. W. Lee et al. Finite temperature dense matter studies on next-generation light sources. *Journal of the Optical Society of America B*, 20(4):770–778, 2003.

[7] http://www.esrf.eu/accelerators/performance/brilliance.

[8] H. Daido. Review of soft x-ray laser researches and developments. *Reports on Progress in Physics*, 65:1513–1576, 2002.

[9] DESY. Flash photo archive. http://www.desy.de/.

[10] J. M. J. Madey. Stimulated emission of bremsstrahlung in a periodic magnetic field. *Journal of Applied Physics*, 42:1906–1913, 1971.

[11] H. Motz. Applications of the radiation from fast electron beams. *Journal of Applied Physics*, 22:527–535, 1951.

[12] L. R. Elias, W. M. Fairbank, J. M. J. Madey, H. A. Schwettman, and T. I. Smith. Observation of stimulated emission of radiation by relativistic electrons in a spatially periodic transverse magnetic field. *Physical Review Letters*, 36(13):717–720, 1976.

[13] D. A. G. Deacon, L. R. Elias, J. M. J. Madey, G. J. Ramian, H. A. Schwettman, and T. I. Smith. First operation of a free-electron laser. *Physical Review Letters*, 38(16):892–894, 1977.

[14] M. J. Hogan et al. Measurements of gain larger than 10^5 at 12 μm in a self-amplified spontaneous-emission free-electron laser. *Physical Review Letters*, 81(22):4867–4870, 1998.

[15] S. V. Milton et al. Exponential gain and saturation of a self-amplified spontaneous emission free-electron laser. *Science*, 292(5524):2037–2041, 2001.

[16] J. Andruszkow et al. First observation of self-amplified spontaneous emission in a free-electron laser at 109 nm wavelength. *Physical Review Letters*, 85(18):3825–3829, 2000.

[17] V. Ayvazyan et al. Generation of GW radiation pulses from a VUV free-electron laser operating in the femtosecond regime. *Physical Review Letters*, 88(10):104802, 2002.

[18] V. Ayvazyan et al. A new powerful source for coherent VUV radiation: Demonstration of exponential growth and saturation at the TTF free-electron laser. *The European Physical Journal D - Atomic, Molecular, Optical and Plasma Physics*, 20:149–156, 2002.

[19] W. Ackermann et al. Operation of a free-electron laser from the extreme ultraviolet to the water window. *Nature Photonics*, 1(6):336, 2007.

[20] V. Ayvazyan et al. First operation of a free-electron laser generating GW power radiation at 32 nm wavelength. *The European Physical Journal D - Atomic, Molecular, Optical and Plasma Physics*, 37:297–303, 2006.

[21] P. Emma et al. First lasing and operation of an angstrom-wavelength free-electron laser. *Nature Photonics*, 4(9):641–647, 2010.

[22] U. Rössler. *Solid state theory*. Springer-Verlag, 2009.

[23] R. W. Godby, M. Schlüter, and L. J. Sham. Self-energy operators and exchange-correlation potentials in semiconductors. *Physical Review B*, 37(17):10159–10175, 1988.

[24] P. Hohenberg and W. Kohn. Inhomogeneous electron gas. *Physical Review*, 136(3B):B864–B871, 1964.

[25] J. Perdew, K. Burke, and M. Ernzerhof. Generalized gradient approximation made simple. *Physical Review Letters*, 77(18):3865, 1996.

[26] N. D. Mermin. Thermal properties of the inhomogeneous electron gas. *Physical Review*, 137(5A):A1441–A1443, 1965.

[27] S. M. Vinko, G. Gregori, M. P. Desjarlais, B. Nagler, T. J. Whitcher, R. W. Lee, P. Audebert, and J. S. Wark. Free-free opacity in warm dense aluminum. *High Energy Density Physics*, 5(3):124 – 131, 2009.

[28] A. J. Nelson et al. Soft x-ray free electron laser microfocus for exploring matter under extreme conditions. *Optics Express*, 17:18271, 2009.

[29] B. Nagler, U Zastrau, R. R. Fäustlin, S. M. Vinko, et al. Turning solid aluminium transparent by intense soft x-ray photoionization. *Nature Physics*, 5:693–696, 2009.

[30] S. M. Vinko et al. Electronic structure of an XUV photogenerated solid-density aluminum plasma. *Physical Review Letters*, 104(22):225001, 2010.

[31] http://hasylab.desy.de/science/user_collaborations/peak_brightness_collaboration.

[32] K. A. Brueckner and S. Jorna. Laser-driven fusion. *Review of Modern Physics*, 46(2):325–367, 1974.

[33] D. Kim and I. Kim. Calculation of ionization balance and electrical conductivity in nonideal aluminum plasma. *Physical Review E*, 68:056410, Dec 2003.

[34] B. L. Henke, E. M. Gullikson, and J. C. Davis. X-ray interactions: Photoabsorption, scattering, transmission, and reflection at E = 50-30,000 eV, z = 1-92. *Atomic Data and Nuclear Data Tables*, 54:181, 1993.

[35] E. M. Gullikson, P. Denham, S Mrowka, and J Underwood. Absolute photoabsorption measurements of Mg, Al, and Si in the soft-x-ray region below the $L_{2,3}$ edges. *Physical Review B*, 49(23):16283, 1994.

[36] R. Keenan, C. Lewis, J. Wark, and E Wolfrum. Measurements of the XUV transmission of aluminium with a soft x-ray laser. *Journal of Physics B: Atomic, Molecular and Optical Physics*, 35:L447, 2002.

[37] K. Sturm, E. Zaremba, and K. Nuroh. Core polarization and the dielectric response of simple metals. *Physical Review B (Condensed Matter)*, 42(11):6973, 1990.

[38] B. Crowley and J. Harris. Modelling of plasmas in an average-atom local density approximation: the CASSANDRA code. *Journal of Quantitative Spectroscopy and Radiative Transfer*, 71:257, 2001.

[39] C. A. Iglesias. XUV absorption by solid-density aluminum. *High Energy Density Physics*, 6(3):311 – 317, 2010.

[40] H. W. Koch and J. W. Motz. Bremsstrahlung cross-section formulas and related data. *Review of Modern Physics*, 31(4):920–955, 1959.

[41] J. Dawson and C. Oberman. High-frequency conductivity and the emission and absorption coefficients of a fully ionized plasma. *Physics of Fluids*, 5(3):517, 1962.

[42] A. Tronnier. *Absorption von VUV-Photonen in Warm Dense Matter*. PhD thesis, Max-Planck-Institut für Quantenoptik, 2007.

[43] V. Krainov. Inverse stimulated bremsstrahlung of slow electrons under Coulomb scattering. *Journal of Physics B*, 33:1585, Jan 2000.

[44] A. Ron and N. Tzoar. Interaction of electromagnetic waves with quantum and classical plasmas. *Physical Review*, 131(1):12, 1963.

[45] J. Hopfield. Effect of electron-electron interactions on photoemission in simple metals. *Physical Review*, 139(2A):A419, 1965.

[46] K. Sturm. Electron energy loss in simple metals and semiconductors. *Advances in Physics*, 31(1):1, 1982.

[47] N. R. Arista and W. Brandt. Dielectric response of quantum plasmas in thermal equilibrium. *Physical Review A - General Physics*, 29(3):1471, 1984.

[48] C. Pines. *Elementary Excitations in Solids*. Perseus Books Publishing, 1999.

[49] G. Mahan. Excitons in degenerate semiconductors. *Physical Review*, 153(3):882, 1967.

[50] G. Mahan. Excitons in metals. *Physical Review Letters*, 18(12):448, 1967.

[51] L. Kleinman. New approximation for screened exchange and the dielectric constant of metals. *Physical Review*, 160(3):585, 1967.

[52] M. Higuchi and H. Yasuhara. Kleinman's dielectric function and interband optical absorption strength of simple metals. *Journal of the Physical Society of Japan*, 69(7):2099, 2000.

[53] J.-P. Hansen and I. R. McDonald. *Theory of Simple Liquids*. Elsevier, 2006.

[54] S. Ichimaru. *Statistical Plasma Physics*. Westview Press, 2004.

[55] H. Singh and A. Holz. Structure factor of liquid alkali metals. *Physical Review A*, 28(2):1108, 1983.

[56] G. Gregori, A. Ravasio, A. Höll, S. Glenzer, and S. Rose. Derivation of the static structure factor in strongly coupled non-equilibrium plasmas for x-ray ... *High Energy Density Physics*, 3:99, 2007.

[57] R. Palmer and J. Weeks. Exact solution of the mean spherical model for charged hard spheres in a uniform neutralizing .... *The Journal of Chemical Physics*, 58(10):4171, 2003.

[58] E. Waisman and J. Lebowitz. Mean spherical model integral equation for charged hard spheres i. method of solution. *The Journal of Chemical Physics*, 56(2):3086, 1972.

[59] Galam S. and J.-P. Hansen. Statistical mechanics of dense ionized matter. VI. Electron screening corrections to the thermodynamic properties of the one-component plasma. *Physical Review A*, 14(2):816–832, 1976.

[60] F. J. Rogers, B. G. Wilson, and C. A. Iglesias. Parametric potential method for generating atomic data. *Physical Review A*, 38(10):5007–5020, 1988.

[61] Horsfield A. and N. Ashcroft. The Fermi surface and pseudopotentials of aluminium. *Journal of Physics*, 5:3925, 1993.

[62] M. W. C. Dharma-wardana and F. Perrot. Resistivity and dynamic conductivity of laser-pulse heated aluminum up to 10^6 K and along the shock .... *Physics Letters A*, 163:223–227, 1992.

[63] G. L. Krasko and Z. A. Gurskii. Concerning one model pseudopotential. *ZhETF Pis. Red.*, 9(10):596–601, 1969.

[64] N. D. Mermin. Lindhard dielectric function in the relaxation-time approximation. *Physical Review B*, 1(5):2362, 1970.

[65] N. W. Ashcroft. The Fermi surface of aluminium. *Philosophical Magazine*, 8(96):2055–2083, 1963.

[66] Y. Takada and H. Yasuhara. Dynamical structure factor of the homogeneous electron liquid: its accurate shape and the interpretation of experiments on aluminum. *Physical Review Letters*, 89(21):216402, 2002.

[67] http://henke.lbl.gov/optical_constants/.

[68] E. Wolfrum et al. Measurements of the XUV mass absorption coefficient of an overdense liquid metal. *Journal of Physics B*, 34(17):L565, 2001.

[69] T. W. Johnston and J. M. Dawson. Correct values for high-frequency power absorption by inverse bremsstrahlung in plasmas. *Physics of Fluids*, 16:722, 1973.

[70] Y. T. Lee and R. M. More. An electron conductivity model for dense plasmas. *Physics of Fluids*, 27(5):1273–1286, 1984.

[71] Y. Ping, D. Hanson, I. Koslow, T. Ogitsu, D. Prendergast, E. Schwegler, G. Collins, and A. Ng. Broadband dielectric function of nonequilibrium warm dense gold. *Physical Review Letters*, 96(25):255003, 2006.

[72] T. Ao, Y. Ping, K. Widmann, D. F. Price, E. Lee, H. Tam, P. T. Springer, and A. Ng. Optical properties in nonequilibrium phase transitions. *Physical Review Letters*, 96(5):055001, 2006.

[73] http://www.fluka.org/fluka.php.

[74] http://www.gsi.de/fair/overview/accelerator/index.html.

[75] N. A. Tahir et al. High energy density matter research using intense heavy ion beams at the future FAIR facility at Darmstadt: The HEDgeHOB collaboration. *Journal of Physics: Conference Series*, 112:042025, 2008.

[76] R. Mitzner, A. A. Sorokin, B. Siemer, S. Roling, M. Rutkowski, H. Zacharias, M. Neeb, T. Noll, F. Siewert, W. Eberhardt, M. Richter, P. Juranic, K. Tiedtke, and J. Feldhaus. Direct autocorrelation of soft-x-ray free-electron-laser pulses by time-resolved two-photon double ionization of He. *Physical Review A*, 80(2):025402, 2009.

[77] U. Fruhling et al. Single-shot terahertz-field-driven x-ray streak camera. *Nature Photonics*, 3(9):523–528, 2009.

[78] S. Bajt et al. Sub-micron focusing of soft x-ray free electron laser beam. In *Society of Photo-Optical Instrumentation Engineers (SPIE) Conference Series*, volume 7361, 2009.

[79] M. Born and E. Wolf. *Principles of Optics: Electromagnetic Theory of Propagation, Interference, and Diffraction of Light.* New York: Pergamon Press, 6th edition, 1989.

[80] E. W. Weisstein. Zernike polynomials. From Mathworld, A Wolfram Web Resource., 2010.

[81] J. C. Wyant and K. Creath. Basic wavefront aberation theory for optical metrology. *Applied Optics and Optical Engineering*, Volume XI, 1992.

[82] J. Chalupský et al. Characteristics of focused soft x-ray free-electron laser beam determined by ablation of organic molecular solids. *Optics Express*, 15(10):6036–6043, 2007.

[83] A. Agesi et al. Diode pumped neodymium lasers repetitively Q-switched by Cr^{4+}:YAG solid-state saturable absorbers. *IEEE Journal of Selected Topics in quantum Electronics*, 3:45–52, 1997.

[84] Y.F. Chen. Passively Q-switched diode-pumped Nd:YVO_4/Cr^{4+}:YAG single frequency microchip laser. *Electronics Letters*, 33:1880–1881, 1997.

[85] P. P. Sorokin, J. J. Luzzi, J. R. Lankard, and G. D. Pettit. Ruby laser Q-switching elements using phthalocyanine molecules in solution. *IBM Journal of Research and Development*, 8(2):182–184, 1964.

[86] J. Gu et al. Passive Q-switching of a Nd:YAG laser with a GaAs output coupler. *Opical Engeneering*, 38(11), 1999.

[87] J. Gu et al. Investigation on the use of semiconductor as Q-switch as well as output coupler for diode-pumped solid-state lasers. In *Conference on Lasers and Electro-Optics, 2000. (CLEO 2000)*, pages 461 –462, 2000.

[88] J.G. Rubiano, R. Florido, C. Bowen, R.W. Lee, and Yu. Ralchenko. Review of the 4th NLTE Code Comparison Workshop. *High Energy Density Physics*, 3(1-2):225 – 232, 2007.

[89] R. Neutze et al. Potential for biomolecular imaging with femtosecond x-ray pulses. *Nature*, 406(6797):752–757, 2000.

[90] S. Marchesini, H. Chapman, S. Hau-Riege, R. London, A. Szoke, H. He, M. Howells, H. Padmore, R. Rosen, J. Spence, and U. Weierstall. Coherent x-ray diffractive imaging: applications and limitations. *Optics Express*, 11(19):2344–2353, 2003.

[91] H. N. Chapman et al. Femtosecond diffractive imaging with a soft-x-ray free-electron laser. *Nature Physics*, 2(12):839–843, 12 2006.

[92] K. J. Gaffney and H. N. Chapman. Imaging Atomic Structure and Dynamics with Ultrafast X-ray Scattering. *Science*, 316(5830):1444–1448, 2007.

[93] H. Thomas et al. Shell explosion and core expansion of xenon clusters irradiated with intense femtosecond soft x-ray pulses. *Journal of Physics B: Atomic, Molecular and Optical Physics*, 42(13):134018, 2009.

[94] Y. H. Jiang et al. Investigating two-photon double ionization of D_2 by XUV-pump–XUV-probe experiments. *Physical Review A*, 81(5):051402, 2010.

[95] L. Young et al. Femtosecond electronic response of atoms to ultra-intense x-rays. *Nature*, 466(7302):56–61, 2010.

[96] http://aphysics2.lanl.gov/tempweb/.

[97] G. Dufour et al. K-LL auger spectrum of aluminium. *Physica Scripta*, 13:370–372, 1976.

[98] J. C. Fuggle, L. M. Watson, D. J. Fabian, and S. Affrossman. X ray excited auger and photoelectron spectra of magnesium, some alloys of magnesium and its oxide. *Journal of Physics F: Metal Physics*, 5:375–383, 1975.

[99] K. Wefers. Properties and characterization of surface oxides on aluminum alloys. *Aluminium*, 57(11):722–726, 1981.

[100] O. Svelto. *Principles of Lasers*. Plenum Press, 1998.

[101] W. Bambynek, B. Crasemann, et al. X-ray fluorescence yields, Auger, and Coster-Kronig transition probabilities. *Review of Modern Physics*, 44(4):716–813, 1972.

[102] J. C. Ashley, C. J. Tung, and R. H. Ritchie. Electron inelastic mean free paths and energy losses in solids. *Surface Science*, 81:409–426, 1979.

[103] V. Recoules et al. Effect of intense laser irradiation on the lattice stability of semiconductors and metals. *Physical Review Letters*, 96:055503, 2006.

[104] C. O. Ambladh et al. Theory of auger CVV processes in simple metals. *Physical Review B*, 39(6):3489, 1989.

[105] B. J. Siwick et al. An atomic-level view of melting using femtosecond electron diffraction. *Science*, 302(5649):1382–1385, 2003.

[106] O. L. Landen, S. H. Glenzer, M. J. Edwards, R. W. Lee, G. W. Collins, R. C. Cauble, W. W. Hsing, and B. A. Hammel. Dense matter characterization by x-ray thomson scattering. *Journal of Quantitative Spectroscopy and Radiative Transfer*, 71(2-6):465 – 478, 2001.

[107] G. Gregori, S. H. Glenzer, R. W. Lee, and O. L. Landen. Theoretical model of x-ray scattering as a dense matter probe. *Physical Review E*, 67:026412, 2003.

[108] D. O. Gericke, J. Vorberger, K. Wünsch, and G. Gregori. Screening of ionic cores in partially ionized plasmas within linear response. *Physical Review E*, 81(6):065401, 2010.

[109] E. Garcia Saiz et al. Probing warm dense lithium by inelastic x-ray scattering. *Nature Physics*, 4(12):940–944, 2008.

[110] B. Barbrel et al. Measurement of short-range correlations in shock-compressed plastic by short-pulse x-ray scattering. *Physical Review Letters*, 102(16):165004, 2009.

[111] R. R. Fäustlin et al. Observation of ultrafast nonequilibrium collective dynamics in warm dense hydrogen. *Physical Review Letters*, 104(12):125002, Mar 2010.

[112] P. A. M. Dirac. *Principles of Quantum Mechanics*. Oxford University Press, 3rd edition, 1947.

[113] P. T. Landsberg. A contribution to the theory of soft x-ray emission bands of sodium. *Proceedings of the Physical Society London*, A62:806, 1949.

[114] J. Pirenne and P. Longe. Contribution to the double electron transitions to the soft x-ray emission bands of metals. *Physica*, 30:277–292, 1964.

[115] H. Neddermeyer. Rontgenspektroskopische untersuchung der struktur des valenzbandes von aluminium. *Zeitschrift fur Physik*, 271:329, 1974.

[116] L. Smrčka. Calculation of soft x-ray emission spectra of aluminium by APW method. *Czech Journal of Physics B*, 21:683–692, 1971.

[117] C. F. Hague. 3p electron density of states in liquid aluminum. *Physical Review B*, 25(6):3529–3537, 1982.

[118] J. C. Fuggle, E. Källne, L. M. Watson, and D. J. Fabian. Electronic structure of aluminum and aluminum-noble-metal alloys studies by soft x-ray and x-ray photoelectron spectroscopies. *Physical Review B*, 16(2):750–761, 1977.

[119] A. S. Shulakov, A. Szász, H. Müller, and H. Kirchmayer. On the L_{23} soft x-ray emission of Al in Al-Mg alloys. *Physica Status Solidi*, 133:555–564, 1992.

[120] D. Liu, Y. Jin, and J. Deng. Ab initio calculations of the relationship between the alpha alumina toughness and its electronic structure under pressure. *Computational Materials Science*, 45:310–314, 2009.

[121] R. R. Fäustlin, U. Zastrau, S. Toleikis, I. Uschmann, E. Förster, and Th. Tschentscher. A compact soft x-ray spectrograph combining high efficiency and resolution. *Journal of Instrumentation*, 5:P02004, 2010.

[122] http://www.abinit.org.

[123] X. Gonze and othes. ABINIT: First-principles approach of materials and nanosystem properties. *Computer Physics Communications*, 180:2582–2615, 2009.

[124] X. Gonze et al. A brief introduction to the abinit software package. *Zeitschrift für Kristallographie*, 220:558–562, 2005.

[125] F. Bottin et al. Large scale ab initio calculations based on three levels of parallelization. *Computational Materials Science*, 42:329, 2008.

[126] M. Torrent et al. Implementation of the projector augmented-wave method in the abinit code. application to the study of iron under pressure. *Material Science*, 42:337, 2008.

[127] P. E. Blöchl, C. J. Först, and J. Schimpl. Projector augmented-wave method: ab initio molecular dynamics with full wavefunctions. *Bulletin of Material Science*, 26(1):33–41, 2003.

[128] P. E. Blöchl. Projector augmented-wave method. *Physical Review B*, 50(24):17953, 1994.

[129] C. Rostgaard. The projector augmented-wave method. *arXiv - Condensed Matter*, arXiv:0910.1921v2, 2009.

[130] http://www.wfu.edu/∼natalie/papers/pwpaw/man.html.

[131] http://www.abinit.org/downloads/paw.

[132] U. von Barth and G. Grossmann. Dynamical effects in x-ray spectra and the final-state rule. *Physical Review B*, 25(8):5150–5179, 1982.

[133] G. A. Rooke. Interpretation of aluminium x-ray band spectra. *Journal of Physics C: Proceedings of the Physical Society*, 2(1):767–775, 1968.

[134] P. E. Blöchl, O. Jepsen, and O. K. Andersen. Improved tetrahedron method for brillouin-zone integrations. *Physical Review B*, 49(23):16223–16233, 1994.

[135] N. Chetty et al. Vacancies and impurities in aluminum and magnesium. *Physical Review B*, 52(9):6313–6326, 1995.

[136] C. H. Zhang, K. L. Tsang, T. A. Callcott, D. L. Ederer, and E. T. Arakawa. Al $L_{2,3}$ and Mg double-ionization emission spectra of dilute Al in Mg alloys. *Physical Review B*, 37(5):2401–2407, 1988.

[137] A. Khounsary et al. Fabrication and evaluation of variable focus x-ray lenses. *Nuclear Instruments and Methods in Physics Research Sec. A*, 582(1):117 – 119, 2007.

[138] C. Morawe and M. Osterhoff. Hard x-ray focusing with curved reflective multilayers. *X-Ray Optics and Instrumentation*, 2010:479631, 2010.

[139] M. P. Desjarlais. Private communication.

List of Figures

List of Tables